

Local-field effects in nanostructured photonic materials

Ksenia Dolgaleva¹ and Robert W. Boyd^{2,3}

¹Department of Electrical and Computer Engineering, University of Toronto, 10 King's College Rd, Toronto, ON M5S 3G4, Canada (ksenia.dolgaleva@utoronto.ca)

²Department of Physics, University of Ottawa, Ottawa, ON K1N 6N5, Canada

³Institute of Optics, University of Rochester, Rochester, New York 14627, USA

Received October 14, 2011; revised January 16, 2012; accepted January 18, 2012; published March 13, 2012 (Doc. ID 156554)

It is well known that the optical response of a medium depends on the local field acting on an individual emitter rather than on the macroscopic average field in the medium. The local field depends very sensitively on the microscopic environment in an optical medium. It is thus possible to achieve a significant control over the local field by intermixing homogeneous materials on a nanoscale to produce composite optical materials. A combination of local-field effects and nanostructuring provides new degrees of freedom for manipulating the optical properties of photonic materials. Especially interesting opportunities open up in the nonlinear optical regime where the material response depends on the local-field correction as a power law. The goal of this review is to present a conceptual overview of the influence of local-field effects on the optical properties of photonic materials, both homogeneous and composite. We also give a summary of recent achievements in controlling the optical properties by local-field effects and nanostructuring. © 2012 Optical Society of America

OCIS codes: 160.3380, 160.2540, 190.4223, 190.4400, 260.2065

1. Introduction	3
2. Basic Concepts	4
2.1. Local Field	4
2.1a. Lorentz Local Field	4
2.1b. Onsager Model	6
2.1c. Real-Cavity Model	7
2.2. Nanocomposite Optical Materials	7
2.2a. Quasi-static Approximation and Finite-Wavelength Effect	8
2.2b. Composite Geometries	10
2.2c. Bounds on Effective Dielectric Constant	11

3. Local-Field Effects and Spontaneous Emission Rates in Dielectric Media	13
3.1. Macroscopic Theories	13
3.2. Microscopic Theories	16
3.3. Experimental Studies	18
3.4. Radiative Lifetime of Liquid Suspensions of Nd ³⁺ :YAG Nanoparticles	24
3.4a. Sample Preparation and Experiment	25
3.4b. Bi-exponential Fluorescence Lifetime	26
3.4c. Data Analysis	27
4. Influence of Local-Field Effects on Basic Laser Parameters	29
4.1. Idea of the Composite Laser	29
4.2. Laser Gain Properties of Composite Optical Materials	30
4.2a. Influence of Local Environment	31
4.2b. Influence of Composite Geometry	34
4.2c. Laser Gain Properties of Layered Composite Materials ..	35
4.2d. Laser Gain Properties of Maxwell Garnett Composite Materials	36
5. Nonlinear Optical Properties of Composite Materials	39
5.1. Local-Field Effects in Nonlinear Optics	39
5.2. Theoretical Predictions	41
5.2a. Maxwell Garnett Composite Geometry	41
5.2b. Layered Composite Geometry	45
5.2c. Bruggeman Composite Geometry	48
5.3. Experimental Studies	50
6. Cascaded Nonlinearity Induced by Local-Field Effects	54
6.1. Theoretical Prediction of Microscopic Cascading	55
6.2. Experimental Evidence of Microscopic Cascading	58
7. Conclusions	66
Acknowledgments	68
References and Notes	69

Local-field effects in nanostructured photonic materials

Ksenia Dolgaleva and Robert W. Boyd

1. Introduction

There is a huge variety of optical materials suitable for different applications, and there is always a need for a material that has optical properties superior to existing ones. Controlling the optical properties of photonic materials is thus a subject of great importance. There are many different approaches one can take to manipulate the optical properties of photonic materials. For instance, molecular engineering can be used to produce materials with a high nonlinear optical response. Photonic crystal structures enable dispersion control to achieve phase-matched nonlinear optical interactions and enhanced laser gain.

One approach that we discuss in this review is based on nanostructuring, *i.e.*, building nanocomposite optical materials by intermixing two or more homogeneous constituents on a nanoscale. Another approach relies on local-field effects, a phenomenon that has intrigued scientists for decades. Even before the practical importance of these effects was recognized, there had been a considerable interest in their fundamental nature. The realization that local-field effects could be utilized to manipulate the optical response has triggered an extensive study of their influence on the linear and nonlinear optical properties of photonic materials. The beauty of the two aforementioned approaches is that they can merge together to produce new degrees of freedom in controlling optical properties and to generate a new class of optical materials with highly tailorable optical responses.

The primary goal of this paper is to review how local-field effects can come into play in homogeneous and composite optical materials, in both the linear and the nonlinear optical regimes. We also discuss some recent achievements and outline future directions. As the scope of this review is fairly broad, we do not aim at providing details on narrowly focused subtopics, such as metal–dielectric composite materials and spectroscopy of nanopowders. We restrict ourselves to discussing the optical properties of dielectric composite materials, while briefly touching on the benefits of combining metals and dielectrics. We derive only more general equations that are crucial for understanding the topic at a fundamental level. To avoid overloading the paper, we provide references for more complex derivations and lengthy final expressions (*e.g.*, small-signal gain coefficients of composite materials). The overview presented herein is also aimed at clarifying some conceptual issues that

the authors have found to be the subjects of common misinterpretation or confusion.

The paper is organized as follows. In Section 2, we give an overview of various concepts that form the basis of the topic. In particular, we present the concept of the local field and describe the simplest models developed for the local-field correction factor. In addition, we review the idea of composite optical materials and their various geometries. In Section 3, we review the existing theories for treating the local-field-corrected spontaneous emission rate. We also discuss how these theories have been applied to describe the local-field effects in the experimentally measured radiative lifetime. In Section 4, we present the general idea of a composite laser and discuss the influence of local-field effects on the laser gain properties of nanocomposite optical materials. In Section 5, we discuss the role of local-field effects in the nonlinear optical response of composite materials. We review a recent theoretical and experimental study of the microscopic cascading phenomenon in nonlinear optics in Section 6. This phenomenon is purely a consequence of local-field effects. Finally, in Section 7, we present a summary, outline future directions, and mention a few interesting novel phenomena relying on local-field effects.

2. Basic Concepts

2.1. Local Field

It is well known that the field driving an atomic transition in a material medium, the local field, is different in general from both the external field and the average field inside the medium. The difference from the average field is not significant when one considers a low-density medium. To describe the optical properties of such a system, one can use the macroscopic (ensemble average) field. However, if the atomic density of a system exceeds approximately 10^{15} atoms/cm³ [1], the influence of local-field effects becomes significant and cannot be neglected.

In order to account for local-field effects on the optical properties of a material, one needs to utilize a proper model relating the local field to its macroscopic counterparts, namely, the average field and polarization. The choice of the model strongly depends on the medium of interest. For example, the local field in a homogeneous medium can be related to the macroscopic average field according to

$$\tilde{\mathbf{E}}_{\text{loc}} = L\tilde{\mathbf{E}}, \quad (1)$$

where L is the local-field correction factor. The tilde denotes quantities oscillating at an optical frequency. Existing theoretical models predict different expressions for the factor L . Below we give a brief overview of the models most commonly used by experimentalists to explain measurement results.

2.1a. Lorentz Local Field

It is conventional to describe local-field effects in a homogeneous material medium by using the well-known Lorentz model. In the

simplest version of this model, one treats the medium as a cubic lattice of point dipoles of the same sort. In order to find the local field acting on a typical dipole of the medium, one surrounds the dipole of interest with an imaginary spherical cavity of radius much larger than the distance between the dipoles, and much smaller than the optical wavelength. The contributions to the local field from the dipoles situated within the spherical cavity are accounted for exactly, while the dipoles outside the cavity are treated as uniformly distributed, characterized by some average macroscopic polarization. This approach yields the well-known expression

$$\tilde{\mathbf{E}}_{\text{loc}} = \tilde{\mathbf{E}} + \frac{4\pi}{3}\tilde{\mathbf{P}} \quad (2)$$

for the local field in terms of the average macroscopic field and macroscopic polarization $\tilde{\mathbf{P}}$. The local field given by Eq. (2) is called “the Lorentz local field.” It is derived in many textbooks (see, for example, [2,3]). The textbook model used for deriving Eq. (2) is known as the virtual-cavity model, because a fictitious sphere is introduced as a trick for calculating the local field acting on a typical dipole in the medium. An alternative, more elegant, derivation of relationship (2) that does not require introducing an imaginary sphere was proposed by Aspnes [4].

We further derive the Lorentz–Lorenz (or Clausius–Mossotti) relation for the dielectric permittivity ϵ and microscopic polarizability α . Let us assume for now that the medium is lossless and dispersionless. We represent the microscopic dipole moment induced in a typical molecule (or atom) of the medium as

$$\tilde{\mathbf{p}} = \alpha\tilde{\mathbf{E}}_{\text{loc}}. \quad (3)$$

The macroscopic polarization of the material is given by the equation

$$\tilde{\mathbf{P}} = N\tilde{\mathbf{p}}, \quad (4)$$

where N denotes molecular (or atomic) number density. Using Eqs. (2)–(4), we find that the polarization and macroscopic field are related by

$$\tilde{\mathbf{P}} = N\alpha\left(\tilde{\mathbf{E}} + \frac{4\pi}{3}\tilde{\mathbf{P}}\right). \quad (5)$$

We assume the polarization $\tilde{\mathbf{P}}$ to be linear in the average field:

$$\tilde{\mathbf{P}} = \chi^{(1)}\tilde{\mathbf{E}}, \quad (6)$$

where $\chi^{(1)}$ is the linear optical susceptibility of the medium. Substituting expression (5) into Eq. (6), solving for $\chi^{(1)}$, and eliminating the field $\tilde{\mathbf{E}}$, we find that

$$\chi^{(1)} = \frac{N\alpha}{1 - \frac{4\pi}{3}N\alpha}. \quad (7)$$

Expressing the left-hand side of Eq. (7) as $\chi^{(1)} = (\varepsilon - 1)/4\pi$, we obtain the well-known Lorentz–Lorenz (or Clausius–Mossotti) relation

$$\frac{\varepsilon - 1}{\varepsilon + 2} = \frac{4\pi}{3}N\alpha. \quad (8)$$

Through a rearrangement of Eq. (8), we can express the linear susceptibility as

$$\chi^{(1)} = \frac{\varepsilon + 2}{3}N\alpha. \quad (9)$$

Substituting expression (9) into Eq. (6), then Eq. (6) into Eq. (4), and using relationship (3) between the local field and the dipole moment, we obtain the equation relating the local field to the average field:

$$\tilde{\mathbf{E}}_{\text{loc}} = \frac{\varepsilon + 2}{3}\tilde{\mathbf{E}}. \quad (10)$$

The factor

$$L_{\text{Lor}} = \frac{\varepsilon + 2}{3} \quad (11)$$

is known in the literature as the Lorentz local-field correction factor. Expression (11) for the local-field correction factor is valid in the case of homogeneous media, where all the particles (molecules or atoms) are of the same sort. It is also valid in materials where the emitters enter as interstitial impurities that do not influence the correlation between the host molecules or atoms [5].

2.1b. Onsager Model

A different macroscopic model for describing the local field in homogeneous media was developed by Onsager [6]. In his study, Onsager treats a molecule or atom as being enclosed in a tiny real cavity in the medium. Then the field acting on the molecule is divided into the cavity field, which would exist at the center of the real cavity surrounding the molecule in the absence of the molecule, and the reaction field, which corrects the cavity field for the polarization of the surrounding medium by the dipole field of the molecule in the cavity. The resulting local field is given by

$$\tilde{\mathbf{E}}_{\text{loc}} = \frac{3\varepsilon}{2\varepsilon + 1}\tilde{\mathbf{E}} + \frac{2(\varepsilon - 1)}{(2\varepsilon + 1)a^3}\tilde{\mathbf{p}} \quad (12)$$

with the first and second terms expressing the cavity and reaction fields, respectively. Here a is the cavity radius. Even though the Lorentz and Onsager models yield different expressions for the local field, more rigorous theories, developed in [5,7], reconcile these two models, which appear to be two special cases.

In most of the experimental situations, one of the two macroscopic theories works reasonably well. The Onsager model is applicable to polar liquids, while the Lorentz model is applicable to solids. Both

models can describe a guest–host system. The Lorentz model describes such a system in cases when the guest’s molecule or atom replaces a molecule or atom of the host with similar polarizability [5]. An example is neodymium-doped yttrium aluminum garnet (Nd³⁺:YAG) where neodymium guest ions replace yttrium ions in the crystalline structure. Both neodymium and yttrium belong to the class of rare-earth metals and have similar properties. The Onsager model is more suitable when the polarizability of a guest is significantly different from that of the host molecules or atoms. Then the guest not only forms a cavity in the host medium, but affects the local field outside the cavity [6,8]. A good example of such a guest–host system is provided by liquid solutions of fullerene C₆₀ [8].

2.1c. Real-Cavity Model

If the polarizability of an emitter placed in a cavity inside a dielectric medium is small, so that the emitter does not impose strong changes on the local field outside the cavity, one can neglect the reaction field in Eq. (12). The local-field model resulting from this simplification is referred to as the “real-cavity” model. The expression for the local field given by the real-cavity model has the form

$$\tilde{\mathbf{E}}_{\text{loc}} = \frac{3\varepsilon}{2\varepsilon + 1} \tilde{\mathbf{E}}, \quad (13)$$

and the corresponding local-field correction factor is given by [9]

$$L_{\text{real}} = \frac{3\varepsilon}{2\varepsilon + 1}. \quad (14)$$

The real-cavity model describes the majority of experiments on measuring the radiative lifetime of composite optical materials, which we discuss in Section 3.

2.2. Nanocomposite Optical Materials

Nanocomposite optical materials are nanoscale mixtures of two or more homogeneous constituents in which the individual particles are much smaller than the optical wavelength, but still large enough to be characterized by their own dielectric constants. The optical properties of composite materials can be adjusted by controlling the constituents and morphology of the composite structure. Properly tailored composites can display the best qualities of each of their constituents, or, in certain cases, can display properties that even exceed those of their constituents. These features render composite materials valuable for applications in photonics and laser engineering.

Nanocomposite optical materials are becoming more and more important in laser applications, as nanofabrication technology has been rapidly developing. In particular, nanoscale ceramic composite laser gain media with improved optical properties have been reported [10,11]. It has also been shown that one can improve the performance of a laser material by mixing it with some other material on a nanoscale in such a way

that the thermal refractive index changes of the resulting composite material are smaller than those of either of the constituents [12,13]. In the current work we are concerned with controlling the laser properties of nanocomposite materials by using local-field effects [2,3].

The optical properties of composite materials have been the subject of many studies (see, for example, [14–17]). In particular, the modification of the radiative lifetime of composite materials caused by local-field effects was addressed in many publications both theoretically [5,9,18–20] and experimentally [21–29]. The influence of the local-field effects on the nonlinear optical properties of composite materials is even more significant, as the material response scales as several powers of the local-field correction factor. Theoretical modeling of the nonlinear optical response has been reported for many different geometries of composite materials [30–33]. In particular, rigorous theories for Maxwell Garnett-type composite materials [30] and layered composite materials [32] have been developed. It was shown that a significant enhancement of the nonlinear optical response is possible under certain conditions. A number of experiments in the field yielded promising results [34–37]. In such a way, a composite-material approach has proved to be a valuable tool in designing optical materials with improved laser properties and enhanced nonlinear response.

2.2a. Quasi-static Approximation and Finite-Wavelength Effect

There are several characteristic length scales associated with nanocomposite optical materials. The smallest dimension is the average size of the constituent grains. According to Aspnes [38], this quantity has the lower limit of 1–2 nm, at which individual particles can still be characterized by their dielectric permittivities. The upper limit on the sizes of the individual grains is dictated by the range of applicability of the effective-medium approximation that is valid as long as a composite optical material can be considered uniform at the scale of an optical wavelength. Within the effective-medium approximation, one can introduce an effective dielectric constant ϵ_{eff} in order to treat a composite optical material as quasi-homogeneous.

Different models for calculating ϵ_{eff} have been developed for different composite geometries (see Section 2.2b). These models rely on the infinite-wavelength approximation, neglecting the time variation of the optical field. Within the infinite-wavelength, or quasi-static, approximation, the particles of the constituents of the composite material behave as objects placed in a static electric field. They exhibit a screening surface charge, which results in differences of the local fields in different phases of the nanocomposite material. Under certain conditions, the electric field can become concentrated inside the grains with smaller dielectric constants (smaller optical density). It may seem counterintuitive at a first glance, as in waveguiding structures the electric field tends to accumulate in the regions with the higher dielectric constant. One should keep in mind, however, that the waveguiding structures operate in a different regime, the regime of guided waves, or finite wavelength. In that regime, the characteristic size of components of a heterogeneous structure is comparable with the wavelength of light, and total internal reflection of the wave at the boundary between more and less optically

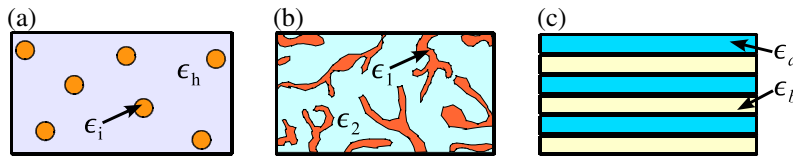
dense media can occur. The light tends to be confined within the regions with the higher dielectric constant, occupying the available spatial modes in these regions. The characteristic size of the constituent particles for which the waveguiding effect comes into play sets the upper limit beyond which the quasi-static approximation is no longer valid and the finite-wavelength effect has to be taken into account.

The range of validity of the quasi-static approximation has been tested both theoretically and experimentally by Aspnes and Egan in the 1980s [38–40]. The authors performed the measurement of the refractive index of a composite material formed by pressed spherical Al_2O_3 nanoparticles of different sizes at different wavelengths and compared the measurement outcome to the value of ε_{eff} predicted by the effective-medium approximation [40]. They found that the experimental measurements are in good agreement with the quasi-static approximation as long as the characteristic size of the constituent grains does not exceed 0.25λ . When the size of the grains reaches 0.5λ , the waveguiding effect becomes dominant. Comparing different theories with their measurement results, the authors also concluded that one cannot treat the effect of finite wavelength as time-dependent dipolar and quadrupolar corrections to the quasi-static approximation. Instead, one should incorporate the finite-wavelength effect in the initial formulation of the effective-medium problem.

Using the effective-medium approximation for describing nanocomposite optical materials involves spatial averaging. Another length scale associated with composite materials is the characteristic radius over which one performs the averaging. This quantity should be much larger than the average particle size, but much smaller than λ (see, for example, [30]). In more recent work [41], LeBihan *et al.* measured the distance at which an emitter in a composite optical material stops sensing the refractive index change due to the presence of an interface. As the emitter, the authors used a monolayer of $\text{Eu}^{3+}:\text{Gd}_2\text{O}_3$ material. The radiative lifetime of Eu^{3+} ions depends on the refractive index of the surrounding medium. The authors gradually modified the effective refractive index of the medium surrounding the ions by adding thin layers (18 ± 1 nm) of TiO_2 while measuring the changes in the radiative lifetime with every deposition. When the overall thickness of TiO_2 reached $\lambda/4$, the radiative lifetime of $\text{Eu}^{3+}:\text{Gd}_2\text{O}_3$ stopped changing with further depositions. The resulting overall thickness of TiO_2 represents the characteristic distance over which the averaging should be performed, as at this distance the composite optical material appears as uniform regarding the refractive index.

We finish this subsection by summarizing the characteristic length scales associated with a nanocomposite optical material. The individual grains of the composite constituents should be larger than 1–2 nm, but smaller than 0.25λ for the effective-medium theories to be valid. If the constituent particle size is larger than 0.25λ but smaller than 0.5λ , quasi-static approximation starts to break, and one should incorporate the finite-wavelength effect into the initial formulation of the effective-medium problem. When the constituent particle size becomes larger than 0.5λ , the waveguiding, or finite-wavelength, effect becomes dominant.

Figure 1



Composite material structures: (a) Maxwell Garnett geometry; (b) Bruggeman geometry; (c) layered geometry. Adapted with permission from Ref. [44] (<http://dx.doi.org/10.1088/1464-4258/11/2/024002>).

2.2b. Composite Geometries

There are mainly three types of composite geometries discussed in the literature: Maxwell Garnett composites [14,15,33], Bruggeman composites [37,42,43], and layered composites [32,33,36] (see Fig. 1).

The Maxwell Garnett type of composite geometry is a collection of small particles (the inclusions) distributed in a host medium. The inclusions are assumed to be spheres or ellipsoids of a size much smaller than the optical wavelength; the distance between them must be much larger than their characteristic size and much smaller than the optical wavelength. Under these conditions, one can treat the composite material as an effective medium, characterized by an effective (average) dielectric constant, ϵ_{eff} , which satisfies the relation [14,15]

$$\frac{\epsilon_{\text{eff}} - \epsilon_h}{\epsilon_{\text{eff}} + 2\epsilon_h} = f_i \frac{\epsilon_i - \epsilon_h}{\epsilon_i + 2\epsilon_h}. \quad (15)$$

Here ϵ_h and ϵ_i are the dielectric constants of the host and inclusion materials, respectively, and f_i is the volume fraction of the inclusion material in the composite.

In the Maxwell Garnett model the composite medium is treated asymmetrically. It is assumed that the host material completely surrounds the inclusion particles, and the result for the effective dielectric constant of the composite will be different if we interchange the host and inclusion dielectric constants in the expression (15). This problem is eliminated in the Bruggeman composite model [45], in which each particle of each constituent component is considered to be embedded in an effective medium characterized by ϵ_{eff} . The corresponding equation defining the effective dielectric constant thus has the form [37]

$$0 = f_1 \frac{\epsilon_1 - \epsilon_{\text{eff}}}{\epsilon_1 + 2\epsilon_{\text{eff}}} + f_2 \frac{\epsilon_2 - \epsilon_{\text{eff}}}{\epsilon_2 + 2\epsilon_{\text{eff}}}. \quad (16)$$

Here ϵ_1 and ϵ_2 are the dielectric constants of the constituent components 1 and 2, and f_1 and f_2 are the volume fractions of the components. If we accept that $f_1 = f_i, f_2 = f_h, \epsilon_1 = \epsilon_i$, and $\epsilon_2 = \epsilon_h$, Eq. (16) reduces to the Maxwell Garnett model (15) in the limit $f_1 \ll f_2$.

There are certain practical limitations associated with both Maxwell Garnett and Bruggeman composite geometries. The Maxwell Garnett model predicts the existence of plasmon resonances in the case when $\epsilon_i + 2\epsilon_h$ is close to zero, which is achievable in metal–dielectric material

systems, such as that originally described by Maxwell Garnett [14,15]. However, due to its asymmetrical treatment of the host and inclusion materials, this model is only applicable to the situations when the volume fraction of the inclusions is very small: $f_i \ll 1$. As the constituents are treated symmetrically in Bruggeman expression for ε_{eff} (16), this model can describe percolation. On the other hand, it does not predict surface plasmon resonances. Neither of the two models works well in the situations when the volume fractions of the two constituents are comparable. There has been some success in developing mean-field models that attempt to extrapolate between the two topologies (see, for instance, Ref. [46]).

The third composite model shown in Fig. 1 is a layered structure consisting of alternating layers of two materials (a and b) with different optical properties. The thicknesses of the layers should be much smaller than the optical wavelength. Materials of this sort are anisotropic. For light polarized parallel to the layers of such a composite material the effective dielectric constant is given by a simple volume average of the dielectric constants of the constituents:

$$\varepsilon_{\text{eff}} = f_a \varepsilon_a + f_b \varepsilon_b. \quad (17)$$

The electric field in this case is spatially uniform, as the boundary conditions require continuity of its tangential part on the border between two constituents. However, for the light polarized perpendicular to the layers, the effective dielectric constant is given by

$$\frac{1}{\varepsilon_{\text{eff}}} = \frac{f_a}{\varepsilon_a} + \frac{f_b}{\varepsilon_b}. \quad (18)$$

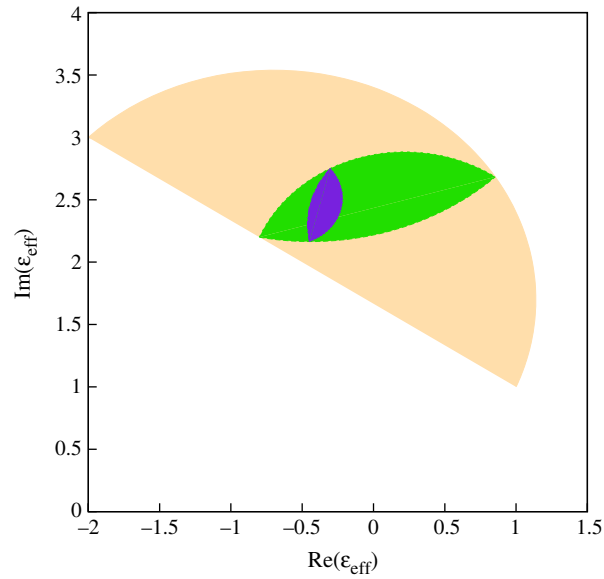
In the latter case the electric field is nonuniformly distributed between the two constituents in the composite, and local-field effects are of particular interest.

2.2c. Bounds on Effective Dielectric Constant

The theories developed for estimating the effective dielectric constant of composite geometries were elaborated under the assumption of perfect shapes of the individual particles. For example, Maxwell Garnett theory was developed for spherical nanoparticles surrounded by a dielectric host material. In practice, spherical nanoparticles tend to accumulate and form aggregates of random shapes, which makes it nontrivial, if not impossible, to precisely determine the value of the effective dielectric constant of the composite material. However, one can establish bounds on the value of ε_{eff} , based on the information available about the constituents of the composite optical material [39,47].

The most relaxed bounds for the value of ε_{eff} for any composite optical material are given by the Wiener limits [4,39,47], corresponding to the maximum and minimum screening of the electric field by the constituents, depending on the electric field polarization and the shape of the individual parts. If the particles form needles or elongated cylinders, and the electric field vector is polarized along the particles' largest dimension, the screening will be minimal, and the corresponding boundary value of the effective dielectric constants will be given by

Figure 2



Limits on the values of the effective dielectric constant of a two-component composite material. The constituents a and b have complex dielectric constants $\varepsilon_a = -2 + i3$ and $\varepsilon_b = 1 + i1$, respectively. The largest shaded area corresponds to the least restrictive Wiener bounds. The smaller shaded area corresponds to Hashin–Shtrikman limits for $f_a = 0.6$. The smallest shaded area represents Bergman–Milton limits for the case when the composite material is macroscopically isotropic. After Fig. 5 of Ref. [4]. Reproduced with permission. Copyright 1982, American Association of Physics Teachers (<http://dx.doi.org/10.1119/1.12734>).

Eq. (17). If the particles form discs, and the electric field is polarized perpendicular to their surfaces, the screening will be maximal, and ε_{eff} will be given by Eq. (18). Equations (17) and (18) thus represent two limiting cases of no screening and maximum screening for any composite geometry regardless of its morphology, and the actual values of ε_{eff} should fall within these limits. Such bounds are displayed in Fig. 2 as the largest shaded area, formed by a straight line (no screening) and a curve (maximum screening), for a two-component composite material in which the constituents have complex dielectric constants [4].

In cases in which the information about the volume fractions of the two constituents is available, the Wiener limits reduce to the more restrictive Hashin and Shtrikman bounds [39], displayed in Fig. 2 with a smaller shaded area for the case $f_a = 0.6$ [4]. If the composite optical material has an isotropic or cubic point symmetry, one can further confine the value of ε_{eff} to an even smaller region on the complex plane [47].

Aspnes and Egan [40] presented an elegant way to summarize all the models for calculating ε_{eff} and the limit theorems by using a single equation,

$$\varepsilon_{\text{eff}} = \frac{q\varepsilon_a\varepsilon_b + (1 - q)\varepsilon_h(f_a\varepsilon_a + f_b\varepsilon_b)}{(1 - q)\varepsilon_h + q(f_a\varepsilon_b + f_b\varepsilon_a)}. \quad (19)$$

Here ($0 \leq q \leq 1$) is a screening parameter, and ε_h is a host dielectric function that can be assigned the values of either ε_a or ε_b , or a combination of these, depending on the particular case. The Wiener limits for an arbitrary composition and microstructure are obtained from Eq. (19) by setting $q = 0$ or 1 and $0 \leq f_a \leq 1$. The Hashin–Shtrikman limits are defined by a known volume fraction f_a and $0 \leq q \leq 1$. The Bergman–Milton limits for 2D ($q = 1/2$) or 3D ($q = 1/3$) macroscopically isotropic composite materials can be obtained by fixing f_a and imposing the Wiener limits on ε_h , *i.e.*, $\varepsilon_h = x\varepsilon_a + (1 - x)\varepsilon_b$ and $1/\varepsilon_h = x/\varepsilon_a + (1 - x)/\varepsilon_b$, where $0 \leq x \leq 1$. It is remarkable that the Maxwell Garnett expression (15) for ε_{eff} also follows from Eq. (19) by setting $\varepsilon_h = \varepsilon_a$ or ε_b , and Eq. (16) for the Bruggeman effective-medium approximation can also be obtained from Eq. (19) by setting $\varepsilon_h = \varepsilon_{\text{eff}}$. Equation (19) thus summarized the effective-medium approximation for calculating the value of ε_{eff} for a two-component nanocomposite optical material of an arbitrary morphology and choice of constituents and their volume fractions.

Beyond the range of applicability of the quasi-static approximation, light tends to concentrate in regions of the composite material with the higher optical density. As a result, the effective value of the dielectric constant experienced by light under these condition can be higher than expected. In fact, it has been shown by Aspnes and Egan [39,40] that it can even lie outside Wiener limits.

3. Local-Field Effects and Spontaneous Emission Rates in Dielectric Media

Spontaneous emission occurs as a result of the interaction of an excited atom with the ground state of the quantized electromagnetic field. The rate of spontaneous emission can be described by Fermi's golden rule as

$$A = \frac{2\pi}{\hbar} |V_{12}(\omega_0)|^2 \rho(\omega_0). \quad (20)$$

Here $V_{12}(\omega_0)$ is the energy of interaction between the emitter and the electric field in the medium, and $\rho(\omega_0)$ is the density of states at the emission frequency ω_0 . It follows from Fermi's golden rule (20) that one can control the rate of spontaneous emission through the density of states. For instance, it has been demonstrated both theoretically and experimentally that the spontaneous emission rate can be suppressed or enhanced in the vicinity of a mirror or an interface [48,49], in periodic structures [50,51] or in a cavity [52,53]. Radiative processes in bulk dielectric media appear to be less well understood at a fundamental level, and in particular there has been much current interest in the effects of local fields on spontaneous emission. Numerous models have been developed to account for local-field effects on the spontaneous emission rate. These models tend to make different predictions. Below we provide an overview of some of them.

3.1. Macroscopic Theories

A very common approach used by many researchers to describe the influence of local-field effects on the spontaneous emission rate for

both homogeneous and composite dielectric media relies on the use of macroscopic theories. Most of these approaches are based on the quantization of the electromagnetic field in a dielectric medium and an assumption that the emitter embedded in the medium has no influence on the surrounding oscillators. Within this approach, one phenomenologically accounts for the local field by substituting it into the interaction energy, so that

$$V_{12, \text{loc}} \propto \frac{L}{n}, \quad (21)$$

while treating the density of states at the emission frequency as a macroscopic characteristic of the medium with the refractive index n [18]:

$$\rho(\omega_0) \propto n^3. \quad (22)$$

We also assume that the dielectric medium is lossless. The analysis can easily be extended to the case of absorbing dielectric media. The factor n in the denominator of relation (21) comes from the mode normalization and thus appears in the expression for the electromagnetic energy density in a dielectric medium [18]. Using Eqs. (20) through (22), one can establish the relationship between the local-field-corrected spontaneous emission rate A_{loc} in the dielectric medium and the spontaneous emission rate in the medium of unit refractive index (we call it A_{vac}) to be

$$A_{\text{loc}} = n|L|^2 A_{\text{vac}}. \quad (23)$$

Here and below in this paper we assign the “vac” subscript to the variables denoting quantities in a medium with the same chemical environment as that of the dielectric medium under consideration, but with the refractive index equal to unity. The variables marked with the “loc” subscript denote the local-field-corrected quantities. Relation (23) has been shown to hold also when the effect of dispersion is included in $V_{12, \text{loc}}$ and in the density of states [18]. The corresponding relation for the local-field-corrected radiative lifetime τ_{loc} in terms of the “vacuum” lifetime τ_{vac} takes the form

$$\tau_{\text{loc}} = \frac{\tau_{\text{vac}}}{n|L|^2}. \quad (24)$$

The form of the factor L , entering Eqs. (23) and (24), depends on the choice of the local field model. Two simple and intuitive models, the virtual-cavity (Lorentz) model [4] and the real-cavity model [9], are most commonly used for describing the experimentally measured radiative lifetime as a function of the refractive index. Within this section we will refer to the Lorentz model as the “virtual-cavity model” in order to emphasize its difference from the real-cavity model. Using the virtual-cavity approach, one arrives at expression (11) for the local-field correction factor [2,3]. Here we rewrite this expression as

$$L_{\text{virt}} = \frac{n^2 + 2}{3} \quad (25)$$

in terms of the refractive index of the dielectric medium. We also rewrite the expression for the local-field correction factor following from the

real-cavity model (14) as

$$L_{\text{real}} = \frac{3n^2}{2n^2 + 1}. \quad (26)$$

Expressions (25) and (26) for the local-field correction factor are very different and lead to different results for the radiative lifetimes in a dielectric medium. In fact, they describe different physical situations. An attempt to classify the physically different systems has been reported by de Vries and Lagendijk [5]. They present a microscopic theory based on resonant classical light scattering by impurity atoms inside dielectric cubic lattices, and they introduce a distinction between interstitial and substitutional types of impurities, depending on the way the emitters enter a lattice and their influence on the correlations between the rest of the particles in the medium. The interstitial case occurs when the emitters do not influence the many-particle correlation and interact with Lorentz local field in the lattice, and the virtual-cavity model is valid. The substitutional case occurs when the impurities have correlations comparable with those of the particles constituting the lattice. In this case, the real-cavity model is applicable. The authors of [5] thus identify the conditions under which each of the cavity models is applicable. Their generalized theory describes both types of impurity and can be reduced to the virtual- and real-cavity models in the limiting cases. Their theory based on resonant scattering thus agrees with the macroscopic theories.

Most of the experiments on evaluating the influence of the local-field effects on the radiative transition rate were performed in composite optical materials. A commonly accepted way of describing the measured local-field-corrected radiative lifetime is to compare the measurements to Eq. (24) with either a real- [Eq. (26)] or a virtual-cavity [Eq. (25)] local-field correction factor. In this case, an effective refractive index n_{eff} of the composite optical material, given by an appropriate model corresponding to the composite geometry (see Subsection 2.2), is used everywhere in place of the refractive index n in Eqs. (24)–(26). We also give another example of a phenomenological macroscopic model developed by Pukhov *et al.* [54] to describe the local-field effects on the radiative lifetime in composite optical materials. The authors point out that mere replacement of the refractive index n of a bulk material with the refractive index n_{eff} of a composite material in Eqs. (23)–(26) does not account for the difference between the local field acting on an emitter within a constituent nanograin where it is embedded and the average mesoscopic field in the nanograin. They modify Eq. (23) to phenomenologically account for the difference, so that

$$A_{\text{loc}} = n_{\text{eff}} L_{\text{nano}} L_{\text{bulk}} A_{\text{vac}}. \quad (27)$$

Here the local-field correction L_{nano} in Eq. (27) accounts for the difference between the macroscopic average field in the entire composite material and the mesoscopic average field in the constituent containing the emitters, while L_{bulk} is a function of n_{bulk} of the bulk constituent material containing the emitters and accounts for the local-field effects in the bulk constituent. In order to avoid an ambiguity of choosing the model for L_{bulk} , the authors of [54] suggest that the experimentally measured spontaneous emission rate in the nanocomposite materials should be

compared with that of the bulk materials,

$$A_{\text{loc}} = \frac{n_{\text{eff}}}{n_{\text{bulk}}} L_{\text{nano}} A_{\text{bulk}}. \quad (28)$$

The problem is now reduced to finding the right form of L_{nano} .

In their later studies [55,56], the authors consider composite materials comprising spherical and ellipsoidal inclusions embedded in a dielectric host and derive the corresponding expressions for the spontaneous emission rate explicitly. For the case of spherical inclusions, they obtain

$$A_{\text{spher}} = \frac{n_{\text{eff}}}{n_i} \left[\frac{3}{2 + \varepsilon_i/\varepsilon_h - f_i(\varepsilon_i/\varepsilon_h - 1)} \right] A_{\text{bulk}}, \quad (29)$$

where f_i is the volume fraction of the inclusions in the nanocomposite, and ε_i and ε_h are the dielectric constants of the inclusion and host, respectively. The effective dielectric constant $\varepsilon_{\text{eff}} = n_{\text{eff}}^2$ is given by the Maxwell Garnett expression (15). The expression for the spontaneous emission rate for an isolated ellipsoidal inclusion has the form

$$A_{\text{ellips}} = \frac{n_h}{n_i} \sum_{\alpha=a,b,c} \left[\frac{\gamma_\alpha}{1 + (\varepsilon_i/\varepsilon_h - 1)N_\alpha} \right]^2 A_{\text{bulk}}, \quad (30)$$

where $\gamma_\alpha = d_\alpha / \sqrt{\sum_\alpha |d_\alpha|^2}$ are the direction cosines of the transition dipole moment with respect to the principal axes a , b , and c of the ellipsoid, and N_α are the depolarization factors.

3.2. Microscopic Theories

The key feature of the macroscopic approaches is quantization of the electromagnetic field in a dielectric under the assumption that the oscillators forming the dielectric are not influenced by the emitter. The latter is assumed to interact with nonlocal vacuum field modes determined by the macroscopic density of states. Local-field effects exist due to the dipole–dipole interaction between the particles forming the dielectric and manifest themselves at the microscopic scale within the characteristic distances much smaller than the optical wavelength. It seems thus plausible, in a strict manner, to consider the interaction of the emitter with the local vacuum radiation field modes in order to accurately evaluate the influence of the local-field effects on the spontaneous emission rate [57,58].

Crenshaw and Bowden [57] presented a fully microscopic theory based on a many-body quantum electrodynamical approach. Within their model, the emitters are treated as two-level atoms (TLAs) embedded in an absorptive and dispersive dielectric host. The emitters and host particles are assumed to interact with each other only through the electromagnetic field. The model yields an expression for the spontaneous emission rate of the form

$$A_{\text{loc}} = L A_{\text{vac}}, \quad (31)$$

where L takes the form of the Lorentz factor (11) as a result of the interaction between the emitter and nearby polarizable particles of the host via the electromagnetic field.

The result given by Eq. (31) differs significantly from that of the macroscopic theories (23) in that there is no refractive index present in expression (31) and the factor L appears in it in the first power. This result not only challenges the macroscopic theories of spontaneous emission rate, but also such fundamental concepts as Fermi's golden rule and fluctuation–dissipation theorem. In [58], the authors extend their fully microscopic many-body quantum electrodynamical treatment to revisit these fundamental concepts, showing that there is no contradiction within their formalism. They argue that, when dealing with dipole–dipole interactions, one should distinguish the macroscopic electrodynamical environment of the dielectric from the local environment of the emitter. The reciprocal dipole–dipole interaction of the emitter with the dielectric in its near vicinity leads to the self-action, neglected in macroscopic theories, resulting in the difference of the local-field-corrected spontaneous emission rate (31) from Eq. (23). This self-action is the modification of the local field acting on a dipole through the contribution of the dipole itself to the local fields of the nearby dipoles.

In his later work [59], Crenshaw further analyzes the inconsistency of the macroscopic theory with the fully microscopic theory. He derives the optical Bloch equations by using two approaches: quantum-classical theory relying on the classical Lorentz model of the local field, and macroscopic quantum electrodynamics. The inconsistency found in the expressions for the Lorentz frequency shift and Rabi frequency (electric field) is attributed to the failure of the macroscopic theory to properly account for the local-field effects. The results obtained by using the quantum-classical theory based on the Lorentz local field model are consistent with those obtained earlier using the fully microscopic model [57].

The fact that the local-field correction factor appears in the first power in the expression for the local-field-corrected spontaneous emission rate is typical for fully microscopic approaches [60]. For instance, another microscopic model, developed by Kuznetsov *et al.* [61,62], leads to an expression for the spontaneous emission rate where factor L enters in the first power, similar to Eq. (31). In their model, Kuznetsov *et al.* [62] consider a three-component system consisting of two sets of TLAs and a quantized electromagnetic field. Like Crenshaw and Bowden [57], they assume that the emitters and host TLA systems interact only through the electromagnetic field. The group of the emitting TLAs is assumed to be in resonance with the external electromagnetic field, while the group of host TLAs are assumed to have their resonance frequency far from that of the external field. The authors use a different approach, adapting the Bogolyubov–Born–Green–Kirkwood–Yvon formalism [63] to the problem and deriving a system of coupled equations for the evolution of the emitters' density matrix. The resulting expression for the local-field-corrected spontaneous emission rate is

$$A_{\text{loc}} = nL A_{\text{vac}}. \quad (32)$$

The difference of Eq. (32) from Eq. (31) is that the dependence on the refractive index is now present, and the local-field correction factor is given by the real-cavity model (14).

The fully microscopic theory developed by Crenshaw and Bowden raised much discussion. One attempt to reconcile it with macroscopic theories is due to Berman and Milonni [64]. These authors developed an alternative microscopic theory of the spontaneous emission rate, considering a system consisting of an emitter embedded in a bath of other atoms comprising a dielectric. The modification to the spontaneous emission rate is then a consequence of the dipole–dipole interaction between the emitter and the bath atoms. The modification of the decay rate of the source atom was calculated exactly as an integral over all space. Berman and Milonni have shown that their result is fully consistent with that of the macroscopic theories.

Another example of a microscopic theory reproducing the result of the macroscopic theories belongs to Knoester and Mukamel [65]. They have derived an equation of motion describing the excited-state dynamics of impurity molecules embedded in an atomic crystal. The molecules were assumed to interact with each other through an exciton–polariton exchange. Full agreement with Eq. (23) was obtained, where the local-field correction factor (11) appeared from the microscopic theory as a consequence of the interactions between the molecules.

It is evident from Eqs. (23)–(32) that different macroscopic and microscopic approaches to treating the local-field-corrected spontaneous emission rate lead to quite different results. It is generally recognized that some of them—*e.g.*, the macroscopic theory [Eq. (23)] with virtual-cavity [Eq. (25)] and real-cavity [Eq. (26)] local field models—describe physically different systems. Nevertheless, in some experiments an agreement was found with a model that is generally applicable to a physically different material system (see, for instance, Ref. [66]). The question about the range of applicability of various theoretical models of the local-field-corrected spontaneous emission rate thus remains open. Below we review some recent attempts to explain the existing experimental results with different models.

3.3. Experimental Studies

The expressions for the local-field-corrected spontaneous emission rate contain the dependence on the refractive index and local-field correction factor. It is thus convenient to test the theories by measuring the radiative lifetime of emitters as a function of the refractive index of the background dielectric medium. The easiest way to produce a system where all the parameters but the refractive index remain unchanged is by making composite optical materials, dispersing nanograins containing emitters in background materials with different refractive indices. Some examples of composite materials for the radiative lifetime measurements include liquid suspensions of nanoparticles [29,66], quantum dots [28], dye molecules dissolved in water droplets [26,27], Eu^{3+} organic complexes in liquids [21] and supercritical gas [22], and rare-earth ions embedded in a binary glass system $x\text{PbO} - (1 - x)\text{B}_2\text{O}_3$ [23,24].

Here we summarize the models for the local-field-corrected spontaneous emission rate, discussed above, applying them to the radiative lifetime under the assumption of a lossless composite dielectric medium. As we mentioned in Subsection 3.1, it is common to replace the bulk refractive index n with the effective refractive index n_{eff} of a composite optical material in describing the influence of the local-field effects on its radiative lifetime. We thus rewrite the expressions for the radiative lifetime in terms of n_{eff} to emphasize that we are dealing with the composite optical materials in this section. Neglecting local-field effects, one obtains the expression

$$\tau_{\text{noLFE}} = \frac{\tau_{\text{vac}}}{n_{\text{eff}}} \quad (33)$$

for the radiative lifetime in the dielectric medium. We refer to this model as “no local-field effects,” and call the corresponding radiative lifetime τ_{noLFE} . The macroscopic virtual- and real-cavity models of the local field yield

$$\tau_{\text{virt}} = \frac{1}{n_{\text{eff}}} \left(\frac{3}{n_{\text{eff}}^2 + 2} \right)^2 \tau_{\text{vac}} \quad (34)$$

and

$$\tau_{\text{real}} = \frac{1}{n_{\text{eff}}} \left(\frac{2n_{\text{eff}}^2 + 1}{3n_{\text{eff}}^2} \right)^2 \tau_{\text{vac}}, \quad (35)$$

respectively. The fully microscopic model from [57] yields

$$\tau_{\text{micro}, 1} = \frac{3}{n_{\text{eff}}^2 + 2} \tau_{\text{vac}}, \quad (36)$$

and the microscopic model developed later in [62] results in

$$\tau_{\text{micro}, 2} = \frac{1}{n_{\text{eff}}} \frac{2n_{\text{eff}}^2 + 1}{3n_{\text{eff}}^2} \tau_{\text{vac}}. \quad (37)$$

Finally, we also give the expression for the radiative lifetime obtained in [54] for spherical inclusions:

$$\tau_{\text{spher}} = \frac{n_i}{n_{\text{eff}}} \left[\frac{2 + \varepsilon_i/\varepsilon_h - f_i(\varepsilon_i/\varepsilon_h - 1)}{3} \right] \tau_{\text{bulk}}. \quad (38)$$

Here τ_{spher} is expressed in terms of the radiative lifetime τ_{bulk} of the bulk material containing the emitters, instead of τ_{vac} .

Generally, the measured decay time τ_{meas} is not purely radiative and can be expressed in terms of the radiative and nonradiative decay times, τ_{rad} and τ_{nonrad} , as

$$\frac{1}{\tau_{\text{measured}}} = \frac{1}{\tau_{\text{rad}}} + \frac{1}{\tau_{\text{nonrad}}}. \quad (39)$$

It is commonly assumed that the nonradiative decay time $\tau_{\text{nonrad}} = A_{\text{nonrad}}^{-1}$ does not depend on the refractive index of the surrounding material [21,27] and can be roughly expressed in terms of the radiative lifetime of ions in vacuum by using the relation

$$\eta = \frac{A_{\text{rad}}^{(\text{vac})}}{A_{\text{rad}}^{(\text{vac})} + A_{\text{nonrad}}} \quad (40)$$

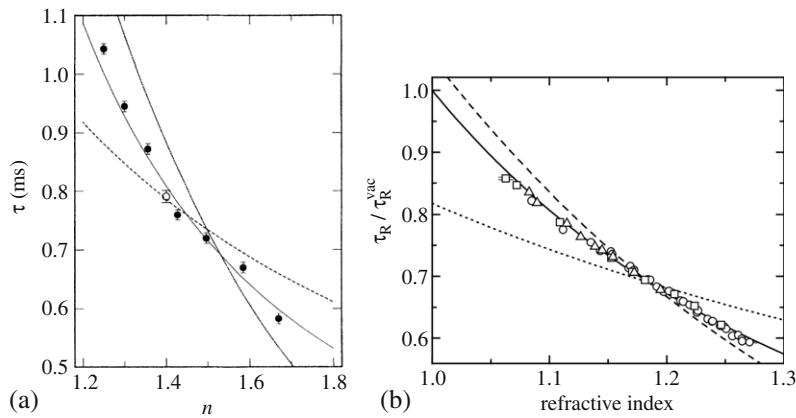
for the quantum yield η of the material. Quantum yield is the fraction of the energy decaying through the radiative channel, so the measured lifetime is purely radiative only in the case when the quantum yield of the material is close to unity. Unlike τ_{nonrad} , τ_{rad} is altered by the local-field effects.

In order to compare the experimentally measured radiative lifetime as a function of n_{eff} to the theory, one typically performs a least-squares fit of the data to the theoretical models, using the unknown “vacuum” lifetime τ_{vac} as a free fitting parameter. The nonradiative transitions can significantly contribute to the population decay dynamics. A common mistake that can lead to a misinterpretation of the experimental data is assuming that $\tau_{\text{measured}} \approx \tau_{\text{rad}}$ in the case when the quantum yield is different from unity, and applying the local-field models (34)–(38) directly to τ_{measured} . It is thus important to use Eq. (39) as a fitting function for the experimental data whenever $\eta < 1$.

The macroscopic virtual- and real-cavity models have been most commonly used by experimentalists, especially in the earliest reports when other models had not yet been developed [21,22,66]. In Fig. 3, we show the measurements of the radiative lifetime of Eu^{3+} organic complexes embedded in dielectric backgrounds with different refractive indices [21] [Fig. 3(a)], and suspended in supercritical gas [22] [Fig. 3(b)]. The refractive index variation in the latter case is achieved through changing the gas pressure. In both reports the measured lifetime was fitted to the no-local-field-effects [Eq. (33)], virtual-cavity [Eq. (34)], and real-cavity [Eq. (35)] models with the best agreement provided by the real-cavity model. The real-cavity model is justified in this type of composite material, as Eu organic complexes, containing low-polarizability Eu^{3+} ions, expel the surrounding solvents or gas from the volume occupied by them, thus producing real cavities in the surrounding dielectric medium [5,25]. It is therefore physically reasonable to use the empty-cavity model of the local field to explain the experimental results.

The measurements of the radiative lifetime of $\text{Y}_2\text{O}_3:\text{Eu}^{3+}$ nanoparticles suspended in different liquids, reported by Meltzer *et al.* [66], display the best least-squares fit with the virtual-cavity model [see Fig. 4(a)]. This result is quite surprising, as the virtual-cavity model is applicable only to homogeneous media or the media with interstitial type of inclusions (emitters) that do not change the correlation between the surrounding lattice particles [5]. The result has been revisited by Duan *et al.* [25] in their article, where they analyze in which situations the virtual- and real-cavity models are applicable. Duan *et al.* have successfully fitted the original data from [66] with the real-cavity model, modifying it so that the refractive index of the cavity is equal to the index of Y_2O_3 . This choice

Figure 3



(a) Experimentally measured radiative lifetime of Eu^{3+} ions embedded in organic ligand cages, suspended in apolar liquids (points). The lines show the best least-squares fit to the no-local-field model [Eq. (33), dashed curve], virtual-cavity model [Eq. (34), dotted curve], and real-cavity model [Eq. (35), solid curve]. Reproduced with permission from Fig. 2, Ref. [21]. Copyright 1995 by the American Physical Society (<http://link.aps.org/doi/10.1103/PhysRevLett.74.880>). (b) Experimentally measured radiative lifetime of Eu^{3+} organic complexes, suspended in supercritical gas (points). The lines show the best least-squares fit to the no-local-field model [Eq. (33), dotted curve], virtual-cavity model [Eq. (34), dashed curve], and real-cavity model [Eq. (35), solid curve]. Reproduced with permission from Fig. 3, Ref. [22]. Copyright 1998 by the American Physical Society (<http://link.aps.org/doi/10.1103/PhysRevLett.80.5077>).

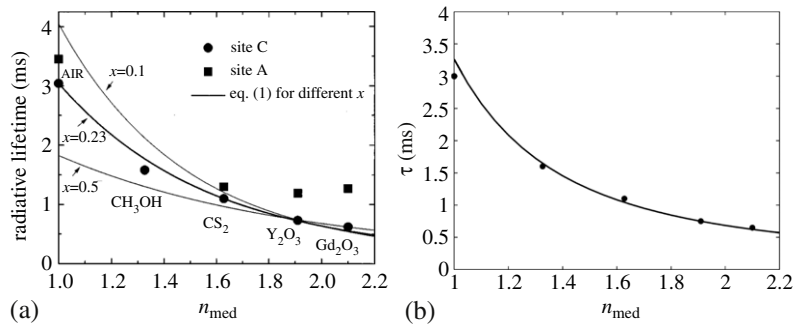
is justified, as the nanoparticles replace a part of the surrounding liquid, producing within it real cavities with the refractive index of Y_2O_3 . Duan *et al.* replaced the refractive index in Eq. (35) with the ratio $n_r = n_{\text{eff}}/n_{\text{Y}_2\text{O}_3}$, so that it becomes

$$\tau_{\text{real}} = \frac{1}{n_r} \left(\frac{2n_r^2 + 1}{3n_r^2} \right)^2, \quad (41)$$

and obtained excellent agreement with the modified real-cavity model [see Fig. 4(b)].

The radiative decay rate, measured in Eu^{3+} [23] and Tb^{3+} [67] ions embedded in $x\text{PbO} + (1-x)\text{B}_2\text{O}_3$ binary glass matrix, has also shown agreement with the real-cavity model (see Fig. 5). The refractive index change was achieved through changing the ratios of PbO and B_2O_3 components in the glass matrix. Kumar *et al.* explain their results by the fact that the virtual-cavity model is applicable only to homogeneous media where all the particles are of the same kind [23]. This interpretation, however, calls for a better physical explanation, which was later provided by Duan *et al.* [25]. Their explanation of the results reported in [23] relies on the fact that the bond length of Pb–O is comparable with that of a rare-earth ion and oxygen, while the bond length of B–O is significantly smaller. It is thus likely that the

Figure 4

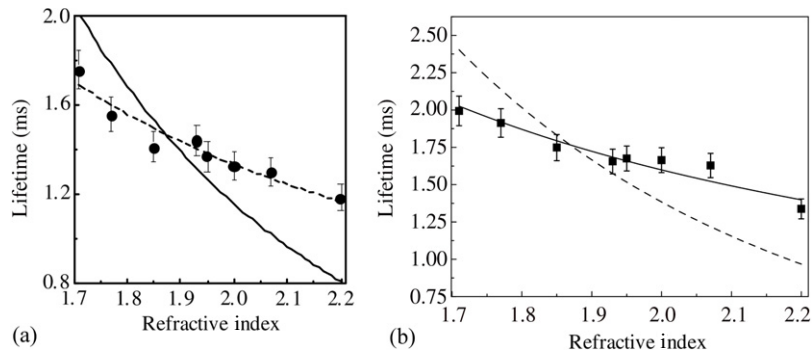


(a) Experimentally measured radiative lifetime of $\text{Eu}^{3+}:\text{Y}_2\text{O}_3$ nanoparticles suspended in different liquids and air (circles). The curves show the best least-squares fit with the virtual-cavity model [Eq. (34)] for different volume fractions x of the nanoparticles, as labeled. Reproduced with permission from Fig. 2, Ref. [66]. Copyright 1999 by the American Physical Society (<http://link.aps.org/doi/10.1103/PhysRevB.60.R14012>). (b) Reinterpretation of the results from [66] by fitting them with a modified real-cavity model with the best least-squares fit obtained for the volume fraction of the $\text{Eu}^{3+}:\text{Y}_2\text{O}_3$ nanoparticles $x = 0.15$. Reproduced with permissions from Fig. 3, Ref. [25]. Copyright 2005 by Elsevier (<http://dx.doi.org/10.1016/j.physleta.2005.06.037>).

rare-earth ions replace Pb atoms in the glass matrix. As the polarizability of the rare-earth ions is relatively low, while the polarizability of Pb is very high, such a replacement is physically similar to an empty cavity formation in the surrounding medium. This example thus corresponds to the substitutional case, as defined by De Vries and Legendijk [5].

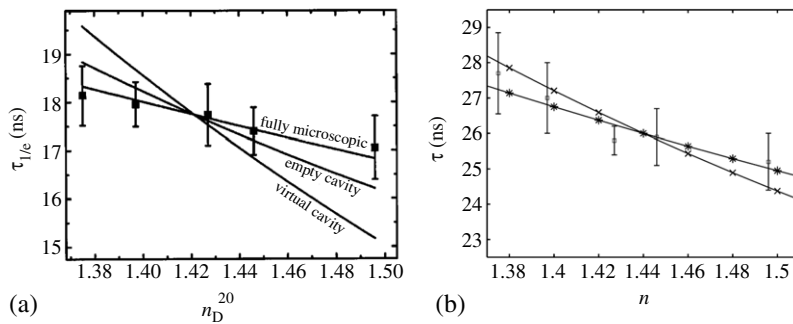
Measurement of the radiative lifetime in liquid suspensions of organically capped CdTe and CdSe quantum dots has been reported by Wuister *et al.* [28] [see Fig. 6(a)]. The data were fitted with the virtual-cavity, real-cavity, and fully microscopic [Eq. (36)] models, with the latter model giving the best least-squares fit. The authors of [36] explain this result with the fact that the polarizability of the quantum dots is very high, and the quantum dots exhibit self-action through the polarization changes that they introduce to their local environment. This situation is similar to the conditions of Crenshaw and Bowden's fully microscopic model [57], where the self-action of the emitter is taken into account. The authors of [36], however, did not account for the fact that their quantum dots have a quantum yield much lower than unity ($\eta \approx 0.55$). This issue has been raised by Duan *et al.* in Ref. [25], where they attempt to reinterpret the data by using the real-cavity model and Eq. (39). Indeed, for such a low value of quantum yield one needs to take into account nonradiative processes when describing the local-field effects on the radiative lifetime. It is also plausible to use the Onsager cavity model, where the reaction field is taken into account, to interpret the data reported in [28]. This is a justified approach, as a quantum dot has a very large polarizability, and, being enclosed in an organic cap, replaces a volume within a liquid in which it is suspended.

Figure 5



Experimentally measured radiative lifetime of (a) Eu^{3+} and (b) Tb^{3+} rare-earth ions embedded in $x\text{PbO} + (1-x)\text{B}_2\text{O}_3$ glass matrix (points). (a) The solid curve displays the best least-squares fit of the experimental data with the virtual-cavity model; the dashed curve corresponds to the fit with the real-cavity model. Reproduced with permission from Fig. 2(b), Ref. [23]. Copyright 2003 by the American Physical Society (<http://link.aps.org/doi/10.1103/PhysRevLett.91.203903>). (b) The dashed curve represents the best least-squares fit with the virtual-cavity model; the solid curve displays the fit with the real-cavity model. Reproduced with permission from Fig. 4, Ref. [67]. Copyright 2009 by Elsevier (<http://dx.doi.org/10.1016/j.optmat.2008.10.010>).

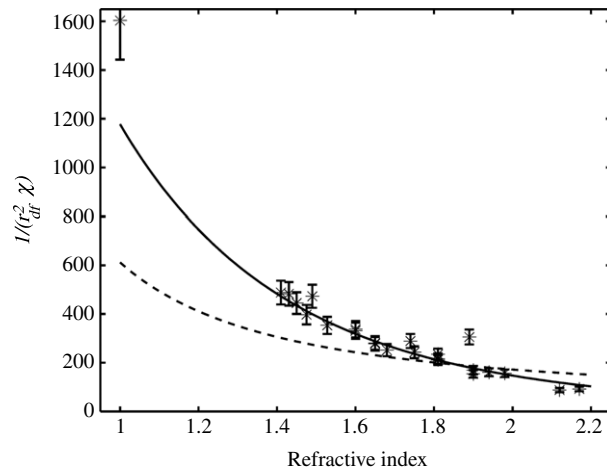
Figure 6



(a) Experimentally measured radiative lifetime of organically capped CdTe quantum dots suspended in different liquids. Reproduced with permission from Fig. 2, Ref. [28]. Copyright 2004 by the American Institute of Physics (<http://link.aip.org/link/doi/10.1063/1.1773154>). (b) A reinterpretation of the experimental results shown in part (a) by Duan *et al.* [25]. The small squares represent the experimental data. The stars and crosses correspond to the best least-squares fit with the real-cavity model for the values of the quantum yield $\eta = 0.55$ and $\eta = 0.90$, respectively. Reproduced with permissions from Fig. 4, Ref. [25]. Copyright 2005 by Elsevier (<http://dx.doi.org/10.1016/j.physleta.2005.06.037>).

A situation where the virtual-cavity model is applicable has been realized in Ce^{3+} ions in different solid-state matrices [25]. The experimental data and the best least-squares fit with the virtual-cavity

Figure 7



Experimentally measured radiative lifetimes of Ce^{3+} ions embedded in different solid-state matrices. The solid curve shows the best least-squares fit to the virtual-cavity model, while the dashed curve corresponds to the fit to the real-cavity model. Reproduced with permissions from Fig. 2, Ref. [25]. Copyright 2005 by Elsevier (<http://dx.doi.org/10.1016/j.physleta.2005.06.037>).

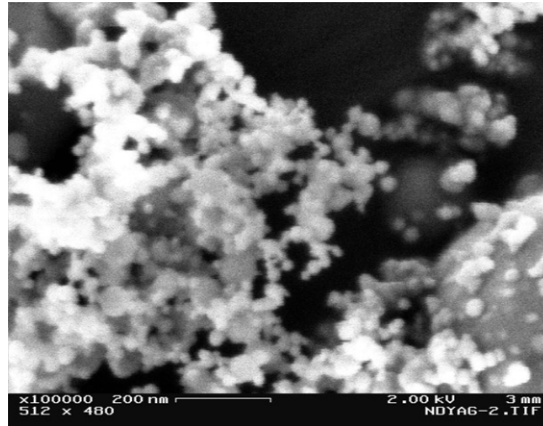
model is represented in Fig. 7. In all the hosts, the low-polarizability Ce^{3+} ions interstitially replace cations with low polarizability, thus not influencing the correlations between the rest of the particles. The virtual-cavity model for the local field is thus applicable in this physical situation.

In [62], Kuznetsov *et al.* applied their microscopic model, given by Eq. (37), to fit the experimentally measured radiative lifetime of Eu^{3+} [23] and Tb^{3+} [67] ions in a binary glass matrix $x\text{PbO}-(1-x)\text{B}_2\text{O}_3$ and liquid suspensions of quantum dots [28]. Their theory provides an excellent description for both kinds of systems, while the real-cavity model originally applied to describe the data [23,28,67] works better for the ions in a binary glass matrix [23,67]. The excellent agreement of the microscopic theory proposed in [62] with the experimental data obtained in the liquid suspensions of quantum dots can be attributed to the fact that Kuznetsov *et al.* account for the self-action of the emitter through the change of its local environment. This is exactly the case with the quantum dots that have a very high polarizability.

3.4. Radiative Lifetime of Liquid Suspensions of Nd^{3+} :YAG Nanoparticles

The experiments on the radiative lifetime measurements are similar. To provide more detail on the specifics of this kind of experiment, we overview our experiment on the radiative lifetime measurement of Nd^{3+} :YAG nanoparticles dispersed in different liquids [29]. The goal of our experiment was to measure the change in the radiative lifetime of emitters caused by local-field effects and to establish which model for

Figure 8



Scanning electron microscope picture of Nd:YAG nanopowder. The average particle size is 20 nm. Reproduced from Fig. 1, Ref. [29] (<http://dx.doi.org/10.1364/JOSAB.24.000516>).

the local-field correction factor works best in this case. We also comment on possible difficulties and uncertainties that one can encounter in this kind of experiment which can complicate the data analysis.

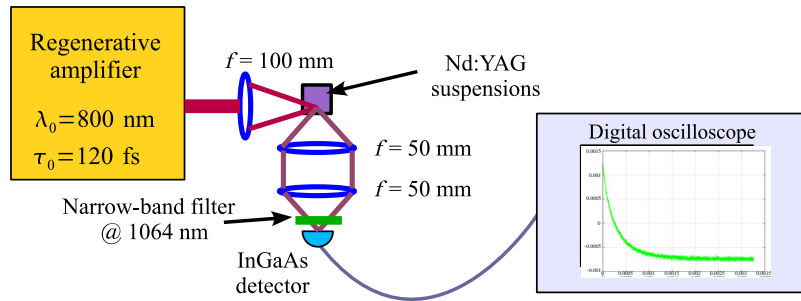
3.4a. Sample Preparation and Experiment

The Nd:YAG nanopowder used in our experiment has an average particle diameter of approximately 20 nm (see the scanning electron microscope image in Fig. 8). The neodymium concentration was chosen to be 0.9 at.%, which is the standard value for Nd:YAG laser rods. We used different organic and inorganic liquids with appropriate surfactants in order to achieve stable suspensions of the nanoparticles. The refractive indices of the liquids ranged between 1.329 (methanol) and 1.63 (CS₂). The Nd:YAG volume fraction in all the samples was 0.11 vol.%.

As the volume fraction f_i of the nanoparticles in our samples is very low, we can treat our suspensions as Maxwell–Garnett-type composite materials and use relation (15) to calculate the effective refractive index n_{eff} , substituting the refractive index of the liquids in place of the host refractive index, $n_h^2 = \epsilon_h$, and the YAG refractive index in place of that of the inclusions, $n_i^2 = \epsilon_i$. The effective refractive indices of our samples are very close to the refractive indices of the liquids.

We used a Spectra Physics femtosecond laser system to optically excite neodymium ions in the Nd:YAG nanoparticle suspensions. The scheme of the experimental setup is represented in Fig. 9. The excitation wavelength was 800 nm, which coincided with a Nd:YAG absorption peak. The pump radiation was focused into a cell containing the suspension, and the fluorescence from the Nd:YAG nanoparticles was collected in a perpendicular geometry. An InGaAs detector and a digital oscilloscope were used to observe and record the fluorescence decay curves. A narrowband 10 nm FWHM filter with the central wavelength

Figure 9



Experimental setup for measuring the radiative lifetime in liquid suspensions of Nd:YAG nanoparticles.

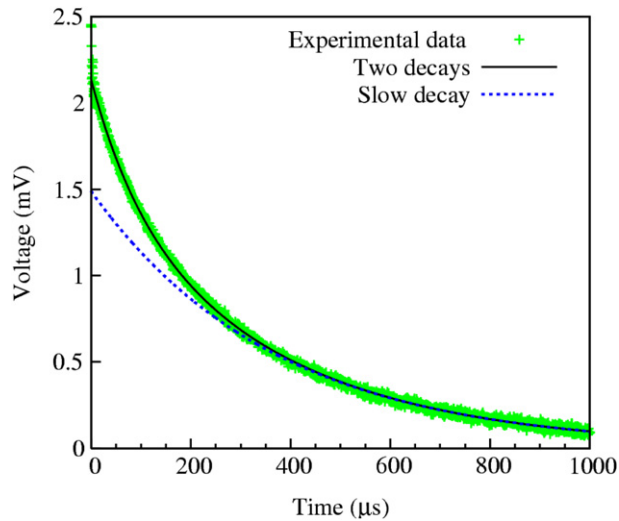
of 1064 nm, together with an additional long-pass filter, were placed in front of the detector to block scattered pump radiation.

3.4b. Bi-exponential Fluorescence Lifetime

A typical time trace showing the fluorescence decay dynamics is shown in Fig. 10. In all our experiments we observed a nonexponential decay, and our data can be fitted well with a sum of two exponentials with a 4:1 ratio of the slower to the faster decay times. All the slower decay exponentials have fluorescence decay times longer than the typical value of $230 \mu\text{m}$ for bulk Nd:YAG, while all the faster decay exponentials have decay times shorter than that of bulk Nd:YAG. We expect the fluorescence decay times in our Nd:YAG nanopowder suspensions to be longer than that in a bulk Nd:YAG crystal, because the effective refractive indices of our liquid suspensions (1.32–1.63) are smaller than the refractive index of a bulk Nd:YAG (1.82).

The most likely reason for the faster exponential in the fluorescence decay in our samples is the contribution from ions sitting on the surfaces of the nanoparticles. To test this hypothesis, we measured the fluorescence lifetimes not only for the Nd:YAG nanopowder, but also for an Nd:YAG micropowder with a micrometer-scale particle size. We obtained the micropowder by crushing an Nd:YAG laser rod and grinding the pieces in a ball mill. The resultant decay dynamics displayed a bi-exponential character in both powders. The shorter decay time ($130 \mu\text{s}$) was the same for both powders (within the error of our measurements), and the longer decay time was around $600 \mu\text{s}$ for the nanopowder and more than two times shorter ($270 \mu\text{s}$) for the micropowder. Furthermore, the relative contribution of the faster-decay exponential was much higher for the nanopowder, compared with that of the micropowder. The facts that the shorter lifetime is the same for both powders and that the faster-exponential amplitude is relatively higher for the nanopowder suggest that the faster exponential in the fluorescence decay is due to the contribution from the Nd^{3+} ions sitting on the surfaces of the particles. Indeed, the structures of the surfaces of the nanoparticles and microparticles should be similar, while the relative surface area of the nanopowder is much larger than that of the micropowder. The crystal lattice surrounding of the surface ions is

Figure 10



Typical fluorescence decay in the Nd:YAG nanopowder. Reproduced from Fig. 3, Ref. [29] (<http://dx.doi.org/10.1364/JOSAB.24.000516>).

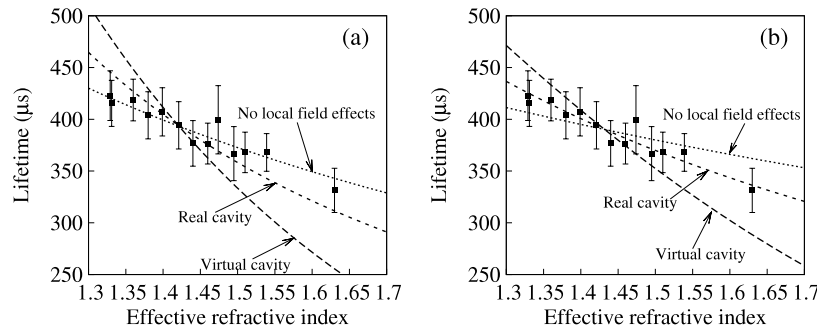
distorted, leading to the variations in their electric dipole moments and resulting in much shorter relative decay times.

The observation of a biexponential fluorescence decay in rare-earth-doped nanoparticles has also been reported by other authors. In Ref. [68], Meltzer *et al.* investigated the effect of the surrounding amorphous matrix on the radiative lifetime of the embedded rare-earth-doped nanoparticles. The authors studied the fluorescence dynamics of $\text{Eu}^{3+}:\text{Y}_2\text{O}_3$ nanoparticles and Pr^{3+} - and Ho^{3+} -doped LaF_3 nanocrystals of different sizes, ranging between 10 and 25 nm. They found that the reduction of an ideal crystal symmetry increases the probability of the radiative transition, resulting in the appearance of the shorter decay component in the measured radiative lifetime. In their recent studies of the luminescent properties of $\text{Yb}^{3+}:\text{Y}_2\text{O}_3$ nanoparticles [69], Amans *et al.* comment on the existence of the crystal field fluctuations for the rare-earth ions sitting close to the surface of the nanoparticles. These crystal field fluctuations are due to an additional pressure induced by the surface strengths that appear when the size of the particles is very small [70] and do not occur in bulk crystals [69]. Because of the high surface-to-volume ratio, a large number of rare-earth emitters sit close to the surface of the nanoparticles and thus significantly contribute to the fluorescence dynamics of a composite material, exhibiting the shorter radiative decay time.

3.4c. Data Analysis

The fluorescence lifetimes for the various host liquids (shown as points in Fig. 11) are obtained by fitting the time evolution of the fluorescence decay to the sum of two exponentials and taking the longer decay time as the relevant time for the reasons explained above. As the results of the fitting procedure were somewhat sensitive to the range of time values

Figure 11



Experimentally measured radiative lifetimes of the Nd:YAG-nanopowder suspensions (points with error bars), and the best least-squares fits with various models (curves) under the assumption that the quantum yield of the nanopowder is (a) 1 and (b) 0.48. Reproduced from Fig. 4, Ref. [29] (<http://dx.doi.org/10.1364/JOSAB.24.000516>).

used in the fitting procedure, we repeated the fit for several different time ranges for each data point. The data points shown in Fig. 11 represent averages of the results of these fits, and the error bars represent the standard deviations from the mean values.

Using Eq. (39), we fitted our experimental data with the “no local-field effects,” [Eq. (33)], virtual-cavity [Eq. (34)], and real-cavity [Eq. (35)] models to find the best least-squares fit to our data. Reported values of the quantum yield of Nd:YAG range from 0.48 (see Ref. [71]) to 0.995 (see Ref. [72]), with 0.6 being the value most often reported [73–75]. It appears that the quantum yield for a given sample depends sensitively on Nd concentration and on environment. For this reason, we have fitted our data to the three models, using the quantum yield as an additional adjustable parameter. We thus find it plausible to present our experimental data together with the results of the least-squares fits for the two limiting values of reported quantum yields, namely 1 and 0.48 in Figs. 11(a) and 11(b), respectively. Through visual inspection of these results, one can immediately rule out the virtual-cavity model. Under the assumption $\eta = 1$, both the real-cavity and the no-local-field-effects models agree reasonably well the experimental data, with the no-local-field-effects model providing a slightly better fit [see Fig. 11(a)]. For the other limiting case, with the assumption that $\eta = 0.48$ [see Fig. 11(b)], the real-cavity model gives the best fit, which agrees with our expectations based on the theoretical analysis performed in Ref. [5]. The no-local-field-effects model lies close to our experimental data as well. However, there is no theoretical justification for assuming the validity of the no-local-field-effects model, as the physical properties of our samples were such that local field effects should have been present. That is, the sizes of the particles were more than 30 times smaller than the wavelength of light. Also the dispersions were stable in most of the samples, which indicates that even if some particle aggregation had occurred, the aggregates would still have been smaller than the wavelength of light.

In Ref. [54], Pukhov *et al.* used their model of the local-field-corrected radiative lifetime in spherical inclusions dispersed in a host, given by Eq. (38), to reinterpret the experimental data shown in Figs. 11 and 4. This choice of the theoretical model is physically meaningful for liquid suspensions of nanoparticles. However, using the volume fraction of the spherical inclusions (nanoparticles) as a free fitting parameter did not result in good agreement with the experimental data in Fig. 11. Moreover, the volume fraction values, obtained from the model, were reaching 0.2–0.4, while the actual volume fraction of Nd:YAG nanoparticles in our samples was $f_i \approx 0.001$. A possible way to improve the agreement between the theory proposed by Pukhov *et al.* and our data could be returning to the original expression in terms of A_{vac} , given by Eq. (27). Expressing explicitly $L_{\text{bulk}} = (\varepsilon_i + 2)/3$ in terms of the dielectric constant ε_i of the inclusions, one can set $\tau_{\text{vac}} = (A_{\text{vac}})^{-1}$ as a free fitting parameter while using the known value of the inclusion volume fraction as a fixed parameter. A similar theoretical approach, developed for calculating the local-field-corrected laser gain coefficient in various composite geometries, is discussed in the next section.

4. Influence of Local-Field Effects on Basic Laser Parameters

In this section, we discuss how local-field effects and composite optical materials can be applied to control and tailor the basic laser properties of laser gain media, such as the radiative lifetime of the upper laser level, the small-signal gain coefficient, and the saturation intensity. We first provide an overview of a proof-of-principle study aimed at demonstrating the idea of the composite laser in Subsection 4.1 and show the significance of the local-field effects in modifying the laser properties. Local-field effects can come into play differently in different composite geometries, and separate theoretical studies of the laser properties of various composite geometries are needed. We provide a recipe for developing such theories in Subsection 4.2. Using examples, we also analyze the small-signal gain coefficient in layered and Maxwell Garnett composite geometries.

4.1. Idea of the Composite Laser

The basic operation of lasers can be characterized most simply in terms of the upper-level spontaneous emission lifetime τ , the laser gain coefficient g , and the gain saturation intensity I_s . Control of the three laser parameters is crucial for the development of laser systems for the following reasons. (1) The upper state lifetime controls how large the pumping rate of the laser needs to be in order to establish a population inversion. (2) The gain coefficient determines the laser threshold condition. The gain needs to be large enough for the laser to reach threshold, but it is not desirable for the gain to be too large because excessive gain can lead to the development of parasitic effects such as amplified spontaneous emission. (3) The saturation intensity (and its related energy quantity, the saturation fluence) determine the output power of a laser, from the point of view that the output power

is determined by the condition that the saturated round-trip gain must equal the round-trip loss. In practice, the output intensity of most lasers is typically a factor of several times the saturation intensity. All three of these parameters can be controlled through use of a composite material geometry. In order to show the significance of local-field effects in modifying laser properties of composite optical materials, we developed in [76] a simple theoretical study aimed at presenting a general picture.

In this section, we summarize the idea of the composite laser reported in [76]. For illustrative purposes, we treat a composite laser gain medium as an effective medium and assume that the amplification (and loss) at the laser transition frequency is small enough to neglect the imaginary part of the effective dielectric constant ϵ_{eff} . We also assume that the local-field effects in our effective medium can be accounted for using the Lorentz model of the local field. This allows us to express the local-field correction factor as $L = (n_{\text{eff}}^2 + 2)/3$. In this simplest formulation of local-field effects, we obtain the expressions for the laser parameters as functions of n_{eff} [18,76]:

$$\tau_{\text{loc}} = \frac{\tau_{\text{vac}}}{n_{\text{eff}}|L|^2}, \quad (42a)$$

$$g_{0, \text{loc}} = \frac{|L|^2}{n_{\text{eff}}} g_{0, \text{vac}}, \quad (42b)$$

$$I_{s, \text{loc}} = n_{\text{eff}}^2 I_{s, \text{vac}}. \quad (42c)$$

Equations (42) thus relate the basic laser parameters in a composite dielectric medium to their “vacuum” counterparts.

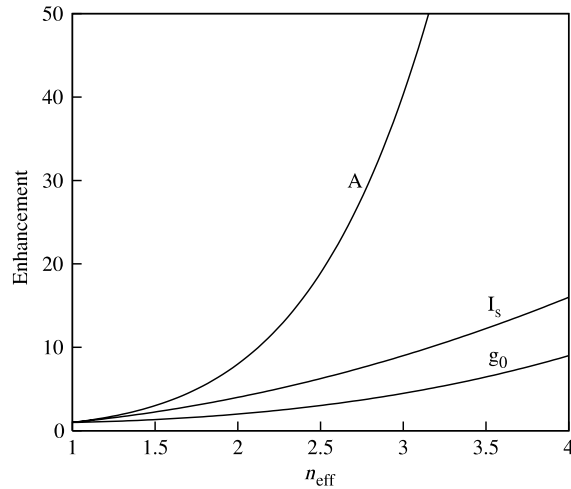
In Fig. 12, we plot the enhancement factors, which are the ratios between the basic laser parameters and their vacuum counterparts, as functions of n_{eff} . We choose the range of refractive indices available in dielectric composite materials. Clearly, significant control over the laser parameters is available through use of a composite geometry. Since the rates of change of the laser parameters with n_{eff} are very different, it is possible to control the radiative lifetime, gain coefficient, and saturation intensity almost independently. The approach described in this section is general to all composite geometries for the linear optical regime and can only be used to estimate the linear laser properties. More specific separate models are needed for a more precise evaluation of the basic laser parameters of different composite geometries.

4.2. Laser Gain Properties of Composite Optical Materials

The Lorentz model of the local field has been shown to be applicable to homogeneous media [5]. However, local-field effects can manifest themselves differently in composite materials, and separate theoretical models for describing the laser properties of different composite geometries [17] are needed. Such models have been developed in Ref. [44] for layered and Maxwell Garnett composite geometries. Here we give a generalized recipe, derived from Ref. [44], for assessing the laser properties of an arbitrary composite geometry.

In order to demonstrate our model, in Subsection 4.2a we derive the local-field-corrected small-signal gain coefficient for homogeneous

Figure 12



Variation of the principal parameters that control the basic operation of a laser with the effective refractive index of the composite material. $A = 1/\tau$ is the Einstein A coefficient. Reproduced from [76] (<http://dx.doi.org/10.1364/JOSAB.24.000A19>).

materials. We give a recipe for extending the model to the case of composite materials, while omitting the derivations and lengthy final expressions. Instead, we give examples in Subsections 4.2c and 4.2d of applying the models to describe the small-signal gain coefficients in layered and Maxwell Garnett composite materials.

We consider a two-component nanocomposite optical material with resonant emitters in one of the constituents. There are two mechanisms contributing to the local field acting on the emitters in such a material system: (i) the local environment within the constituent containing the emitters, and (ii) the geometry of the composite material.

4.2a. Influence of Local Environment

The influence of the local environment on the electric field acting on an emitter in a resonant constituent can be taken into account by treating the constituent as a homogeneous material and applying an appropriate model, such as Lorentz model of local field. This model can be applied to describe the majority of homogeneous solids, such as rare-earth-doped laser materials. The Lorentz model of the local field in its simplest formulation [Eq. (2)] is applicable to the case of “pure resonant emitters” (PREs) in which all atoms are of the same sort. However, when dealing with laser gain media, it is more typical to have a system with atoms or molecules of two or more sorts. Therefore, it is useful to distinguish the case in which one has a background (host) material with the transition frequencies far from that of the optical field, doped with some portion of atoms with a transition frequency in resonance with the optical field. We refer to this case as “resonant emitters in a background” (REB).

Pure Resonant Emitters. We first consider a PRE medium illuminated by an optical field of frequency ω . We assume that the field is tuned close to a resonance of the emitters. In that case we can treat the medium roughly as a collection of TLAs, and can apply a well-known formalism, based on the Maxwell–Bloch equations [77]

$$\dot{\sigma} = \left(i\Delta - \frac{1}{T_2} \right) \sigma - \frac{1}{2} i\kappa E w \quad (43a)$$

and

$$\dot{w} = -\frac{w - w_{\text{eq}}}{T_1} + i(\kappa E \sigma^* - \kappa^* E^* \sigma) \quad (43b)$$

for coherence σ and population inversion w , to describe the optical properties of such a medium. Here $E(t)$ is the slowly varying amplitude of the macroscopic electric field $\tilde{E}(t) = E(t) \exp(-i\omega t) + \text{c.c.}$. The polarization $\tilde{P}(t) = P(t) \exp(-i\omega t) + \text{c.c.}$ involves

$$P(t) = N\mu^* \sigma(t), \quad (44)$$

where N is the number density of atoms, μ is the transition dipole moment of the two-level system from the ground to excited state, and $\sigma(t)$ is the slowly varying amplitude of coherence $\tilde{\sigma}(t)$, that is,

$$\tilde{\sigma}(t) = \sigma(t) \exp(-i\omega t). \quad (45)$$

In Eqs. (43), $\kappa = 2\mu/\hbar$, $\Delta = \omega - \omega_0$ is the detuning of the optical field frequency ω from the atomic resonance frequency ω_0 , T_1 and T_2 are, respectively, the population and coherence relaxation times, and w_{eq} is the equilibrium value of the population inversion (*e.g.*, in the case of an uninverted system, $w_{\text{eq}} = -1$).

We insert the Lorentz local field (2) into the Maxwell–Bloch equations (43) and obtain

$$\dot{\sigma} = \left(i\Delta + i\Delta_L w - \frac{1}{T_2} \right) \sigma - \frac{1}{2} i\kappa w E \quad (46a)$$

and

$$\dot{w} = -\frac{w - w_{\text{eq}}}{T_1} + i(\kappa E \sigma^* - \kappa^* E^* \sigma). \quad (46b)$$

As a result of the Lorentz local field correction, an inversion-dependent frequency shift $\Delta_L w$ appears in Eq. (46a). It involves shifting of the resonance of the atomic transition. Here Δ_L is known as Lorentz redshift [78] and is given by

$$\Delta_L = -\frac{4\pi}{3} \frac{N|\mu|^2}{\hbar}. \quad (47)$$

The slowly varying amplitude P of the macroscopic polarization can be expressed in terms of the linear susceptibility $\chi^{(1)}$ as $P = \chi^{(1)} E$. We find

from Eq. (44) that

$$\chi^{(1)} = \frac{N\mu^*\sigma}{E}. \quad (48)$$

Substituting the steady-state solution of Eq. (46a) [44,79] for the coherence σ yields

$$\chi^{(1)} = \frac{N|\mu|^2}{\hbar} \frac{w_{\text{eq}}}{\Delta + \Delta_L w_{\text{eq}} + i/T_2}. \quad (49)$$

Now we can find the small-signal gain (g_0) and absorption (α_0) coefficients of the medium, as they are proportional to the imaginary part of the linear susceptibility:

$$g_0 = -\alpha_0 = -\frac{4\pi\omega}{c\sqrt{\varepsilon}} \text{Im} \chi^{(1)}. \quad (50)$$

The dielectric permittivity ε entering Eq. (50) describes the dielectric properties of the entire material structure away from its resonances.

Resonant Emitters in a Background. For a REB medium, we can split the total polarization entering Eq. (2) for the Lorentz local field (we call it P_{tot} from now on) into a contribution P_{bg} coming from the atoms of the background medium and a contribution P_{res} from the resonant atoms:

$$P_{\text{tot}} = P_{\text{bg}} + P_{\text{res}} = N_{\text{bg}} \alpha_{\text{bg}} E_{\text{loc}} + N_{\text{res}} \mu_{\text{res}}^* \sigma_{\text{res}}, \quad (51)$$

where α_{bg} is the polarizability of a background atom. Here and below the parameters with the subscripts “bg” and “res” refer to the background and resonant atoms or molecules of the medium. As we consider only media in which the Lorentz model of the local field is valid, both resonant and background types of molecules or atoms should experience the same Lorentz local field.

One can relate the polarizability α_{bg} to the dielectric constant of the background material ε_{bg} by using the Clausius–Mossotti (or Lorentz–Lorenz) relation (8):

$$\frac{\varepsilon_{\text{bg}} - 1}{\varepsilon_{\text{bg}} + 2} = \frac{4\pi}{3} N_{\text{bg}} \alpha_{\text{bg}}. \quad (52)$$

Substituting Eq. (51) into Eq. (2) for the local field and using the Clausius–Mossotti relation (52) and Eq. (11) for the local-field correction factor, we find

$$E_{\text{loc}} = L_{\text{bg}} \left(E + \frac{4\pi}{3} P_{\text{res}} \right), \quad (53)$$

where $L_{\text{bg}} = (\varepsilon_{\text{bg}} + 2)/3$ is the Lorentz local-field correction factor for the background material. The current expression for the local field reduces to Eq. (2) if one considers a vacuum to be a background medium.

Next, we find the susceptibility of the medium from the relationship $\chi^{(1)} = P_{\text{tot}}/E$. Substituting Eq. (51) and the steady-state solution for σ_{res}

into the above relationship for $\chi^{(1)}$, we arrive at the result

$$\chi^{(1)} = \chi_{\text{bg}}^{(1)} + \frac{N_{\text{res}} |\mu_{\text{res}}|^2}{\hbar} \frac{L_{\text{bg}}^2 w_{\text{eq, res}}}{\Delta + \Delta'_L w_{\text{eq, res}} + i/T_{2, \text{res}}} \quad (54)$$

for the linear susceptibility of the REB medium. The frequency shift Δ'_L is a modified Lorentz redshift, given by

$$\Delta'_L = -\frac{4\pi}{3} \frac{N_{\text{res}} |\mu_{\text{res}}|^2}{\hbar} L_{\text{bg}} = L_{\text{bg}} \Delta_L. \quad (55)$$

The Lorentz redshift thus appears to be enhanced by L_{bg} owing to the influence of the background dielectric medium. Using Eqs. (50) and (54), we can find the small-signal gain and absorption coefficients.

The result [Eq. (55)] for the Lorentz redshift modified by the presence of the background medium is in agreement with that obtained by Crenshaw and Bowden [57,80] for a collection of resonant TLAs embedded into a dielectric background. Knoester and Mukamel [65], however, obtained a different enhancement factor for the Lorentz redshift in a similar system. Their result shows frequency shift enhancement by the refractive index of the background n_{bg} only.

4.2b. Influence of Composite Geometry

We consider a two-component nanocomposite optical material comprised of homogeneous media a and b , and we assume that the resonant emitters are present in constituent a only. Constituent a can be of either PRE or REB type. In the case of a composite material, Eqs. (2) and (53), describing the Lorentz local field in homogeneous media of PRE and REB types, take the forms

$$\mathbf{E}_{\text{loc}, a} = \mathbf{e}_a + \frac{4\pi}{3} \mathbf{p}_a \quad (56)$$

and

$$\mathbf{E}_{\text{loc}, a} = L_{\text{bg}, a} \left(\mathbf{e}_a + \frac{4\pi}{3} \mathbf{p}_a \right), \quad (57)$$

respectively. Here \mathbf{e}_a and \mathbf{p}_a are the average (mesoscopic) field and polarization within component a , influenced by the mesoscopic field and polarization of component b , and thus by the geometry of the composite material. Applying the models developed for the specific composite geometries [17,30,32], one can express \mathbf{e}_a and \mathbf{p}_a in terms of the average macroscopic field E and polarization P of the entire composite material. Equations (56) and (57) thus describe the local field acting on the emitters in a composite material of an arbitrary geometry. Substituting the local field in the form of Eqs. (56) and (57) into the Maxwell–Bloch equations (46), one can solve them to find $\chi^{(1)}$ and, from there, the local-field-corrected gain and absorption coefficients for composite optical materials with PRE and REB types of resonant constituent [44].

4.2c. Laser Gain Properties of Layered Composite Materials

Here we consider a layered composite material comprising two types of homogeneous media (we call them a and b) with different optical properties [see Fig. 1(c)]. Let us assume that both components a and b of our layered composite material respond linearly to the applied optical field, and we consider only the components of electric field and polarization perpendicular to the layers. Assume that the field of frequency ω is tuned close to one of the resonances of the component a , but does not coincide with any of the resonances of the component b . The detailed derivation of the linear susceptibility and local-field-induced frequency shift for the layered composite material can be found in [44]. Here we present an example of how the model can be applied to analyze the laser gain properties of a layered composite material.

As an example, we analyze the behavior of the small-signal gain as a function of various parameters, choosing a Rhodamine 6G-doped poly(methyl methacrylate) (PMMA) laser gain medium as the resonant species a in our layered composite material. The parameters of the gain medium that we used for our analysis are the emission peak wavelength $\lambda_0 = 590$ nm, the transverse relaxation time $T_2 = 100$ fs, the transition cross section $\sigma_{\text{tr}} = 2 \times 10^{-16}$ cm², the Rhodamine molecular concentration $N = 1.8 \times 10^{18}$ cm⁻³, and the refractive index of PMMA, $n_{\text{bg}} = 1.4953$. We take the component b to be an unknown material and vary its refractive index to see how it affects the optical response of Rhodamine-doped PMMA.

Rhodamine-doped PMMA is an example of the REB case, and, therefore, one should use Eq. (57) for the local field acting on the Rhodamine molecules. The expression for the mesoscopic field in a constituent of a two-component layered composite material has been derived in [32]. In the linear optical regime, it takes the form

$$e_a = \frac{\varepsilon_{\text{eff}}}{\varepsilon_a} E. \quad (58)$$

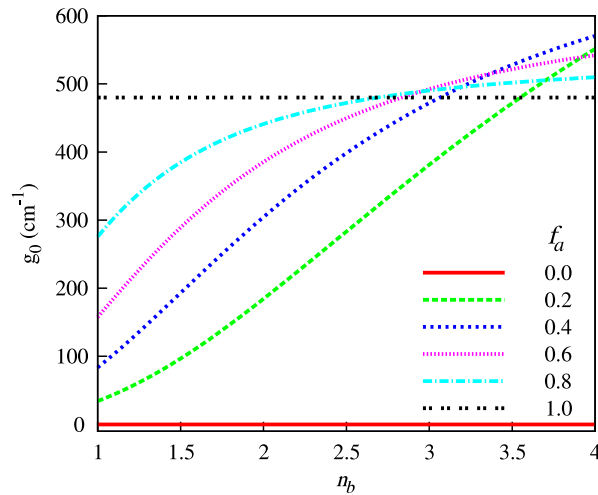
We have dropped the vector notation, as we treat only the component of the electric field that is perpendicular to the layers. Alternatively, one can also express the mesoscopic field in the resonant constituent a as [44]

$$e_a = \frac{\varepsilon_b}{1 + 4\pi f_a \chi_b^{(1)}} E - \frac{4\pi f_b}{1 + 4\pi f_a \chi_b^{(1)}} p_a \quad (59)$$

in terms of the macroscopic field and mesoscopic polarization p_a . Substituting Eq. (59) into the local field [Eq. (57)], and then Eq. (57) into the Maxwell–Bloch equations (46), and following the recipe given in Subsection 4.2a, one can find the expression for the small-signal gain coefficient [44].

Setting the equilibrium value of the population inversion $w_{\text{eq}} = 1$, which corresponds to a fully inverted amplifying system, and the detuning of the optical field with respect to the resonance $\Delta = 0$, we plot the small-signal gain, calculated by using the method described above, as a function of the refractive index of the nonresonant component n_b in Fig. 13, and of f_a in Fig. 14. It can be seen from Figs. 13 and 14 that the

Figure 13



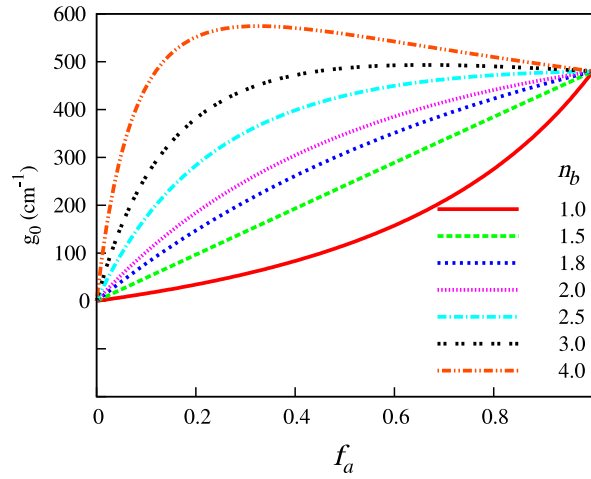
Small-signal gain of a layered composite material as a function of the refractive index of the nonresonant component for different values of the volume fraction of the resonant component. Reproduced with permission from Fig. 3(a), Ref. [44] (<http://dx.doi.org/10.1088/1464-4258/11/2/024002>).

gain coefficient tends to grow with the increase of the refractive index of the nonresonant component. The reason for this behavior is that for the light polarized perpendicular to the layers, the electric field tends to localize in the regions of a dielectric with lower refractive index [32]. Therefore, the higher the refractive index of the nonresonant layers, the more the electric field is displaced into the resonant layers, which causes a stronger gain. The behavior of the gain coefficient as a function of f_a is more complex. It grows monotonically with the increase of f_a for small refractive indices. In the case $n_b = n_{bg}$ the growth is linear. For high values of the refractive index the small-signal gain displays a rapid growth with the increase of the volume fraction until it reaches a maximum value, corresponding to an optimal value of f_a , after which it starts to decrease with further increase of f_a . This behavior can be understood as follows. The initial growth of g_0 with f_a is due to the fact that the number of the resonant molecules in the medium increases. On the other hand, by increasing f_a , we make our layers with the resonant molecules thicker, and the local field, highly concentrated in these layers because of the high value of n_b , spreads over the layers, and each individual molecule “feels” a smaller value of the local field. This causes the gain to decrease with the increase of f_a beyond an optimal value. Thus, in order to achieve maximum gain or absorption in a layered composite material, one needs to use a nonresonant component with a high refractive index while keeping the volume fraction of the resonant component low.

4.2d. Laser Gain Properties of Maxwell Garnett Composite Materials

The Maxwell Garnett type of composite geometry is a collection of small particles (the inclusions) distributed in a host medium [see Fig. 1(a)].

Figure 14



Small-signal gain of a layered composite material as a function of the volume fraction of the resonant component for different values of the refractive index of the nonresonant component. Reproduced with permission from Fig. 4, Ref. [44] (<http://dx.doi.org/10.1088/1464-4258/11/2/024002>).

The effective dielectric constant of a Maxwell Garnett composite material is described by Eq. (15). Because of the geometry of Maxwell Garnett composite materials, the local field is uniform in the inclusion medium and nonuniform in the host [30]. We review only the results obtained in Ref. [44] for the case of resonant species in inclusions. Following the recipe reported in [44], one can numerically solve the problem to deduce the total susceptibility and associated frequency shift of the resonant feature for the case of the resonant species in the host material.

As an example, we consider a Maxwell Garnett composite material with Nd:YAG nanoparticles as inclusions. We use the emission wavelength $\lambda_0 = 1.064 \mu\text{m}$, the transverse relaxation time $T_2 = 3 \text{ ms}$, the transition cross section $\sigma_{\text{tr}} = 4.6 \times 10^{-19} \text{ cm}^2$, the neodymium atomic concentration $N = 1.37 \times 10^{20} \text{ cm}^{-3}$ (this value corresponds to 1 at.% of Nd in YAG), and the YAG refractive index $n_{\text{bg}} = 1.82$. We take the host to be an unknown medium and vary its refractive index n_h to see how it affects the optical response of Nd:YAG nanoparticles.

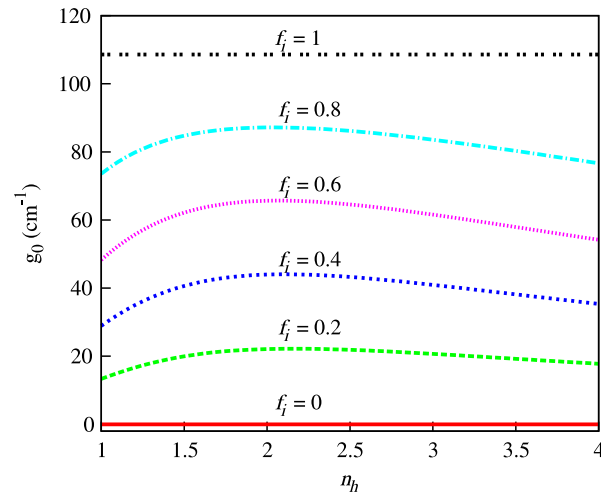
Nd:YAG corresponds to the case of REB, which means that the gain coefficient can be calculated substituting Eq. (57) for the local field acting on the Nd^{3+} ions. The mesoscopic field inside the inclusions can be expressed as [30]

$$\mathbf{e}_i = \frac{\varepsilon_{\text{eff}} + 2\varepsilon_h}{\varepsilon_i + 2\varepsilon_h} \mathbf{E}, \quad (60)$$

or as [44]

$$e_i = \frac{3\varepsilon_h}{3\varepsilon_h - 4\pi f_h \chi_h^{(1)}} \left[E - \frac{4\pi}{3\varepsilon_h} f_h p_i \right] \quad (61)$$

Figure 15



Small-signal gain of a Maxwell Garnett composite material as a function of the refractive index of the nonresonant host for different values of the inclusion volume fraction. Reproduced with permission from Fig. 6, Ref. [44] (<http://dx.doi.org/10.1088/1464-4258/11/2/024002>).

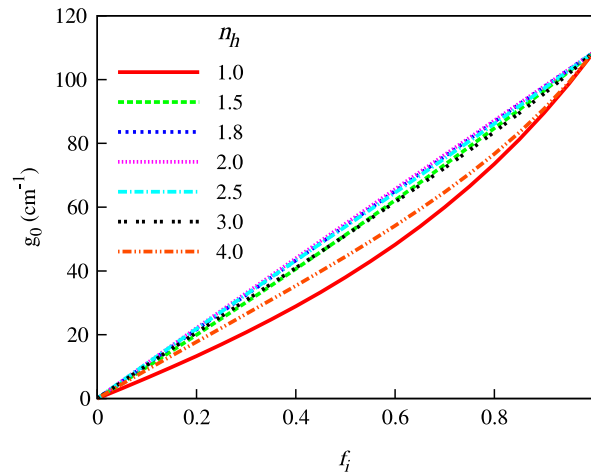
in terms of the mesoscopic polarization. We dropped the vector notation in Eq. (61) as the mesoscopic field inside the inclusion is uniform, and the inclusion material is assumed to be isotropic. Substituting the mesoscopic field [Eq. (61)] into the local field [Eq. (57)], and Eq. (57) into the Maxwell–Bloch equation (46), one can solve them and find the small-signal gain coefficient.

Setting the equilibrium value of the population inversion $w_{\text{eq}} = 1$ and the detuning $\Delta = 0$, we plot the small-signal gain coefficient as a function of the host refractive index n_h in Fig. 15. The dependence of g_0 on the inclusion volume fraction f_i is depicted in Fig. 16.

One can see from Figs. 15 and 16 that the small-signal gain of the Maxwell Garnett composite geometry exhibits a monotonic growth with the increase of f_i . It increases to some maximum value with the increase of the host refractive index and then decreases with further growth of n_h . The monotonic growth of g_0 with f_i is due to the fact that, unlike in layered composite materials, the increase of the inclusion volume fraction in the Maxwell Garnett composite material is not accompanied by the decrease in the local field in an inclusion. The reason for the complex behavior of g_0 as a function of n_h is as follows. It is seen from Eq. (50) that $g_0 \propto [\sqrt{\varepsilon_{\text{eff}}}]^{-1} \text{Im} \chi_{\text{eff}}^{(1)}$. Due to the electric field localization in the component with the lower refractive index, $\text{Im} \chi_{\text{eff}}^{(1)}$ monotonically grows with the increase of n_h . However, the term $[\sqrt{\varepsilon_{\text{eff}}}]^{-1}$, where ε_{eff} is given by Eq. (15), decreases with the increase of n_h , and at some value of the host refractive index its decrease overcompensates for the growth of $\text{Im} \chi_{\text{eff}}^{(1)}$. As a result, g_0 starts to decrease with further increase of n_h .

It is important to keep in mind that the Maxwell Garnett model works well only for low volume fractions of the inclusions ($f_i \lesssim 0.4$, and even

Figure 16



Small-signal gain of a Maxwell Garnett composite material as a function of the inclusion volume fraction for different values of the host refractive index. Reproduced with permission from Fig. 7, Ref. [44] (<http://dx.doi.org/10.1088/1464-4258/11/2/024002>).

lower in some cases). It does not account for a percolation phenomenon that occurs when $f_i \gtrsim 0.3$.

5. Nonlinear Optical Properties of Composite Materials

Numerous studies, discussed in the previous sections, have shown that local-field effects can significantly modify the linear optical properties of both homogeneous and composite optical materials. These effects become even more pronounced in the nonlinear optical regime, as the optical response scales with the strength of the local field.

In this section, we provide an overview of how local-field effects can come into play in the nonlinear optical regime. We first present a basic treatment of local-field effects in the nonlinear optics in Subsection 5.1, and then show in Subsections 5.2 and 5.3 how nanostructuring can be utilized to control the nonlinear optical response of materials.

5.1. Local-Field Effects in Nonlinear Optics

In order to demonstrate how local-field effects modify the nonlinear optical susceptibility, we consider here the simplest case of a homogeneous centrosymmetric medium that can be described by the Lorentz model of the local field. We restrict ourselves with treating the lowest-order nonlinear optical interactions at a single frequency, such as degenerate four-wave mixing (DFWM). We thus can limit the consideration to the third order of nonlinearity, and the corresponding power series expansion of the nonlinear optical susceptibility characterizing the medium with respect to the strength of the macroscopic electric field

takes form [81]

$$\chi = \chi^{(1)} + 3\chi^{(3)}|E|^2 + \dots \quad (62)$$

Our goal is to relate the macroscopic characteristics of the medium to the microscopic ones, applicable to individual molecules or atoms. We thus seek the relationships between the linear susceptibility $\chi^{(1)}$ and third-order nonlinear susceptibility $\chi^{(3)}$ of the medium and their microscopic counterparts, namely, the linear polarizability $\gamma_{\text{at}}^{(1)}$ and third-order hyperpolarizability $\gamma_{\text{at}}^{(3)}$. This is where the local-field corrections come into play.

We rewrite expression (2) for the Lorentz local field in terms of the slowly varying amplitudes of the electric field and polarization as

$$E_{\text{loc}} = E + \frac{4\pi}{3}P. \quad (63)$$

The polarization P entering Eq. (63) now contains a nonlinear contribution and can be represented as a sum of the terms proportional to the first and third powers of the local electric field as

$$P = P^{(1)} + P^{(3)} + \dots, \quad (64)$$

where

$$P^{(1)} = N\gamma_{\text{at}}^{(1)}E_{\text{loc}} \quad (65a)$$

and

$$P^{(3)} = N\gamma_{\text{at}}^{(3)}|E_{\text{loc}}|^2E_{\text{loc}}. \quad (65b)$$

Using Eq. (63) in Eq. (65a), we obtain

$$P^{(1)} = \frac{\varepsilon - 1}{4\pi} \left[E + \frac{4\pi}{3}P^{(3)} + \dots \right]. \quad (66)$$

The electric displacement vector D is defined as

$$D = E + 4\pi P = E + 4\pi P^{(1)} + 4\pi P^{(3)} + \dots \quad (67)$$

Substituting Eq. (66) into Eq. (67), we find that

$$D = \varepsilon E + 4\pi P^{\text{NLS}}, \quad (68)$$

where

$$P^{\text{NLS}} = L_{\text{Lor}}(P^{(3)} + \dots) \quad (69)$$

is the nonlinear source polarization, introduced by Bloembergen [82]. Here L_{Lor} is the Lorentz local-field correction factor, given by Eq. (11) in terms of the susceptibility ε of the medium.

Substituting expression (66) for the polarization $P^{(1)}$ into Eq. (64) for the total polarization, we find that

$$P = \chi^{(1)}E + P^{\text{NLS}}. \quad (70)$$

Substituting Eq. (63) for the local field into Eq. (65b) for the polarization $P^{(3)}$ and dropping out the terms scaling with higher than the third power of the electric field, we obtain

$$P^{(3)} = 3N\gamma_{\text{at}}^{(3)}|L_{\text{Lor}}|^2L_{\text{Lor}}|E|^2E. \quad (71)$$

Substituting Eq. (71) into Eq. (69), and Eq. (69) into Eq. (70), we find the total polarization to be

$$P = \chi^{(1)}E + 3N\gamma_{\text{at}}^{(3)}|L_{\text{Lor}}|^2L_{\text{Lor}}^2|E|^2E + \dots. \quad (72)$$

Alternatively, the total polarization can be represented as a Taylor series expansion with respect to the average electric field as

$$P = \chi E = \chi^{(1)}E + 3\chi^{(3)}|E|^2E + \dots. \quad (73)$$

Equating relations (72) and (73), we obtain

$$\chi^{(1)} = N\gamma_{\text{at}}^{(1)}L_{\text{Lor}} \quad (74a)$$

and

$$\chi^{(3)} = N\gamma_{\text{at}}^{(3)}|L_{\text{Lor}}|^2L_{\text{Lor}}^2. \quad (74b)$$

By inspection of Eqs. (74a) and (74b), one can see that the linear optical susceptibility scales as the first power of the local-field correction factor, while the third-order nonlinear optical susceptibility scales as the fourth power of the factor L_{Lor} . This extra power in the expression for $\chi^{(3)}$ stems from the nonlinear source polarization, Eq. (69). The physical implication is that the presence of the nonlinear polarization modifies the linear optical response of the material itself. Clearly, the influence of the local field on the nonlinear optical response is much more significant than on the linear properties, as it depends on the order of the nonlinearity.

5.2. Theoretical Predictions

5.2a. Maxwell Garnett Composite Geometry

A rigorous theoretical model for describing the third-order nonlinear optical interactions in Maxwell Garnett composite material has been developed by Sipe and Boyd in [30]. They consider a degenerate third-order nonlinearity at the same frequency as that of the incident field, such as the Kerr effect. They theoretically describe the cases in which either or both host and inclusion materials exhibit the third-order nonlinear optical response.

We follow the simplified representation used in Ref. [31] to display the key result of the theory reported in [30] for the simplest case of the linear host and nonlinear inclusions. In obtaining this result, the assumption that the host and inclusion materials are isotropic and absorptionless is made. We also assume that the inclusion material is centrosymmetric in that it lacks even-order nonlinear susceptibilities, which implies that $\chi_i^{(3)}$ is the lowest-order nonlinear susceptibility in such a material. As we are

dealing with degenerate nonlinear interactions, we can operate in terms of the slowly varying amplitudes of the electric field and polarization.

We can write the mesoscopic constitutive relation for the inclusions as

$$\mathbf{d}_i = \varepsilon_i \mathbf{e}_i + 4\pi \mathbf{p}_i^{\text{NL}}, \quad (75)$$

where the mesoscopic nonlinear polarization in the inclusion can be expressed as

$$\mathbf{p}_i^{\text{NL}} = A_i (\mathbf{e}_i \cdot \mathbf{e}_i^*) \mathbf{e}_i + \frac{B_i}{2} (\mathbf{e}_i \cdot \mathbf{e}_i) \mathbf{e}_i^*. \quad (76)$$

Here A_i and B_i are the constants specifying the nonlinear optical response of the inclusion material. At the macroscopic level, Eqs. (75) and (76) take the form

$$\mathbf{D} = \varepsilon_{\text{eff}} \mathbf{E} + 4\pi \mathbf{P}_{\text{eff}}^{\text{NL}} \quad (77)$$

and

$$\mathbf{P}_{\text{eff}}^{\text{NL}} = A_{\text{eff}} (\mathbf{E} \cdot \mathbf{E}^*) \mathbf{E} + \frac{B_{\text{eff}}}{2} (\mathbf{E} \cdot \mathbf{E}) \mathbf{E}^*. \quad (78)$$

Here ε_{eff} is the Maxwell Garnett effective dielectric permittivity given by Eq. (15). A_{eff} and B_{eff} characterize the overall nonlinear optical response of the composite material. It can be shown [30] that for the case of a nonlinearity in inclusions,

$$A_{\text{eff}} = f_i \left| \frac{\varepsilon_{\text{eff}} + 2\varepsilon_h}{\varepsilon_i + 2\varepsilon_h} \right|^2 \left(\frac{\varepsilon_{\text{eff}} + 2\varepsilon_h}{\varepsilon_i + 2\varepsilon_h} \right)^2 A_i \quad (79a)$$

and

$$B_{\text{eff}} = f_i \left| \frac{\varepsilon_{\text{eff}} + 2\varepsilon_h}{\varepsilon_i + 2\varepsilon_h} \right|^2 \left(\frac{\varepsilon_{\text{eff}} + 2\varepsilon_h}{\varepsilon_i + 2\varepsilon_h} \right)^2 B_i. \quad (79b)$$

Equations (79) can be rewritten as

$$A_{\text{eff}} = f_i |L_i|^2 L_i^2 A_i \quad (80a)$$

and

$$B_{\text{eff}} = f_i |L_i|^2 L_i^2 B_i \quad (80b)$$

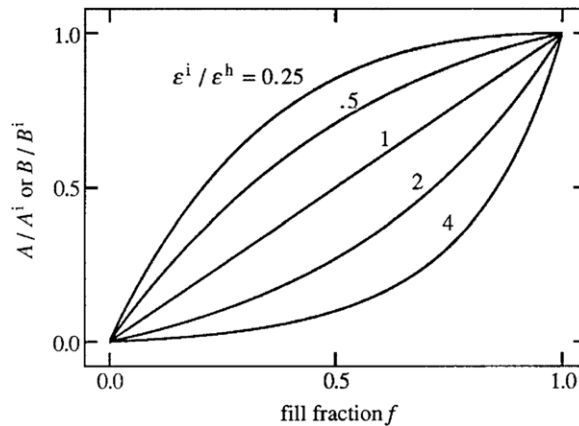
in terms of the factor

$$L_i = \frac{\varepsilon_{\text{eff}} + 2\varepsilon_h}{\varepsilon_i + 2\varepsilon_h} \quad (81)$$

that enters Eq. (60), relating the mesoscopic electric field in an inclusion to the macroscopic field in the Maxwell Garnett composite material. Factor L_i has thus the meaning of the local-field correction factor for the inclusions in Maxwell Garnett geometry, and Eqs. (80) are in agreement with the result of the previous paragraph, Eq. (74b).

We emphasize that L_i is not to be confused with the *full* local-field correction containing both the influence of the local environment within

Figure 17



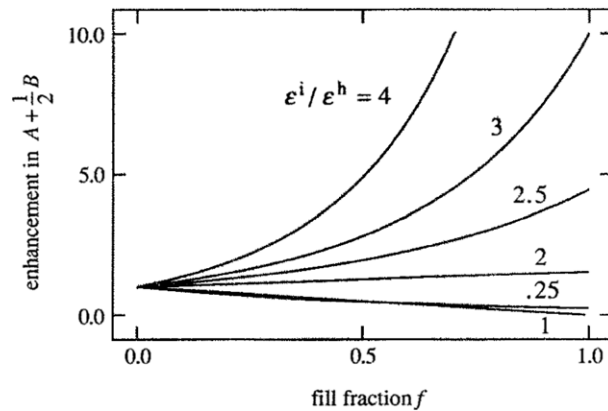
Enhancement in the nonlinear coefficients A_{eff} and B_{eff} as a function of the volume fraction of the nonlinear inclusions embedded in a linear host. Reproduced with permission from Fig. 3, Ref. [30]. Copyright 1992 by the American Physical Society (<http://link.aps.org/doi/10.1103/PhysRevA.46.1614>).

an inclusion and the structural contribution from the composite material. In Subsection 4.2, we took into account both the local environment and structural contributions when treating the local-field-corrected small-signal gain coefficient. We did it there on purpose, to emphasize that there are, in fact, two mechanisms contributing to the local field. In this section, we restrict ourselves to accounting for the difference between the mesoscopic field in a constituent of a composite material and its macroscopic field, thus considering only the effect of composite geometry on the local field.

To analyze the practical importance of Maxwell Garnett composite materials with the nonlinearity in inclusions, we plot the ratios A_{eff}/A_i and B_{eff}/B_i , indicating an enhancement of the nonlinear coefficients, as functions of the inclusion volume fraction for different values of $\varepsilon_i/\varepsilon_h$ [30] (see Fig. 17). The strength of the nonlinear interactions, characterized by the coefficients A_{eff} and B_{eff} , increases with the inclusion volume fraction at a rate that is either more or less rapid than linear, depending on the ratio of the dielectric permittivities of the inclusion and host materials $\varepsilon_i/\varepsilon_h$. The reason for this behavior is the concentration of the electric field in the component with the lower optical density. When $\varepsilon_i < \varepsilon_h$, the field is concentrated in the nonlinear inclusion, and the strength of the nonlinear interactions in this case is enhanced compared with that in the case when $\varepsilon_i > \varepsilon_h$. However, it is clear from Fig. 17 that the effective nonlinear coefficients can never be larger than those of the pure inclusion material.

A different situation arises when the host is nonlinear and the inclusions are linear. Due to the geometry of the Maxwell Garnett composite materials, the electric field in the host is nonuniform, especially in the regions around the inclusions, where it can be very large. Because of the complexity of the electric field distribution, the expressions for the effective nonlinear coefficients in this case are very complicated. We thus

Figure 18



Enhancement in the nonlinear coefficient of the Maxwell Garnett composite material with a nonlinear host as a function of the volume fraction of the linear inclusions. Reproduced with permission from Fig. 4, Ref. [30]. Copyright 1992 by the American Physical Society (<http://link.aps.org/doi/10.1103/PhysRevA.46.1614>).

do not present them here, referring the reader to the original paper [30] for these expressions.

In Fig. 18, we show the enhancement of the effective nonlinear coefficients of a Maxwell Garnett material with a nonlinear host and linear inclusions, compared with the nonlinear coefficients of the homogeneous host material, as a function of the inclusion volume fraction at different values of the ratio ϵ_i/ϵ_h . Because of the large concentration of the electric field in the vicinity of inclusions, it is possible to achieve an enhancement of the effective nonlinearity compared with that of the pure host material for the case when $\epsilon_i > \epsilon_h$. It is remarkable that such an enhancement is achievable by an addition of small amount of *linear* material to a nonlinear host.

Among the theories describing the nonlinear interactions in Maxwell Garnett composite materials, we would also like to mention the work by Gao *et al.* [83]. They developed a nonlinear differential effective dipole approximation (NDEDA) to investigate an effective linear and a third-order nonlinear susceptibility in a Maxwell Garnett composite material with graded spherical inclusions dispersed in a linear host material. For such inclusions, the linear and nonlinear optical properties vary along the radius. The authors of [83] imitated the graded profile by using a multishell construction. Taking into account local-field effects, they derived expressions for the effective linear dielectric constant and nonlinear susceptibility of such a composite material. They applied their theory to investigate the surface plasmon resonant effect on the optical absorption and optical nonlinearity enhancement.

A theoretical study of second-harmonic generation in a dilute suspension of coated nanoparticles has been presented by Hui *et al.* [84]. The authors consider a dilute suspension of coated spheres under the assumption that only the coating material has a nonzero second-order susceptibility describing the second-harmonic generation, while the host

and core materials are linear. They found that even with a modest choice of material parameters a significant enhancement of second-order nonlinear susceptibility can be obtained at certain frequencies.

An alternative theoretical model of the nonlinear optical response of Maxwell Garnett composite geometry was developed by Stockman *et al.* [85]. Their theory is based on material-independent spectral representation in the dipole approximation. They show that a strong enhancement (up to four orders of magnitude) of the third-order nonlinear susceptibility is possible in case of silver nanocomposite. They point out that the previous theories, developed under the assumption that the electric field in each inclusion is equivalent, are applicable only in cases when the volume fraction of the inclusions is very low ($f_i \sim 10^{-3}$), because of strong fluctuations of the local field in the resonant regions.

Recent theoretical studies include those on supercontinuum generation in silica glass doped with silver nanoparticles [86] and on aqueous colloids containing silver nanoparticles by Driben *et al.* [87]. Later, Driben and Herrmann also predicted that it is possible to achieve solitary wave propagation over five soliton periods in silica glass containing silver nanoparticles [88] despite the high plasmonic loss. The same group studied the effective linear and nonlinear optical properties of Maxwell Garnett composite materials comprising silver nanoparticles of various shapes and sizes dispersed in a linear host [89]. Another recent theoretical work [90] is devoted to the study of the linear and nonlinear optical properties of a dense array of metal nanoparticles as functions of interparticle separation. In all of these situations, a combined effect of surface plasmon resonance and strong field localization are responsible for the largely enhanced nonlinear interactions.

5.2b. Layered Composite Geometry

In [32], Boyd and Sipe theoretically describe some nonlinear optical effects, such as second-harmonic generation, electro-optic effect, and the nonlinear index of refraction, in the layered composite geometry. Similarly to the linear optical properties, the nonlinear optical susceptibilities are affected by the local-field effects much more strongly when the electric field and polarization components are perpendicular to the layers. As we have already shown in Subsection 4.2, a significant enhancement of the small-signal gain coefficient is achievable in this case. As has been shown in [32], an even larger enhancement is possible in the nonlinear optical regime.

Assuming that a layered composite material possesses a second-order nonlinearity in both components a and b , given by $\chi_a^{(2)} = \chi_a^{(2)}(2\omega = \omega + \omega)$ and $\chi_b^{(2)} = \chi_b^{(2)}(2\omega = \omega + \omega)$, and considering only the components of the electric field, polarization, and susceptibility tensor that are perpendicular to the layers, one can arrive at the expression

$$\begin{aligned} \chi_{\text{eff}}^{(2)}(2\omega = \omega + \omega) = & f_a \frac{[\varepsilon_{\text{eff}}(\omega)]^2 \varepsilon_{\text{eff}}(2\omega)}{[\varepsilon_a(\omega)]^2 \varepsilon_a(2\omega)} \chi_a^{(2)} \\ & + f_b \frac{[\varepsilon_{\text{eff}}(\omega)]^2 \varepsilon_{\text{eff}}(2\omega)}{[\varepsilon_b(\omega)]^2 \varepsilon_b(2\omega)} \chi_b^{(2)} \end{aligned} \quad (82)$$

for the effective second-order susceptibility of the layered composite material. Recall from Eq. (58) for the mesoscopic electric field in layers a the local-field correction factor

$$L_a = \frac{\varepsilon_{\text{eff}}}{\varepsilon_a}. \quad (83)$$

Similarly, $L_b = \varepsilon_{\text{eff}}/\varepsilon_b$ for layers b . One thus can rewrite Eq. (82) as

$$\chi_{\text{eff}}^{(2)}(2\omega = \omega + \omega) = f_a [L_a(\omega)]^2 L_a(2\omega) \chi_a^{(2)} + f_b [L_b(\omega)]^2 L_b(2\omega) \chi_b^{(2)}. \quad (84)$$

This result is in agreement with Eq. (74b): if n is the order of the lowest-order nonlinearity in the medium, then the effective susceptibility associated with this nonlinearity scales as the $n + 1$ power of the local-field correction factor.

A similar result can be obtained for the Kerr nonlinearity, if one assumes that both the components of the layered composite materials are centrosymmetric (lack even-order nonlinear interactions):

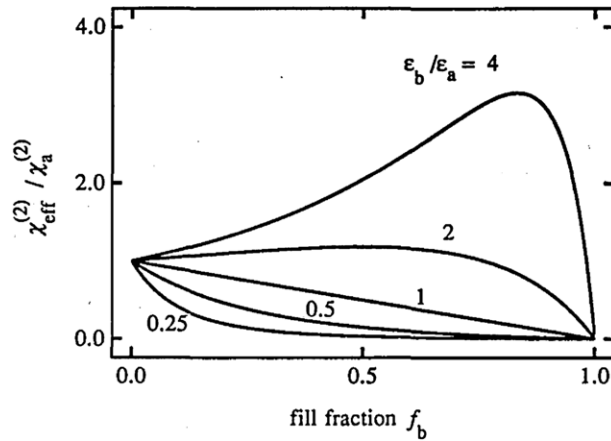
$$\chi_{\text{eff}}^{(3)}(\omega = \omega + \omega - \omega) = f_a |L_a|^2 L_a^2 \chi_a^{(3)} + f_b |L_b|^2 L_b^2 \chi_b^{(3)}. \quad (85)$$

Here $\chi_a^{(3)} = \chi_a^{(3)}(\omega = \omega + \omega - \omega)$ and $\chi_b^{(3)} = \chi_b^{(3)}(\omega = \omega + \omega - \omega)$ are the third-order nonlinear susceptibilities, describing the nonlinear refractive index (Kerr effect) in bulk materials a and b .

In Fig. 19, we show the enhancement of the second-order nonlinear susceptibility for the second-harmonic generation process in a layered composite material as a function of f_a under the assumption that only the constituent a responds nonlinearly to the external optical field for different ratios $\varepsilon_b/\varepsilon_a$. Clearly, a significant enhancement is achievable for the cases when the dielectric constant of the linear component is larger, so that the electric field is concentrated in the nonlinear component. The same type of behavior can be observed in Fig. 20, where we show the third-order effective nonlinear susceptibility for the Kerr effect, assuming once again that only component a exhibits a nonlinear optical response. The enhancement in this case is even more significant, as the effective susceptibility scales as the fourth power of the local-field correction factor [see Eq. (85)].

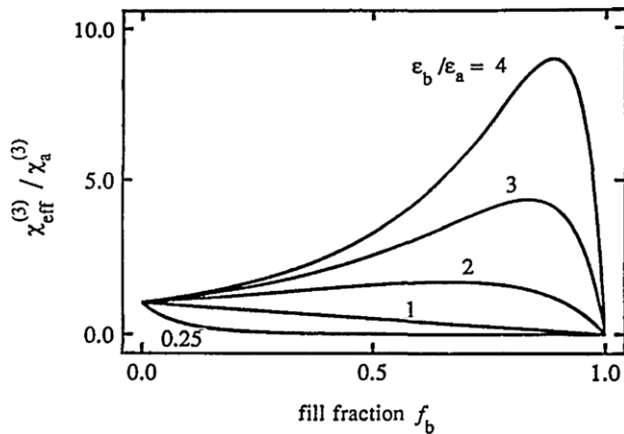
Other theoretical studies of layered composite geometry include investigation of the effective linear and third-order nonlinear susceptibilities of graded metal films [91]. The authors of [91] found that in graded films the surface plasmon resonances are significantly broader, which makes such layered composite materials more suitable for the nonlinear optical applications. As it is easier in practice to fabricate multilayer metallic films than graded films, the same authors later investigated the enhancement of the nonlinear optical response in a multilayer metal composite material [92]. They have shown that there is a gradual transition from sharp resonant peaks to continuous bands with an increase in the number of layers (See Fig. 21). For a sufficiently large number of layers, the surface plasmon resonances become indistinguishable from those of a graded composite material. As a result, a large enhancement of the third-order nonlinear susceptibility is achievable in these more easily realizable structures.

Figure 19



Enhancement in the nonlinear susceptibility describing second-harmonic generation in a layered composite material as a function of the volume fraction of component b under the assumption that only component a possesses the nonlinear optical response. Reproduced from Fig. 4, Ref. [32] (<http://dx.doi.org/10.1364/JOSAB.11.000297>).

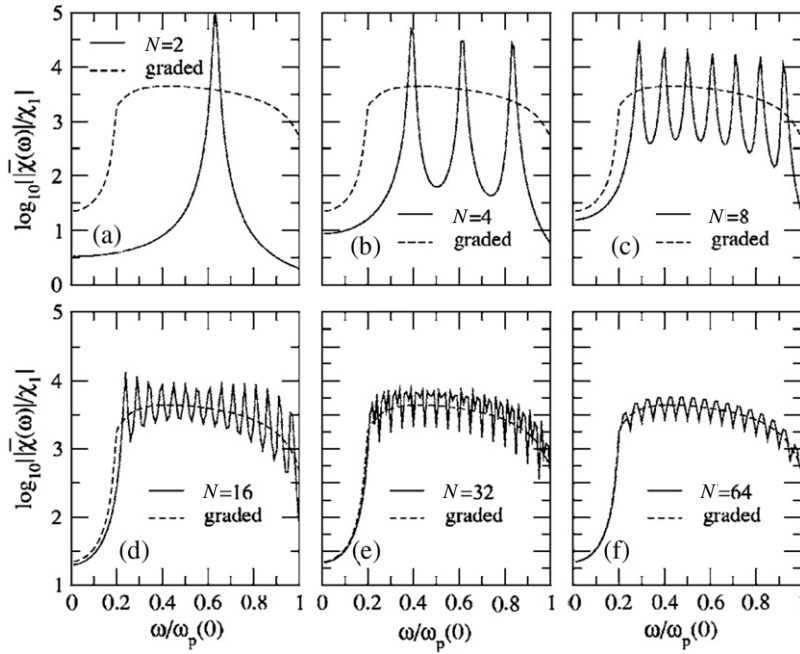
Figure 20



Enhancement in the nonlinear susceptibility describing the nonlinear refractive index in a layered composite material as a function of the volume fraction of component b under the assumption that only component a possesses the nonlinear optical response. Reproduced from Fig. 6, Ref. [32] (<http://dx.doi.org/10.1364/JOSAB.11.000297>).

In [93,94], Zheltikov derived and analyzed mixing rules in layered and Maxwell Garnett composite geometries. He showed that it is possible to manage group-velocity dispersion in nanocomposite materials to achieve phase-matched nonlinear interactions by manipulating the volume fraction, the size of the nanograins, and their dielectric properties. This result is especially important for nonlinear interactions with femtosecond laser pulses, as the group-velocity dispersion becomes

Figure 21



Enhancement of the third-order nonlinear susceptibility in a multilayer metal composite material as a function of the normalized incident angular frequency for different numbers of periods, as marked on the graph (solid curves). Dashed curves, $\chi^{(3)}$ enhancement for graded metal films. Reproduced with permission from Fig. 2, Ref. [92]. Copyright 2006, American Institute of Physics (<http://link.aip.org/link/doi/10.1063/1.2175477>).

especially significant and can lead to a large phase mismatch between the interacting waves.

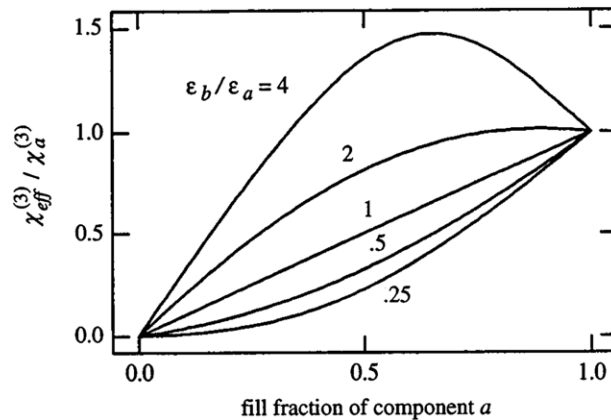
5.2c. Bruggeman Composite Geometry

The nonlinear optical response of the Bruggeman composite geometry, which is a random mixture of two or more constituents, has been theoretically investigated by Zeng *et al.* [42]. The resulting expression for the effective third-order susceptibility characterizing the Kerr effect is given by

$$\chi_{\text{eff}}^{(3)} = \frac{1}{f_a} \left| \frac{\partial \varepsilon_{\text{eff}}}{\partial \varepsilon_a} \right| \left(\frac{\partial \varepsilon_{\text{eff}}}{\partial \varepsilon_a} \right) \chi_a^{(3)}, \quad (86)$$

where the effective dielectric permittivity is given by Eq. (16). The corresponding enhancement in the effective third-order susceptibility under the assumption that the nonlinearity is present only in component a is shown as a function of f_a in Fig. 22. The Bruggeman composite geometry better describes randomly intermixed dielectric constituents with volume fractions significantly larger than the fraction of inclusions in the Maxwell Garnett geometry. When the volume fractions of the two constituents become comparable, the electric field localization becomes less pronounced, and the enhancement of the effective nonlinear

Figure 22



Enhancement of the third-order nonlinear susceptibility in a Bruggeman composite material as a function of the volume fraction of the nonlinear component a . Reproduced from Fig. 2, Ref. [37] (<http://dx.doi.org/10.1364/JOSAB.14.002310>).

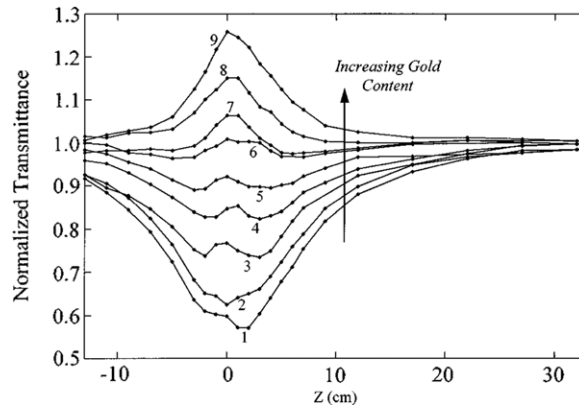
susceptibility decreases. This could be the reason for the smaller enhancement of the nonlinear susceptibility predicted by the Bruggeman model compared with that given by the Maxwell Garnett model for the case of a nonlinear host material (see Fig. 18).

When the volume fraction of one of the constituents reaches $\sim 30\%$, percolation can occur. In this regime, the nature of the optical properties of the material changes dramatically. Unlike Maxwell Garnett theory, the Bruggeman model can accurately describe this regime [45]. On the other hand, the Bruggeman model cannot be applied to metal–dielectric composite materials, as it does not account for surface plasmon resonances.

A theoretical study of third-harmonic generation in a random composite material is also reported by Hui *et al.* [95]. They consider the combined contributions of the direct third-order and cascaded second-order susceptibilities and present a full tensor treatment of the resulting effective third-order susceptibility associated with third-harmonic generation. The use of the Bruggeman theory allowed them to study both local-field effects and percolation in a system of randomly intermixed linear and weakly nonlinear constituents.

In [96], Saarinen *et al.* study a degenerate third-order nonlinear susceptibility enhancement in Maxwell Garnett and Bruggeman composite geometries based on a nonlinear host and high-index linear spherical inclusions. To add practical value to their studies, they choose highly nonlinear polymers, such as polythiophene (PT10) and polysilane (PDHS), as the host materials. The nanoparticles are assumed to be TiO_2 spheres that have a negligible third-order nonlinearity compared with that of the polymers. The authors of [96] treat systems with smaller nanoparticle volume fractions as a Maxwell Garnett composite geometry while using Bruggeman effective-medium theory to describe larger volume fractions. They demonstrate that up to twofold enhancement of the third-order nonlinear susceptibility is achievable in the Maxwell

Figure 23



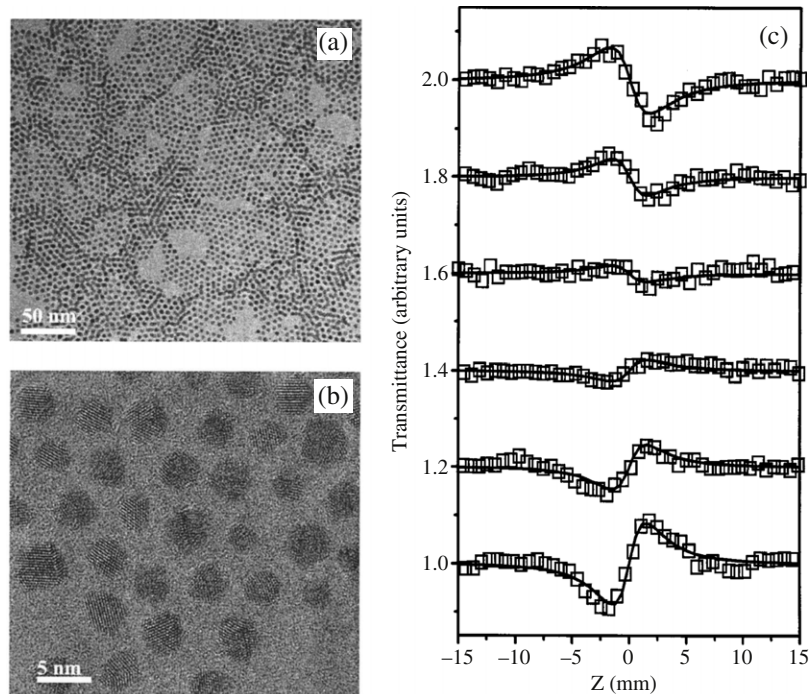
Nonlinear absorption in a gold nanoparticle colloid mixed with a solvent containing the nonlinear organic molecules. Different curves correspond to different volume fractions of the gold nanoparticles. Reproduced from Fig. 4, Ref. [35] (<http://dx.doi.org/10.1364/JOSAB.14.001625>).

Garnett regime of lower volume fraction. The Bruggeman model resulted in a peak enhancement of 1.5 at a nanoparticle volume fraction $f_i = 0.3$. The material system studied in [96] can be easily produced.

5.3. Experimental Studies

Most of the experiments on measuring the nonlinear optical properties of composite materials involve metal nanoparticles dispersed in dielectric hosts. It is possible to observe a dramatic enhancement of the nonlinear optical response in such composite materials that is due to a strong electric field localization combined with surface plasmon resonances. In [35], Smith *et al.* report the cancellation of photoinduced absorption by addition of small amount of gold nanoparticles to a nonlinear host material. Gold colloids were diluted to achieve different volume fractions of the gold nanoparticles and were added to a solvent containing nonlinear organic molecules. Even though the nonlinear absorption was positive for both the pure solvent and the gold colloids, a range of positive and negative absorption coefficients could be obtained by varying the gold content (see Fig. 23). At the surface plasmon resonance, the local-field correction factor becomes nearly imaginary for a host without significant linear absorption: $L \approx 3\varepsilon_h'/i\varepsilon_i''$. (Here prime and double prime indicate the real and imaginary parts of the susceptibilities, respectively.) Under these conditions, $L^2 < 0$ at some volume fractions, and the sign reversal in $\chi_{\text{eff}}^{(3)}$ of the composite material becomes possible.

Later Piredda *et al.* demonstrated a sign reversal of the nonlinear absorption coefficient in a gold-silica composite with gold volume fractions as high as 0.55 [97]. They found that the composite material acts as a saturable absorber at all gold volume fractions, even though gold itself is an optical limiter. They concluded that the nature of the local-field enhancement for higher volume fractions of the nanoparticles is the same as for the lower volume fractions [35].



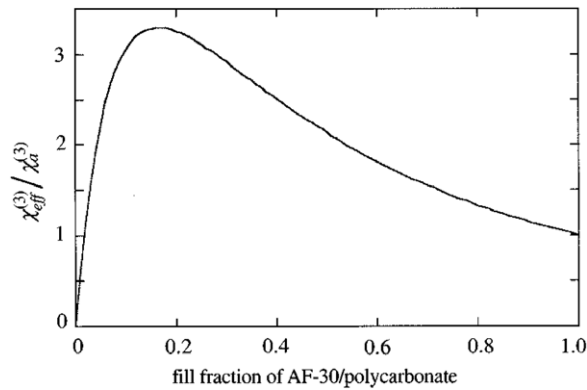
(a), (b) Transmission electron microscopy images of silver nanoparticles. (c) Closed-aperture Z-scan traces of suspensions of silver nanoparticles in CS_2 . Different curves correspond to different volume fractions of the nanoparticles, ranging between 0 and 4.0×10^{-5} , bottom to top. Reproduced from Figs. 1 and 3, Ref. [98] (<http://dx.doi.org/10.1364/JOSAB.22.002444>).

Cancellation of photoinduced absorption α_2 and sign reversal of the nonlinear refractive index n_2 have been observed in [98] in suspension of silver nanoparticles in carbon disulfide CS_2 (see Fig. 24). Due to the high nonlinearity of CS_2 , the local-field enhancement factor contained a real part along with an imaginary part. As a result, the cancellation of α_2 and sign reversal of n_2 were due to counteraction of the nonlinearities of CS_2 and silver. Nevertheless, the local-field enhancement was significant in this case, and the generalized Maxwell Garnett model [30] was applied for theoretical description of the experimental measurements.

Ultrafast low-power all-optical switching has been experimentally realized in a photonic crystal based on a nanocomposite material consisting of silver nanoparticles in a π -conjugated polymer [99]. Enhanced ultrafast optical nonlinearity has been studied in anodized aluminum oxide nanostructures as a function of the pore number density and pore diameters [100]. A strong enhancement of the third-order susceptibility has been observed in an array of rectangular gold nanoparticles and attributed to a strong electric field localization [101]. Various reports on enhancement of the third-order nonlinearity in metal nanoparticle composites due to strong electric field localization have been presented [102–105].

Layered composite materials are relatively easy to fabricate. As an example, a simple spin-coating procedure can be used for this purpose.

Figure 25



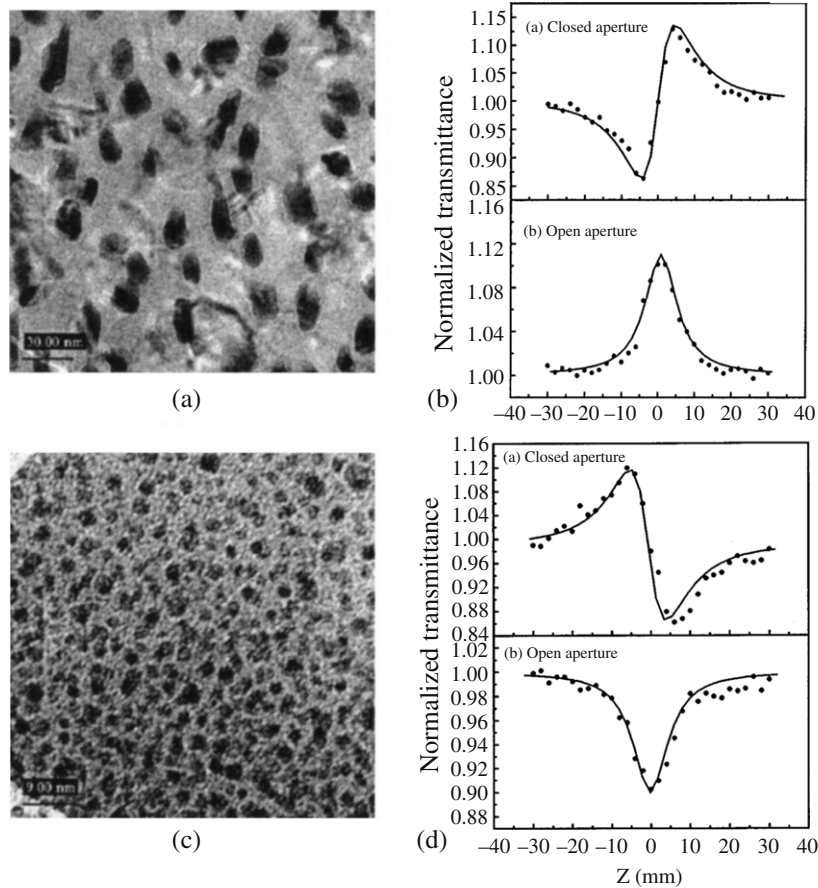
Enhancement in the third-order susceptibility describing the nonlinear refractive index in a layered composite material as a function of the volume fraction of component b under the assumption that only component a exhibits a nonlinear optical response. Reproduced with permissions from Fig. 1, Ref. [36]. Copyright 1999 by the American Institute of Physics (<http://link.aip.org/link/doi/10.1063/1.123866>).

This technique was utilized by Fischer *et al.* in [34] to produce a layered composite material comprising the conjugated polymer PBZT and titanium dioxide. The nonlinear optical response of TiO_2 is negligible compared with that of the polymer, while its refractive index is significantly higher. As a result, a 35% enhancement of the nonlinearity in the composite material was observed compared with that of the pure polymer.

An even larger enhancement, up to 3.2 times, was reported in the electro-optic response of a layered composite material by Nelson and Boyd in Ref. [36]. The composite material comprised alternating layers of barium titanite and polycarbonate containing a third-order nonlinear optical organic dopant. The corresponding effective third-order nonlinear susceptibility enhancement as a function of the polycarbonate is shown in Fig. 25.

A sign reversal in both the nonlinear refractive index n_2 and two-photon absorption coefficient α_2 has been demonstrated in layered composite materials based on gold nanoparticles embedded in BaTiO_3 matrices [106] (see Fig. 26). Two films with equal gold volume fractions but different nanoparticle sizes and shapes exhibited a simultaneous sign change in real and imaginary parts of the third-order nonlinear susceptibility.

In [37], Gehr *et al.* report measurements of the effective linear and nonlinear refractive indices of a porous-glass-based Bruggeman composite material. The porous glass matrix is a silica structure with pore dimensions of approximately 4–6 Å. It is a typical example of Bruggeman composite geometry because of the relatively large (~28%) void volume fraction and because of the arbitrary shape of the voids. The matrix was filled with different fluids with refractive indices ranging between 1.32 and 1.78. The nonlinear refractive index was measured

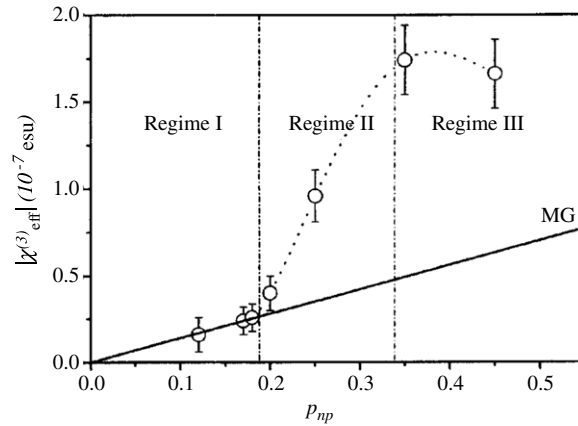


(a), (c) Transmission electron microscopy images of Au in BaTiO₃ films with the nanoparticle sizes 15–20 nm and 2–3 nm, respectively. (b), (d) Closed- (top) and open-aperture (bottom) Z-scan traces of the samples shown in (a) and (c), respectively. Reproduced with permission from Figs. 1, 4, and 5, Ref. [106]. Copyright 2003 by the American Institute of Physics (<http://link.aip.org/link/doi/10.1063/1.1625082>).

by using the closed-aperture Z-scan technique [107]. Good agreement between the measurements and Bruggeman theory was achieved.

In [108], Coso *et al.* studied the third-order nonlinear susceptibility of a composite material consisting of Cu nanoparticles in an amorphous Al₂O₃ matrix at Cu volume fractions f_{Cu} in the range between 0.07 and 0.45. The Maxwell Garnett model has been shown to describe the experimental data in the regime of the linear growth of $\chi_{\text{eff}}^{(3)}$ at $0.07 \leq f_{\text{Cu}} \leq 0.2$ (Fig. 27, Regime I). In the range of volume fractions $0.2 \leq f_{\text{Cu}} \leq 0.35$, $\chi_{\text{eff}}^{(3)}$ undergoes a sharp increase (see Fig. 27, Regime II). The failure of the Maxwell Garnett model in that range can be attributed to the fact that the inclusions start interacting with each other, which gives rise to a strongly inhomogeneous electric field. The Bruggeman model [Eq. (86)], however, fails in that range as well, as it is not capable of describing the resonant behavior of the susceptibility in the vicinity of the surface plasmon resonance. A giant enhancement, up to a factor of

Figure 27



Absolute value of the effective third-order nonlinear susceptibility of a composite material containing Cu nanoparticles embedded in amorphous Al_2O_3 . Three regimes of $\chi_{\text{eff}}^{(3)}$ behavior are observable in the graph, as marked. Reproduced with permissions from Fig. 4, Ref. [108]. Copyright 2004 by the American Institute of Physics (<http://link.aip.org/link/doi/10.1063/1.1643779>).

10, has been observed at that range of the volume fractions, while the predicted enhancement of the effective third-order susceptibility, given by the Bruggeman model, is only a factor of 2. Saturation behavior is observed at $f_{\text{Cu}} > 0.35$ owing to a decrease of the local-field enhancement in that range of volume fractions (Regime III in Fig. 27).

6. Cascaded Nonlinearity Induced by Local-Field Effects

Local-field effects can give rise to new physical phenomena. For instance, steady-state solutions to the local-field-corrected Maxwell–Bloch equations indicate that it is possible to realize mirrorless optical bistability [77,109–111]. Also, an additional inversion-dependent frequency shift appears. In the case of homogeneous media, it is the well-known Lorentz redshift [see Eq. (47)]. It has been experimentally measured in the reflection spectrum of a dense alkali vapor [78,112]. The Lorentz redshift can cause a pulse to acquire a dynamic chirp, which enables solitons to form at a very low level of atomic excitation [113,114]. In a collection of three-level atoms, local-field effects can lead to inversionless gain and the enhancement of the absorptionless refractive index by more than two orders of magnitude [115–118]. Successful experimental attempts to realize this enhancement of the refractive index have been reported [119,120].

A phenomenological approach to treating local-field effects in nonlinear optics was proposed by Bloembergen [82]. He found that the local-field-corrected second-order nonlinear susceptibility scales as three powers of the local-field correction factor L . It has been widely understood that Bloembergen’s result can be generalized to a higher-order nonlinearity, and that the corresponding n th-order nonlinear susceptibility should

scale as L^{n+1} (see, for example, [81,121]). We have recently theoretically shown [79] that Bloembergen's approach, when consistently applied, actually leads to a much more complicated form for the nonlinear susceptibility. This is due to the presence of a cascaded nonlinear effect.

Cascading is a process in which a lower-order nonlinear susceptibility contributes to higher-order nonlinear effects in a multistep fashion; it has been a field of interest in nonlinear optics for some time. Macroscopic cascading has a nonlocal nature, in that the intermediate field generated by a lower-order nonlinearity propagates to contribute to a higher-order nonlinear process by nonlinearly interacting with the fundamental field [122–131]. Thus, it has been acknowledged that the experimentally measured third-order susceptibility can include contributions proportional to the square of the second-order susceptibility [122–124]. On the other hand, it has also been shown that nonlinear cascading is possible because of the local nature of the field acting on individual molecules in the medium [124,132–137]. This local-field-induced “microscopic” cascading does not require propagation and has a purely local character.

The fact that local-field effects create cascaded contributions of the lowest order hyperpolarizability $\gamma_{\text{at}}^{(2)}$ to the third-order susceptibility was first demonstrated by Bedeaux and Bloembergen [132]. They presented a general relationship between the macroscopic and microscopic nonlinear dielectric response, obtained by neglecting pair correlation effects that were later taken into account by Andrews *et al.* [136]. All the studies conducted thus far have concentrated on treating the local cascading contribution of $\gamma_{\text{at}}^{(2)}$ to third-order nonlinear effects, which arises only if the constituent molecules lack a center of inversion symmetry. We have recently shown both theoretically [79] and experimentally [138] that microscopic cascading effects can be significant in higher-order nonlinearities and are present in any system with a nonlinear response higher than lowest level.

In Subsection 6.1, we give a simplified theoretical description of how local-field effects can induce microscopic cascading phenomenon in high-order nonlinearities. We show how to properly apply Bloembergen's approach to treat local-field effects in higher-order nonlinearities. It becomes obvious that local-field effects can, indeed, give rise to a microscopic cascading contribution of the lower-order hyperpolarizabilities to higher-order nonlinear susceptibilities. In Subsection 6.2, we review our experimental work on separating the influence of microscopic cascading from the more-well-known macroscopic cascading, and we show conditions under which microscopic cascading is the dominant effect [138].

6.1. Theoretical Prediction of Microscopic Cascading

The straightforward generalization [81,121] of the Bloembergen's result to the case of the saturation effects [which are described by an odd-order nonlinearity as $\chi^{(n)} = \chi^{(n)}(\omega = \omega + \omega - \omega + \dots)$] reads as

$$\chi^{(n)} = N\gamma_{\text{at}}^{(n)}|L|^{n-1}L^2, \quad (87)$$

where $\gamma_{\text{at}}^{(n)}$ is the n th-order microscopic hyperpolarizability ($n \neq 1$).

We have shown, however, using Lorentz–Maxwell–Bloch equations and accounting for the nonlinear optical interactions treated up to a fifth order, that [79]

$$\chi^{(1)} = N\gamma_{\text{at}}^{(1)}L, \quad (88a)$$

$$\chi^{(3)} = N\gamma_{\text{at}}^{(3)}|L|^2L^2, \quad (88b)$$

but

$$\chi^{(5)} \neq N\gamma_{\text{at}}^{(5)}|L|^4L^2. \quad (88c)$$

Thus, the naïve local-field correction in terms of L 's, Eq. (87), is in disagreement with the correct result derived from the Maxwell–Bloch equations.

To find the origin of this disagreement, we have addressed the problem of treating the saturation up to the fifth order of nonlinearity [79] by following the recipe suggested by Bloembergen [82], rather than using the straightforward generalization given by Eq. (87). The approach can be summarized as follows.

We consider the case of a homogeneous centrosymmetric medium with the nonlinear optical interactions up to the fifth order, assuming that the local field in the medium can be described by the Lorentz model. Extending the treatment that we used in Subsection 5.1 to include the fifth-order nonlinear interactions, we can write the total polarization as

$$P = P^{(1)} + P^{(3)} + P^{(5)} + \dots, \quad (89)$$

where

$$P^{(1)} = N\gamma_{\text{at}}^{(1)}E_{\text{loc}}, \quad (90a)$$

$$P^{(3)} = N\gamma_{\text{at}}^{(3)}|E_{\text{loc}}|^2E_{\text{loc}}, \quad (90b)$$

and

$$P^{(5)} = N\gamma_{\text{at}}^{(5)}|E_{\text{loc}}|^4E_{\text{loc}}. \quad (90c)$$

Using Eq. (63) in Eq. (90a), we obtain

$$P^{(1)} = \frac{\varepsilon^{(1)} - 1}{4\pi} \left[E + \frac{4\pi}{3}P^{(3)} + \frac{4\pi}{3}P^{(5)} + \dots \right]. \quad (91)$$

The electric displacement vector D is defined as

$$D = E + 4\pi P = E + 4\pi P^{(1)} + 4\pi P^{(3)} + 4\pi P^{(5)} + \dots. \quad (92)$$

Substituting Eq. (91) into Eq. (92), we find that

$$D = \varepsilon^{(1)}E + 4\pi P^{\text{NLS}}, \quad (93)$$

where

$$P^{\text{NLS}} = L(P^{(3)} + P^{(5)} + \dots). \quad (94)$$

Substituting expression (91) for the polarization $P^{(1)}$ into Eq. (89) for the total polarization, we find that

$$P = \chi^{(1)}E + P^{\text{NLS}}. \quad (95)$$

Substituting Eq. (63) for the local field into Eqs. (90b) and (90c) for the polarizations $P^{(3)}$ and $P^{(5)}$ and dropping out the terms scaling with higher than the fifth power of the electric field, we obtain

$$P^{(3)} = 3N\gamma_{\text{at}}^{(3)}|L|^2L|E|^2E + \left[24\pi N^2(\gamma_{\text{at}}^{(3)})^2|L|^4L^2 + 12\pi N^2|\gamma_{\text{at}}^{(3)}|^2|L|^6\right]|E|^4E \quad (96a)$$

and

$$P^{(5)} = 10N\gamma_{\text{at}}^{(5)}|L|^4L|E|^4E. \quad (96b)$$

Note that $P^{(3)}$ contains terms proportional to the fifth power of the electric field. Substituting Eq. (96) into Eq. (94), and Eq. (94) into Eq. (95), we find the total polarization to be

$$P = \chi^{(1)}E + 3N\gamma_{\text{at}}^{(3)}|L|^2L^2|E|^2E + [24\pi N^2(\gamma_{\text{at}}^{(3)})^2|L|^4L^3 + 12\pi N^2|\gamma_{\text{at}}^{(3)}|^2|L|^6L + 10N\gamma_{\text{at}}^{(5)}|L|^4L^2]|E|^4E + \dots. \quad (97)$$

Alternatively, the total polarization can be represented as a Taylor series expansion with respect to the average electric field as

$$P = \chi E = \chi^{(1)}E + 3\chi^{(3)}|E|^2E + 10\chi^{(5)}|E|^4E + \dots. \quad (98)$$

Equating Eqs. (97) and (98), we obtain

$$\chi^{(1)} = N\gamma_{\text{at}}^{(1)}L, \quad (99a)$$

$$\chi^{(3)} = N\gamma_{\text{at}}^{(3)}|L|^2L^2, \quad (99b)$$

and

$$\chi^{(5)} = N\gamma_{\text{at}}^{(5)}|L|^4L^2 + \frac{24\pi}{10}N^2(\gamma_{\text{at}}^{(3)})^2|L|^4L^3 + \frac{12\pi}{10}N^2|\gamma_{\text{at}}^{(3)}|^2|L|^6L. \quad (99c)$$

Equations (99) for the local-field-corrected first, third, and fifth order susceptibilities are now equivalent to those obtained by using the Maxwell–Bloch approach [79]. Thus, two different approaches – the Lorentz–Maxwell–Bloch equations and Bloembergen’s approach – brought us to the same result for the local-field-corrected susceptibilities. This is of course not surprising, since both approaches are just different ways of implementing Bloembergen’s scheme.

The expressions for the local-field-corrected $\chi^{(1)}$ and $\chi^{(3)}$ do not display any peculiarity, while Eq. (99c) for $\chi^{(5)}$ deserves special attention. The first term on the right-hand side of the equation is due to a direct contribution from the fifth-order microscopic hyperpolarizability, while the two extra terms come from the contribution of the

third-order microscopic hyperpolarizability. These extra contributions are a manifestation of local-field effects. We denote for convenience the direct contribution to the fifth-order susceptibility as

$$\chi_{\text{dir}}^{(5)} = N\gamma_{\text{at}}^{(5)}|L|^4L^2. \quad (100)$$

Similarly, the sum of the second and third terms on the left-hand side of Eq. (99c) (the microscopic cascaded contribution to $\chi^{(5)}$) can be denoted

$$\chi_{\text{micro}}^{(5)} = \frac{12\pi}{10}N^2[2(\gamma_{\text{at}}^{(3)})^2|L|^4L^3 + |\gamma_{\text{at}}^{(3)}|^2|L|^6L]. \quad (101)$$

Then the total local-field-corrected $\chi^{(5)}$, which is the sum of the two contributions, can be written as

$$\chi^{(5)} = \chi_{\text{dir}}^{(5)} + \chi_{\text{micro}}^{(5)}. \quad (102)$$

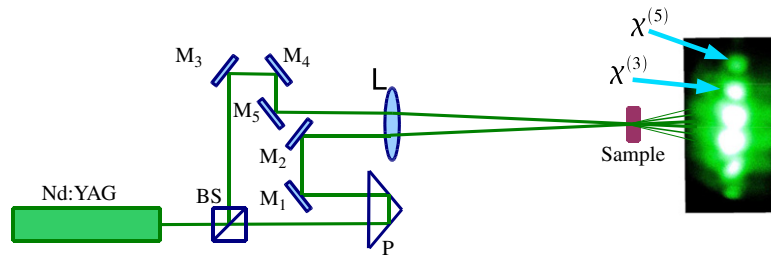
As we pointed out above, the result obtained for $\chi^{(5)}$ does not agree with that predicted by a straightforward generalization of the Bloembergen's result given by Eq. (87). It is evident from Eqs. (87) and (99c) that the generalization, Eq. (87), predicts only the direct term (the term proportional to $\gamma_{\text{at}}^{(5)}$) in the expression for the local-field-corrected $\chi^{(5)}$ and does not account for the cascaded contributions coming from the third-order microscopic hyperpolarizability. We have shown in this section that the cascaded terms arise from substituting the *nonlinear* local field into expression (90b) for $P^{(3)}$. If we were limiting ourselves to considering the third-order nonlinearity (*i.e.*, the lowest-order nonlinearity in our system), as we did in Subsection 5.1, we would have obtained $P^{(3)}$ in the form of Eq. (71) instead of $P^{(3)}$ in the form of Eq. (96a). Thus, one clearly cannot simply use the generalization, Eq. (87), to treat nonlinearity of the order higher than the lowest order of the nonlinearity present in the system of interest.

6.2. Experimental Evidence of Microscopic Cascading

In the previous section, we have shown how local-field effects can act as a mechanism that leads to a cascaded microscopic nonlinear response [79]. In this section, we describe an experiment on separating the microscopic cascaded contribution to the fifth-order nonlinear susceptibility from the direct contribution. This is, to the best of our knowledge, the first experiment of this kind, and it has been described in [138] only very briefly. That is why, in this review, we present additional important details.

It is clear from Eqs. (100) and (101) that $\chi_{\text{dir}}^{(5)}$ is proportional to the molecular (or atomic) density N , whereas $\chi_{\text{micro}}^{(5)}$ is proportional to N^2 . Hence, in order to experimentally separate the two contributions to the fifth-order susceptibility, one should measure $\chi_{\text{dir}}^{(5)}$ and $\chi_{\text{micro}}^{(5)}$ as functions of the molecular or atomic density. We have performed such a measurement in a mixture of carbon disulfide (CS_2) and fullerene (C_{60}), both of which are highly nonlinear materials.

Figure 28



Experimental setup for DFWM. Nd:YAG, 35-ps, 10-Hz, 532-nm Nd:YAG laser; BS, beam splitter; P, prism (delay arm); M₁–M₅, directing mirrors; L, focusing lens, Sample, 2-mm-long quartz cell containing a mixture of CS₂ and C₆₀. Reproduced with permission from Fig. 1, Ref. [138]. Copyright 2009 by the American Physical Society (<http://link.aps.org/doi/10.1103/PhysRevLett.103.113902>).

Our experimental setup is based on a degenerate four-wave mixing (DFWM) scheme [139] (see Fig. 28) that allows one to separate effects that are due to different orders of nonlinearity. Two beams of equal intensity at 532 nm from a frequency-doubled Nd:YAG laser producing 35 ps pulses were sent into a 2 mm quartz cell containing a mixture of CS₂ and C₆₀, and we observed self-diffraction phenomena (see the photograph in Fig. 28). The first order of diffraction is a consequence of the third-order nonlinear effect, while the second-order diffracted beam results from the fifth-order nonlinearity.

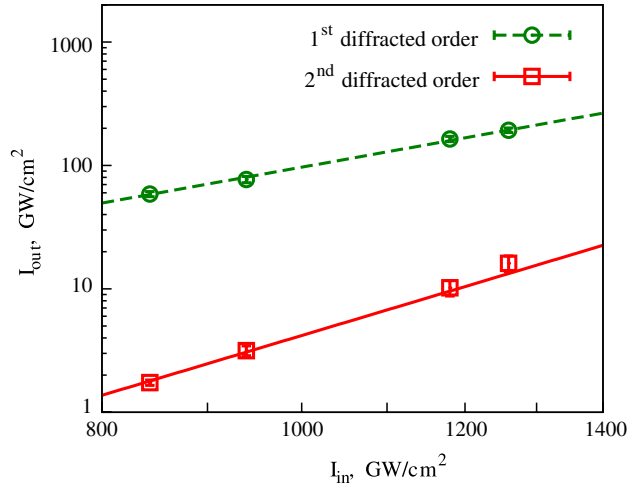
We measured the intensities of the first- and second-order diffracted beams for various concentrations of C₆₀ in CS₂. In order to correct the nonlinear signals for the absorption present in the medium, we measured the linear absorption coefficient α and multiplied our nonlinear signal intensities by the factor $(\alpha l \exp(\alpha l/2)/[1 - \exp(-\alpha l)])^{2n}$, where l is the length of the nonlinear medium and $2n + 1$ is the order of the nonlinearity. We also performed an open-aperture Z-scan measurement [140] to account for the nonlinear absorption in our samples. Extracting the values of the normalized transmission T_{norm} from the Z-scan measurements, we divided our nonlinear intensities by $(T_{\text{norm}})^{2n+1}$. The third- and fifth-order nonlinear signal intensities, corrected for the linear and nonlinear absorptions and plotted on a logarithmic scale as functions of the incident beam intensity, displayed slopes equal to 3 and 5, respectively (see Fig. 29).

The DFWM experiment yields the absolute values of the nonlinear susceptibilities. In order to extract these values from the measured intensities of the diffracted beams, we used the expression [141]

$$I_s = |\chi_{\text{meas}}^{(2n+1)}|^2 I^{2n+1} \left(\frac{n_0 c}{8\pi}\right)^{-2n} \left(\frac{n_0 c}{2\pi \omega l}\right)^{-2} |\Xi(\theta)|^2, \quad (103)$$

relating the measured intensity I_s of the nonlinear signal to the corresponding nonlinear susceptibility $|\chi_{\text{meas}}^{(2n+1)}|$. Here I_1 and I_2 are the intensity of an incident beam, c is the speed of light *in vacuo*, n_0 is the refractive index of the medium, θ is the half-angle between the

Figure 29



Intensities of the first (green circles) and second (red squares) diffracted orders, corresponding to $\chi^{(3)}$ and $\chi^{(5)}$ interactions, respectively, as functions of the incident beam intensity plotted on a logarithmic scale. The lines are the least-squares fits by a cubic (green dashed line) and fifth-order (red solid line) polynomials.

interacting beams in the experiment, and $\Xi(\theta)$ is the phase mismatch term normalized such that $|\Xi(0)| = 1$. $\Xi(\theta)$ takes different forms for different orders of nonlinearities. It is a purely geometrical factor not depending on the molecular density N .

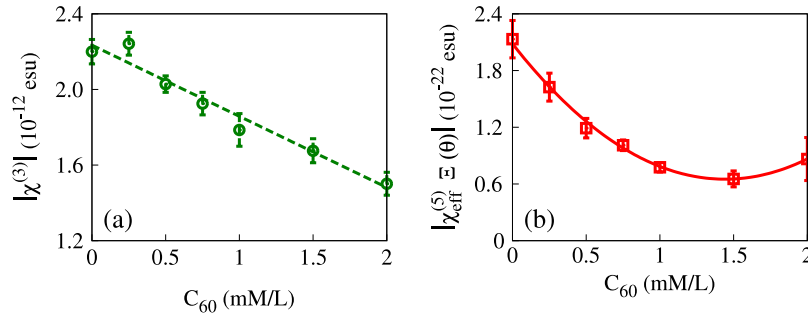
We normalized our measured nonlinear susceptibilities to the known value of $\chi^{(3)}$ for pure CS₂, which is 2.2×10^{-12} esu [81] in order to extract their values from the experimentally measured intensities.

In Fig. 30, we present typical measured $|\chi^{(3)}|$ and $|\chi^{(5)} \Xi(\theta)|$ as functions of the molar concentration $N_{C_{60}}$ of C₆₀. Here and below we do not make an attempt to correct the values of $\chi^{(5)}$ for the phase mismatch, as we cannot precisely determine the value of $\Xi(\theta)$ in our experiment. Possible sources of error include lack of precision in measuring the angle between the interacting beams and imperfections in the geometry of the experiment. We plot the product $|\chi^{(5)} \Xi(\theta)|$, as we can extract its values from our experiment using Eq. (103) with good precision. CS₂ and C₆₀ have nonlinear responses of opposite signs, which is why both the third- and fifth-order nonlinear susceptibilities in Fig. 30 decrease with the increase of $N_{C_{60}}$. It is clear from the graphs that $|\chi^{(3)}|$ depends on $N_{C_{60}}$ linearly, whereas $|\chi^{(5)}|$ has a quadratic dependence due to cascading. However, as we pointed out earlier in this section, the total measured fifth-order susceptibility should also include the macroscopic (propagational) cascaded contribution, that is,

$$|\chi^{(5)}| = |\chi_{LFC}^{(5)} + \chi_{macro}^{(5)}| = |\chi_{dir}^{(5)} + \chi_{micro}^{(5)} + \chi_{macro}^{(5)}|. \quad (104)$$

Both microscopic and macroscopic cascaded effects have a quadratic dependence on the atomic density [132], and thus separating the contributions of the two cascaded effects is not straightforward.

Figure 30



Typical experimental data for (a) third-order and (b) fifth-order nonlinear susceptibilities as functions of $N_{C_{60}}$. The lines represent a least-squares fit with a function (a) linear and (b) quadratic with respect to $N_{C_{60}}$. Reproduced with permission from Fig. 2, Ref. [138]. Copyright 2009 by the American Physical Society (<http://link.aps.org/doi/10.1103/PhysRevLett.103.113902>).

In order to resolve the problem of identification of the microscopic cascaded contribution, we solve the driven wave equation [81],

$$\nabla^2 \tilde{E} - \frac{\varepsilon^{(1)}}{c^2} \frac{\partial^2 \tilde{E}}{\partial t^2} = \frac{4\pi}{c^2} \frac{\partial^2 \tilde{P}^{\text{NL}}}{\partial t^2}, \quad (105)$$

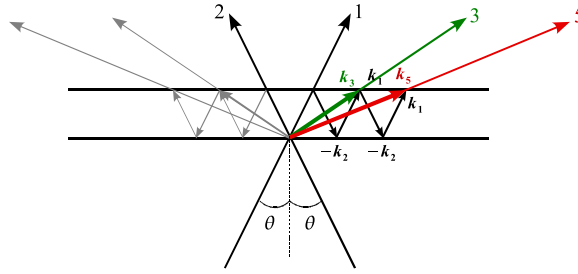
for the direct and microscopic cascaded contributions to $|\chi^{(5)}|$ and, separately, for the macroscopic cascaded contribution. Here $\tilde{P}^{\text{NL}}(t) = P^{\text{NL}} \exp(-i\omega t) = P_0^{\text{NL}} \exp[i(kr - \omega t)]$ denotes the nonlinear polarization. The same kind of relationship is valid for the electric field amplitude: $\tilde{E}(t) = E \exp(-i\omega t) = A \exp[i(kr - \omega t)]$. The total fifth-order nonlinear polarization consists of three contributions, corresponding to the direct and the two cascaded mechanisms:

$$P^{(5)} = P_{\text{dir}}^{(5)} + P_{\text{micro}}^{(5)} + P_{\text{macro}}^{(5)}. \quad (106)$$

Here we dropped the temporal dependence, as we are dealing with a frequency-degenerate nonlinear effect. Next we write the separate contributions to the total $P^{(5)}$ in terms of the electric fields of the interacting waves. After that, we separately substitute them into Eq. (105) and solve it to obtain the corresponding contributions to the electric field amplitude, generated by means of the fifth-order nonlinear process.

In order to illustrate how different contributions to the nonlinear signal are generated, we present a phase matching diagram of our DFWM experiment in Fig. 31. The fundamental electric waves “1” and “2,” propagating at an angle 2θ with respect to each other, interact in the nonlinear medium and produce the diffracted waves “3” and “5.” The direct and microscopic cascaded contributions to $|\chi^{(5)}|$ have the same phase matching condition, as they both are intrinsic properties of the nonlinear response on the molecular or atomic scale. However, it is not possible to achieve full phase matching for these terms, as the nonlinear process is degenerate. That is why it is more informative to present the expression for the wave-vector mismatch for the direct and microscopic

Figure 31



Phase matching diagram for generating the first and second diffracted waves (“3” and “5,” respectively). “1” and “2” are the interacting fundamental waves. \mathbf{k}_i are the k -vectors of the corresponding waves.

cascaded contributions to $|\chi^{(5)}|$, which is

$$\Delta \mathbf{k}_{5,\text{dir}} = \mathbf{k}_5 - (3\mathbf{k}_1 - 2\mathbf{k}_2). \quad (107)$$

Here \mathbf{k}_1 and \mathbf{k}_2 are the wave vectors of the fundamental interacting beams and \mathbf{k}_5 is the wave vector of the generated fifth-order nonlinear signal (see Fig. 31). The corresponding relationship between the nonlinear polarization and the electric fields is

$$P_{\text{dir}}^{(5)} + P_{\text{micro}}^{(5)} = 10(\chi_{\text{dir}}^{(5)} + \chi_{\text{micro}}^{(5)})E_1^2(E_2^*)^2. \quad (108)$$

Solving Eq. (105) for the nonlinear polarization given by Eq. (108), we find the expression

$$A_{\text{dir}}^{(5)} + A_{\text{micro}}^{(5)} = \frac{5\pi}{3n_0^2\theta^2}(\chi_{\text{dir}}^{(5)} + \chi_{\text{micro}}^{(5)})A_1^3(A_2^*)^2 \left[\exp\left(i\frac{12\omega n_0}{c}\theta^2 l\right) - 1 \right] \quad (109)$$

for the amplitudes of the electric field, corresponding to the direct and microscopic contributions to the fifth-order nonlinear signal.

The macroscopic cascaded term, which is a propagational contribution of the generated third-order nonlinear signal to the fifth-order nonlinear signal, results from a two-step process with the corresponding wave-vector mismatches:

$$\Delta \mathbf{k}_3 = \mathbf{k}_3 - (2\mathbf{k}_1 - \mathbf{k}_2); \quad (110a)$$

$$\Delta \mathbf{k}_{5,\text{macro}} = \mathbf{k}_5 - (\mathbf{k}_3 + \mathbf{k}_1 - \mathbf{k}_2). \quad (110b)$$

The nonlinear polarization takes form

$$P_{\text{macro}}^{(5)} = 6\chi^{(3)}E_1E_2^*E_3, \quad (111)$$

where the electric field E_3 , generated through a $\chi^{(3)}$ nonlinear interaction, can be found from Eq. (105):

$$E^{(3)} = \frac{3\pi}{2n_0^2\theta^2}\chi^{(3)}A_1^2A_2^* \left[\exp\left(i\frac{4\omega n_0}{c}\theta^2 l\right) - 1 \right] \exp(ik_3 r). \quad (112)$$

Using Eqs. (110), (111) and (112), we solve Eq. (105) to obtain the relationship

$$A_{\text{macro}}^{(5)} = \frac{35\pi^2}{8n_0^4\theta^4} (\chi^{(3)})^2 A_1^3 (A_2^*)^2 \left\{ \frac{1}{3} \left[\exp\left(i\frac{12\omega n_0}{c}\theta^2 l\right) - 1 \right] - \frac{1}{2} \left[\exp\left(i\frac{8\omega n_0}{c}\theta^2 l\right) - 1 \right] \right\} \quad (113)$$

for the macroscopic cascaded contribution to the fifth-order nonlinear signal.

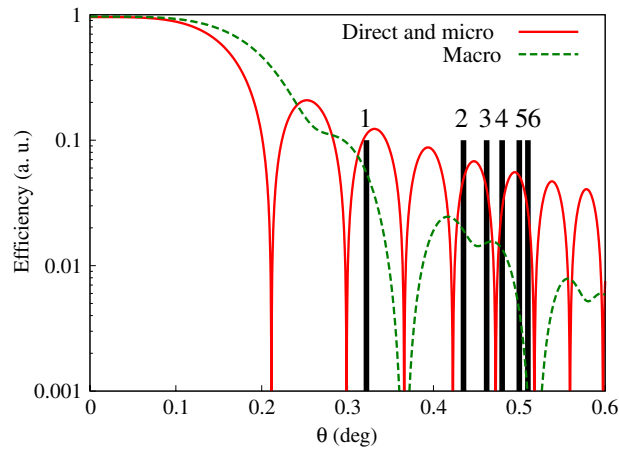
Inspecting Eqs. (109) and (113), one can see that the amplitudes of the electric field of the direct and microscopic cascaded contributions have a different dependence on the angle θ and the cell length l , compared with that of the macroscopic cascaded term. In Fig. 32 we plot the absolute values of the angular dependences of Eqs. (109) and (113), normalized to unity at $\theta = 0$, as functions of the angle θ . These dependences characterize the efficiencies of the direct, microscopic, and macroscopic cascaded contributions to $|\chi^{(5)}|$. The normalized efficiency of the direct and microscopic cascaded contributions is shown as the red solid curve, and the efficiency of the macroscopic cascaded contribution is shown as the green dashed curve. As the efficiencies are normalized, we cannot extract information about the relative values of the contributions to the total measured $|\chi^{(5)}|$. However, the graphs show the approximate positions of the minima and maxima of the efficiencies. It is also important that the efficiency of the macroscopic cascaded process decreases much more rapidly than that of the direct and microscopic cascaded contributions with the increase of the angle between the interacting beams. By measuring the third- and fifth-order nonlinear signals at different angles between the interacting beams, it is possible to discriminate between different contributions to $|\chi^{(5)}|$.

The macroscopic cascaded contribution to the total electric field generated by the fifth-order nonlinear process is proportional to $|\chi^{(3)}|^2$. Hence, in our experiment $|\chi_{\text{macro}}^{(5)}|$ is equal to $C_m |\chi^{(3)}|^2$, where C_m is some parameter independent of N_{C60} . Neglecting the direct and microscopic cascaded contributions to the fifth-order susceptibility of pure CS₂, as their values do not change the dependence of $|\chi^{(5)}|$ on N_{C60} , we can find C_m from the value of $|\chi^{(5)} \Xi(\theta)|/|\chi^{(3)}|^2$ evaluated at $N_{C60} = 0$. Then, multiplying the concentration dependence of $|\chi^{(3)}|^2$ by the value of C_m , we find $|\chi_{\text{macro}}^{(5)} \Xi(\theta)|$. We can estimate $|\chi_{\text{dir}}^{(5)} + \chi_{\text{micro}}^{(5)}|$ from Eq. (104), and find that $|\chi^{(5)}| - |\chi_{\text{macro}}^{(5)}| \leq |\chi_{\text{dir}}^{(5)} + \chi_{\text{micro}}^{(5)}|$.

We have measured the nonlinear susceptibilities at four values of the angle between the interacting beams (marked in Fig. 32 with thick vertical lines with the numbers on top). The results of the measurements are presented in Fig. 33, where we plot the values of $|\chi^{(5)} \Xi(\theta)|$ and $|\chi_{\text{macro}}^{(5)} \Xi(\theta)|$ as functions of the C₆₀ molar concentration.

For $\theta \approx 0.3^\circ$, corresponding to position 1 in Fig. 32, we observed no difference between the $|\chi^{(5)} \Xi(\theta)|$ and $|\chi_{\text{macro}}^{(5)} \Xi(\theta)|$ [see Fig. 33(a)]. This fact suggests that for this experimental geometry the macroscopic cascaded contribution to $|\chi^{(5)}|$ is much larger than the direct and

Figure 32

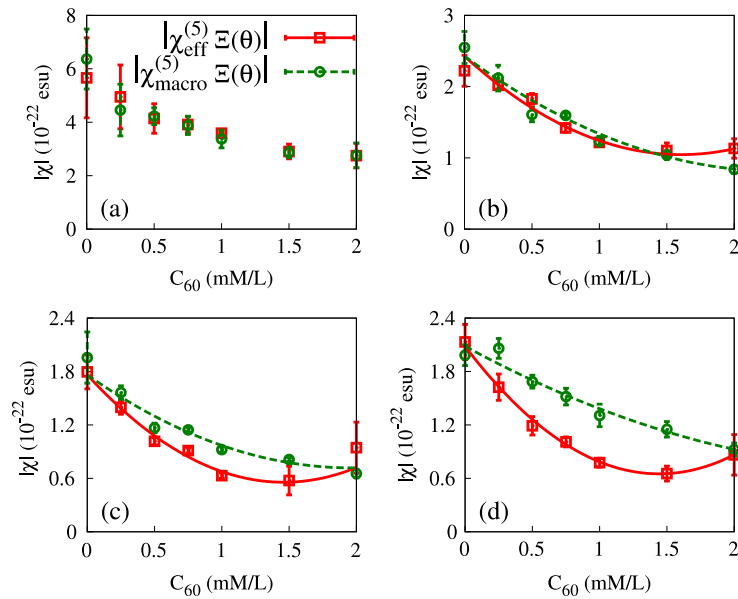


Efficiencies of the direct and microscopic cascaded contributions (red solid curve) and the macroscopic cascaded contribution (green dashed curve) as functions of the half-angle between the interacting beams. Vertical lines show the experimental cases. Reproduced with permission from Fig. 3, Ref. [138]. Copyright 2009 by the American Physical Society (<http://link.aps.org/doi/10.1103/PhysRevLett.103.113902>).

microscopic cascaded contributions. We repeated the measurement, increasing the angle to 0.43° (position 2 in Fig. 32). The resulting measured values of $|\chi^{(5)} \Xi(\theta)|$ and $|\chi_{\text{macro}}^{(5)} \Xi(\theta)|$ are shown in Fig. 33(b). One can see a clear difference between $|\chi^{(5)} \Xi(\theta)|$ and $|\chi_{\text{macro}}^{(5)} \Xi(\theta)|$. This means that, together with the macroscopic cascaded contribution, we observe the presence of other contributions to $|\chi^{(5)}|$, which are the direct and microscopic cascaded terms. Taking a careful look at position 2 in Fig. 32, one can see that, compared with position 1, the curve characterizing the efficiency of the macroscopic cascaded contribution drops significantly, while the curve describing the efficiency of the other two contributions decreases by a much smaller amount. This observation explains why we were not capable of observing the direct and microscopic cascaded contributions in $|\chi^{(5)}|$ at position 1, but see these contributions in the experimental data taken at position 2.

The angles corresponding to positions 3 and 4 in Fig. 32 are in close vicinity to the minimum of the macroscopic cascading efficiency curve. The corresponding results are presented in Figs. 33(c) and 33(d). The large difference between $|\chi^{(5)} \Xi(\theta)|$ and $|\chi_{\text{macro}}^{(5)} \Xi(\theta)|$ indicates that the macroscopic cascaded contribution is not the dominant contribution to $|\chi^{(5)}|$. Observation of positions 3 and 4 in Fig. 32 and the corresponding data in Figs. 33(c) and 33(d) show a good correlation between the efficiency curves and the experimental data. Indeed, position 3 corresponds to the decrease of the macroscopic cascaded contribution efficiency, and position 4 is very close to the minimum of this curve, while the efficiencies of the direct and macroscopic cascaded contributions are relatively high at these positions. As a result,

Figure 33



Experimentally measured $|\chi^{(5)} \Xi(\theta)|$ and $|\chi_{\text{macro}}^{(5)} \Xi(\theta)|$ as functions of $N_{C_{60}}$. The measurements are done at the angles between the interacting beams corresponding to (a) position 1 in Fig. 32, (b) position 2, (c) position 3, and (d) position 4. The least-squares fits to the experimental data are shown with curves. Reproduced with permission from Fig. 4, Ref. [138]. Copyright 2009 by the American Physical Society (<http://link.aps.org/doi/10.1103/PhysRevLett.103.113902>).

we observe a large difference between $|\chi^{(5)} \Xi(\theta)|$ and $|\chi_{\text{macro}}^{(5)} \Xi(\theta)|$ in Fig. 33(c), and an even larger difference in Fig. 33(d).

The data of Fig. 33(d) show that under these conditions the microscopic cascaded term makes a very large contribution to $|\chi^{(5)}|$. Unfortunately, we are not able to extract the precise value of this contribution from our data because each of the contributions to the measured signal is a complex quantity, and we do not know the relative complex phase of each contribution. Instead, we assume that the relative complex phases between the direct, macroscopic, and microscopic cascaded contributions to $|\chi^{(5)}|$ take arbitrary values in the range between 0 and π . These relative complex phases include the phase mismatch, which scales differently with the angle θ for $\chi_{\text{micro}}^{(5)}$ and $\chi_{\text{macro}}^{(5)}$. We fit our experimental data to the square root of a fourth-order polynomial with respect to the molecular density N for different fixed values of the relative complex phases. An example of the least-squares fit is shown with lines in Fig. 4 for the case of zero phase difference. Our fit outcome indicates that the values of the ratio between $|\chi_{\text{micro}}^{(5)}|$ and $|\chi_{\text{macro}}^{(5)}|$ are in the range [1.75, 5.0]. The values falling into this range have the smallest fit uncertainty (<30%). This shows that, under the conditions of Fig. 33(d), the microscopic cascaded contribution is more significant than the macroscopic cascaded contribution to $|\chi^{(5)}|$.

7. Conclusions

With the growing importance of photonics in different areas, including medicine, military, and science, there is a demand for new materials with substantially improved optical properties. As the cost associated with nanofabrication goes down, it becomes possible to explore nanostructuring as the means for optimizing the optical performance of various materials. The focus of this review paper was tailoring the optical properties of laser and nonlinear optical materials by nanostructuring and through local-field effects. Local-field effects arise as a result of the change of the local electric field driving an atomic transition induced by the neighboring atoms and molecules, and it is the local field that is responsible for the optical properties of the medium. The contribution to the local field at an emitter from its immediate neighbors can be controlled by nanostructuring. We have shown how it is possible to combine local-field effects and nanostructuring to effectively manipulate the optical properties of composite materials.

We have given an up-to-date overview of the progress in theoretical and experimental investigation of the influence of local-field effects on the radiative lifetime in photonic materials. This topic has been attracting much interest over the past two decades, as there have been a few theoretical models that, at first glance, contradict one another. The availability of experimental methods to verify the theoretical studies triggered a number of experiments on measuring the radiative lifetimes of photonic materials. The experimental outcomes and data analysis frequently lead to ambiguous conclusions, however, and a large number of attempts to reconcile the theories and to develop some physical understanding sometimes brought up new confusions. That is why we found it necessary to review the existing theories and experimental studies with the emphasis on recent findings. We believe that our attempt to compile a summary of research on the radiative transition rate in dielectrics will help one to see that there is, in fact, much progress in understanding the physics of local-field effects.

We also summarized recent work on modification of the basic laser parameters by local-field effects and nanostructuring with emphasis on small-signal gain. We have shown that the small-signal gain, radiative lifetime, and saturation intensity can be controlled almost independently, which gives some freedom in tailoring these properties for specific applications. We have presented a method of theoretical treatment of the small-signal gain coefficient in an arbitrary composite geometry. Here we have emphasized that the action of the local field on the emitters in composite materials is twofold: by the impact from the local environment in the immediate vicinity of the emitter within the constituent where it is embedded, and from the nanocomposite geometry. We gave examples of applying the theory to the layered and Maxwell Garnett composite geometries. We also demonstrated the conditions under which it is possible to achieve an enhancement of the small-signal gain coefficient compared with its value in a bulk constituent. We thus have shown that the impact of local-field effects is significant not only in the nonlinear optical regime, but in the linear optical regime as well.

Local-field effects are especially significant in the nonlinear optical regime, as the nonlinear optical response of photonic materials scales with the local field strength according to a power law. It is thus possible to achieve a significant enhancement of the nonlinear optical response in a composite material compared with its bulk constituents by a proper nanostructuring. We have summarized recent theoretical and experimental studies of the nonlinear optical response in nanocomposite materials of various geometries. More than tenfold enhancement has been demonstrated both theoretically and experimentally in the Maxwell Garnett composite geometry with a nonlinear host and layered composite geometry. An enhancement predicted (and observed) in Bruggeman composite materials is not as significant because the electric field localization in such randomly intermixed structures is not as strong. The enhancement is especially dramatic in metal–dielectric nanocomposite materials, such as suspensions of metal nanoparticles in a nonlinear host material and metal–dielectric films, because of a combined effect of surface plasmon resonances and local-field enhancement. Continuing effort in this research direction will bring many more practical opportunities.

Owing to their obscure complex nature, local-field effects can give rise to new, sometimes unexpected physical phenomena. One example that we have discussed in detail in this review is local-field-induced microscopic cascaded contribution of the lower-order nonlinearities to higher-order nonlinear susceptibilities. We have shown, carefully applying Bloembergen’s prescription, how this effect appears in calculation of the fifth-order nonlinear optical susceptibility. The equation obtained for the local-field-corrected $\chi^{(5)}$ contains not only an obvious term coming from the fifth-order hyperpolarizability contribution (the direct term), but also two extra terms, proportional to the second power of the third-order hyperpolarizability. The two extra terms are induced purely by local-field effects. This kind of cascaded contribution from the lower-order hyperpolarizability to the higher-order nonlinear terms will appear in high-order susceptibilities describing other nonlinear effects as well.

Together with the fundamental interest in the microscopic cascading effect, there is a practical significance for its detailed investigation. Many studies in quantum information science require materials that can respond to the simultaneous presence of N photons, as in N -photon absorption. One more particular example of a potential application of the high-order nonlinear response is in the context of quantum lithography [142]. In particular, Boto *et al.* have suggested exposing an N -photon absorbing lithographic material to the interference pattern created by N entangled photons. They show that under certain conditions this procedure would allow one to record a fringe pattern with a fringe spacing N times smaller than the Rayleigh $\lambda/2$ limit. The field of quantum information is thus in need of efficient multiphoton-absorbing materials. Microscopic cascading allows one to synthesize higher-order nonlinearities out of lower-order nonlinearities by means of local-field effects, and therefore has potential application for the development of high-order nonlinear optical materials.

We have presented a detailed description of an experimental demonstration of the presence of a local-field-induced microscopic cascaded

contribution in the measured $\chi^{(5)}$. This experiment was reported earlier in [138], but some details of the data analysis were omitted for the sake of brevity. As this experiment is, to the best of our knowledge, the first study of this kind, we have included a more detailed description in this review. We determined the conditions under which the microscopic cascaded contribution is most significant. Even though it is sometimes easier to implement the macroscopic cascaded process, there can be situations in which this procedure is unaccessible. Further experimental studies should help one to implement the microscopic cascaded effect for achieving multiphoton absorption, which occurs locally, meaning that the macroscopic cascaded effect is of no use for this phenomenon. The experimental results reported here may thus constitute an important first step in developing new nonlinear materials. A follow-up study on third-order nonlinearity enhancement through the second-order nonlinear cascaded contribution shows promising results [143].

When the interaction between the atoms of a material system is very strong, mean-field theories break down, as the local field may no longer be uniform at the scale of the optical wavelength. The contribution to the local field at a particular atom from the neighboring atoms becomes a dominant effect rather than a correction to the average field in the medium. Then local field variation on a scale much less than λ is possible, and it can lead to giant resonances and dramatic changes in the nature of light-matter interaction in both linear and nonlinear optical regimes. Such a subwavelength spatial modulation of polarization and local field in 1D and 2D arrays of strongly interacting resonant atoms was recently theoretically discovered by Kaplan and Volkov [144–146]. The resulting phenomena include size-related resonances, local field enhancement and suppression, “magic numbers,” and optical bistability. The potential applications of these phenomena range from molecular computers to biosensors and nanoelements for switching and logic [144]. These results further prove that there exist many hidden treasures that local-field effects have yet to offer, and research in this field will result in exciting discoveries having large practical implications.

Acknowledgments

The authors are grateful to Prof. Peter Milonni for many fruitful discussions and collaborations. K. Dolgaleva also acknowledges Dr. Maxim Gladush from the Institute of Spectroscopy in Troitsk, Russia, for a valuable discussion with regard to the theories of spontaneous emission rate in dielectric media. She is also thankful to Dr. Sergei Volkov and Dr. Sergei Zhukovsky for other related important discussions.

The work was supported in part by the NSF and by a MURI grant from the U.S. Research Army Research Office. K. Dolgaleva has been supported by Canadian Mitacs Elevate postdoctoral research funding, and R. W. Boyd acknowledges support from the Canada Excellence Research Program.

References and Notes

1. J. Guo, J. Cooper, and A. Gallagher, "Selective reflection from a dense atomic vapor," *Phys. Rev. A* **53**, 1130–1138 (1996).
2. H. A. Lorentz, *Theory of Electrons*, 2nd ed. (Teubner, 1916).
3. J. D. Jackson, *Classical Electrodynamics*, 3rd ed. (Wiley, 1999).
4. D. E. Aspnes, "Local-field effects and effective-medium theory: a microscopic perspective," *Am. J. Phys.* **50**, 704–709 (1982).
5. P. de Vries and A. Lagendijk, "Resonant scattering and spontaneous emission in dielectrics: microscopic derivation of local-field effects," *Phys. Rev. Lett.* **81**, 1381–1384 (1998).
6. L. Onsager, "Electric moments of molecules in liquids," *J. Am. Chem. Soc.* **58**, 1486–1493 (1936).
7. F. Hynne and R. K. Bullough, "The Onsager reaction field as a screened self-interaction in refractive-index theory," *J. Phys. A* **5**, 1272–1295 (1972).
8. J. U. Andersen and E. Bonderup, "Local field corrections for light absorption by fullerenes," *Eur. Phys. J. D* **11**, 435–448 (2000).
9. R. J. Glauber and M. Lewenstein, "Quantum optics of dielectric media," *Phys. Rev. A* **43**, 467–491 (1991).
10. A. Ikesue and Y. L. Aung, "Synthesis and performance of advanced ceramic lasers," *J. Am. Ceram. Soc.* **89**, 1936–1944 (2006).
11. T. T. Basiev, M. E. Doroshenko, V. A. Konyushkin, V. V. Osiko, L. I. Ivanov, and S. V. Simakov, "Lasing in diode-pumped fluoride nanostructure $F_2^-:LiF$ colour centre ceramics," *Quantum Electron.* **37**, 989–990 (2007).
12. F. J. Duarte and R. O. James, "Tunable solid-state lasers incorporating dye-doped, polymer-nanoparticle gain media," *Opt. Lett.* **28**, 2088–2090 (2003).
13. F. J. Duarte and R. O. James, "Spatial structure of dye-doped polymer nanoparticle laser media," *Appl. Opt.* **43**, 4088–4090 (2004).
14. J. C. Maxwell Garnett, "Colours in metal glasses and in metallic films," *Philos. Trans. R. Soc. London A* **203**, 359–371, 385–420 (1904).
15. J. C. Maxwell Garnett, "Colours in metal glasses, in metallic films, and in metallic solutions," *Philos. Trans. R. Soc. London A* **205**, 237–288, 387–401 (1906).
16. V. M. Shalaev and M. I. Stockman, "Fractals: optical susceptibility and giant Raman scattering," *Z. Phys. D* **10**, 71–79 (1988).
17. R. J. Gehr and R. W. Boyd, "Optical properties of nanostructured optical materials," *Chem. Mater.* **8**, 1807–1819 (1996).
18. P. W. Milonni, "Field quantization and radiative processes in dispersive dielectric media," *J. Mod. Optic.* **42**, 1991–2004 (1995).
19. M. S. Tomaš, "Local-field corrections to the decay rate of excited molecules in absorbing cavities: the Onsager model," *Phys. Rev. A* **63**, 053811 (2001).
20. H. T. Dung, S. Y. Buhmann, and D.-G. Welsch, "Local-field correction to the spontaneous decay rate of atoms embedded in bodies of finite size," *Phys. Rev. A* **74**, 023803 (2006).
21. G. L. J. A. Rikken and Y. A. R. R. Kessener, "Local field effects and electric and magnetic dipole transitions in dielectrics," *Phys. Rev. Lett.* **74**, 880–883 (1995).

22. F. J. P. Schuurmans, D. T. N. de Lang, G. H. Wegdam, R. Sprik, and A. Lagendijk, "Local-field effects on spontaneous emission in a dense supercritical gas," *Phys. Rev. Lett.* **80**, 5077–5080 (1998).
23. G. M. Kumar, D. N. Rao, and G. S. Agarwal, "Measurement of local field effects of the host on the lifetimes of embedded emitters," *Phys. Rev. Lett.* **91**, 203903 (2003).
24. G. M. Kumar, D. N. Rao, and G. S. Agarwal, "Experimental studies of spontaneous emission from dopants in an absorbing dielectric," *Opt. Lett.* **30**, 732–734 (2005).
25. C.-K. Duan, M. F. Reid, and Z. Wang, "Local field effects on the radiative lifetime of emitters in surrounding media: virtual- or real-cavity model?" *Phys. Lett. A* **343**, 474–480 (2005).
26. P. Lavallard, M. Rosenbauer, and T. Gacoin, "Influence of surrounding dielectrics on the spontaneous emission of sulphorhodamine B molecules," *Phys. Rev. A* **54**, 5450–5453 (1996).
27. G. Lamouche, P. Lavallard, and T. Gacoin, "Optical properties of dye molecules as a function of the surrounding dielectric medium," *Phys. Rev. A* **59**, 4668–4674 (1999).
28. S. F. Wuister, C. de Mello Donega, and A. Meijerink, "Local-field effects on the spontaneous emission rate of CdTe and CdSe quantum dots in dielectric media," *J. Chem. Phys.* **121**, 4310–4315 (2004).
29. K. Dolgaleva, R. W. Boyd, and P. W. Milonni, "Influence of local-field effects on the radiative lifetime of liquid suspensions of Nd:YAG nanoparticles," *J. Opt. Soc. Am. B* **24**, 516–521 (2007).
30. J. E. Sipe and R. W. Boyd, "Nonlinear susceptibility of composite optical materials in the Maxwell Garnett model," *Phys. Rev. A* **46**, 1614–1629 (1992).
31. J. E. Sipe and R. W. Boyd, "Nanocomposite materials for nonlinear optics based on local field effects," in *Optical Properties of Nanostructured Random Media*, Vol. 82 of Topics in Applied Physics, V. M. Shalaev, ed. (Springer-Verlag, 2002), pp. 1–19.
32. R. W. Boyd and J. E. Sipe, "Nonlinear optical susceptibilities of layered composite materials," *J. Opt. Soc. Am. B* **11**, 297–303 (1994).
33. R. W. Boyd, R. J. Gehr, G. L. Fischer, and J. E. Sipe, "Nonlinear optical properties of nanocomposite materials," *Pure Appl. Opt.* **5**, 505–512 (1996).
34. G. L. Fischer, R. W. Boyd, R. J. Gehr, S. A. Jenekhe, J. A. Osaheni, J. E. Sipe, and L. A. Weller-Brophy, "Enhanced nonlinear optical response of composite materials," *Phys. Rev. Lett.* **74**, 1871–1874 (1995).
35. D. D. Smith, G. Fischer, R. W. Boyd, and D. A. Gregory, "Cancellation of photoinduced absorption in metal nanoparticle composites through a counterintuitive consequence of local field effects," *J. Opt. Soc. Am. B* **14**, 1625–1631 (1997).
36. R. L. Nelson and R. W. Boyd, "Enhanced electro-optic response of layered composite materials," *Appl. Phys. Lett.* **74**, 2417–2419 (1999).
37. R. J. Gehr, G. L. Fischer, and R. W. Boyd, "Nonlinear-optical response of porous-glass-based composite materials," *J. Opt. Soc. Am. B* **14**, 2310–2314 (1997).
38. D. E. Aspnes, "Bounds to average internal fields in two-component composites," *Phys. Rev. Lett.* **48**, 1629–1632 (1982).

39. D. E. Aspnes, "Bounds on allowed values of the effective dielectric function of two-component composites at finite frequencies," *Phys. Rev. B* **25**, 1358–1361 (1982).
40. W. G. Egan and D. E. Aspnes, "Finite-wavelength effects in composite media," *Phys. Rev. B* **26**, 5313–5320 (1982).
41. V. LeBihan, A. Pillonnet, D. Amans, G. Ledoux, O. Marty, and C. Du-jardin, "Critical dimension where the macroscopic definition of refractive index can be applied at a nanometric scale," *Phys. Rev. B* **78**, 113405 (2008).
42. X. C. Zeng, D. J. Bergman, P. M. Hui, and D. Stroud, "Effective-medium theory for weakly nonlinear composites," *Phys. Rev. B* **38**, 10970–10973 (1988).
43. M. Born and E. Wolf, *Principles of Optics*, 6th ed. (Cambridge University Press, 1997).
44. K. Dolgaleva, R. W. Boyd, and P. W. Milonni, "Effects of local fields on laser gain for layered and Maxwell Garnett composite materials," *J. Opt. A Pure Appl. Opt.* **11**, 024002 (2009).
45. R. Landauer, "The electrical resistance of binary metallic mixtures," *J. Appl. Phys.* **23**, 779–784 (1952).
46. P. Sheng, "Theory for the dielectric function of granular composite media," *Phys. Rev. Lett.* **45**, 60–63 (1980).
47. D. J. Bergman, "Exactly solvable microscopic geometries and rigorous bounds for the complex dielectric constant of a two-component composite material," *Phys. Rev. Lett.* **44**, 1285–1287 (1980).
48. K. H. Drexhage, "Influence of a dielectric interface on fluorescence decay time," *J. Lumin.* **1–2**(2), 693–701 (1970).
49. E. Yablonovitch, T. J. Gmitter, and R. Bhat, "Inhibited and enhanced spontaneous emission from optically thin AlGaAs/GaAs double heterostructures," *Phys. Rev. Lett.* **61**, 2546–2549 (1988).
50. E. Yablonovitch, "Inhibited spontaneous emission in solid-state physics and electronics," *Phys. Rev. Lett.* **58**, 2059–2062 (1987).
51. B. Ohnesorge, M. Bayer, A. Forchel, J. P. Reithmaier, N. A. Gippius, and S. G. Tikhodeev, "Enhancement of spontaneous emission rates by three-dimensional photon confinement in Bragg microcavities," *Phys. Rev. B* **56**, R4367–R4370 (1997).
52. H. Schniepp and V. Sandoghdar, "Spontaneous emission of europium ions embedded in dielectric nanospheres," *Phys. Rev. Lett.* **89**, 257403 (2002).
53. P. W. Milonni, "Spontaneous emission between mirrors," *J. Mod. Opt.* **54**, 2115–2120 (2007).
54. K. K. Pukhov, T. T. Basiev, and Y. V. Orlovskii, "Spontaneous emission in dielectric nanoparticles," *JETP Lett.* **88**, 12–18 (2008).
55. K. K. Pukhov, "Spontaneous emission in the ellipsoidal nanocrystals," *J. Rare Earths* **27**, 637–640 (2009).
56. K. K. Pukhov and T. T. Basiev, "Radiative transitions in nanocrystals," *Opt. Mater.* **32**, 1664–1667 (2010).
57. M. E. Crenshaw and C. M. Bowden, "Effects of local field on spontaneous emission in dielectric media," *Phys. Rev. Lett.* **85**, 1851–1854 (2000).
58. M. E. Crenshaw and C. M. Bowden, "Lorentz local-field effects on spontaneous emission in dielectric media," *Phys. Rev. A* **63**, 013801 (2000).
59. M. E. Crenshaw, "Comparison of quantum and classical local-field effects on two-level atoms in a dielectric," *Phys. Rev. A* **78**, 053827 (2008).

60. D. M. Gladush, Institute for Spectroscopy of the Russian Academy of Sciences, Troitsk, Russia, personal communication (July 26, 2011).
61. D. V. Kuznetsov, V. K. Roerich, and M. G. Gladush, "Using BBGKY hierarchies to study the effect of the local field on the rate of radiative relaxation of quantum systems in a dielectric medium," *Theor. Math. Phys.* **168**, 1078–1095 (2011).
62. D. V. Kuznetsov, V. K. Roerich, and M. G. Gladush, "Local field and radiative relaxation rate in a dielectric medium," *J. Exp. Theor. Phys.* **113**(4), 647–658 (2011).
63. A. A. Panteleev, V. K. Roerich, and A. N. Starostin, "Transient scattering of resonance radiation in a two-level system," *Sov. Phys. JETP* **96**, 222–240 (2003).
64. P. R. Berman and P. W. Milonni, "Microscopic theory of modified spontaneous emission in a dielectric," *Phys. Rev. Lett.* **92**, 053601 (2004).
65. J. Knoester and S. Mukamel, "Intermolecular forces, spontaneous emission, and superradiance in a dielectric medium: polariton-mediated interactions," *Phys. Rev. A* **40**, 7065–7080 (1989).
66. R. S. Meltzer, S. P. Feofilov, B. Tissue, and H. B. Yuan, "Dependence of fluorescence lifetimes of $\text{Y}_2\text{O}_3:\text{Eu}^{3+}$ nanoparticles on the surrounding medium," *Phys. Rev. B* **60**, R14012–R14015 (1999).
67. G. M. Kumar and D. N. Rao, "Modification of the spontaneous emission lifetime of Tb^{3+} in a binary glass," *Opt. Mater.* **31**, 1343–1345 (2009).
68. R. S. Meltzer, W. M. Yen, H. Zheng, S. P. Feofilov, M. J. Dejneka, B. Tissue, and H. B. Yuan, "Effect of the matrix on the radiative lifetimes of rare earth doped nanoparticles embedded in matrices," *J. Lumin.* **94–95**, 217–220 (2001).
69. D. Amans, A. Belsky, C. Dujardin, A. Hovsepyan, I. Kamenskih, A. Kotlov, G. Ledoux, N. Fedorov, C. Pedrini, and A. N. Vasil'ev, "Time-resolved VUV excited luminescence of $\text{Y}_2\text{O}_3 - \text{Yb}$ nanoparticles," *IEEE Trans. Nucl. Sci.* **57**, 1355–1359 (2010).
70. C. Dujardin, D. Amans, A. Belsky, F. Chaput, G. Ledoux, and A. Pillonnet, "Luminescence and scintillation properties at the nanoscale," *IEEE Trans. Nucl. Sci.* **57**, 1348–1354 (2010).
71. T. S. Lomheim and L. G. DeShazer, "Determination of optical cross-sections by the measurement of saturation flux using laser-pumped laser-oscillators," *J. Opt. Soc. Am.* **68**, 1575–1579 (1978).
72. T. Kushida and J. E. Geusic, "Optical refrigeration in Nd-doped yttrium aluminum garnet," *Phys. Rev. Lett.* **21**, 1172–1175 (1968).
73. S. Singh, R. G. Smith, and L. G. Van Uitert, "Stimulated-emission cross section and fluorescent quantum efficiency of Nd^{3+} in yttrium aluminum garnet at room temperature," *Phys. Rev. B* **10**, 2566–2572 (1974).
74. A. Rosencwaig and E. A. Hildum, " Nd^{3+} fluorescence quantum-efficiency measurements with photoacoustics," *Phys. Rev. B* **23**, 3301–3307 (1981).
75. C. J. Kennedy and J. D. Barry, "New evidence on quantum efficiency of Nd:YAG," *Appl. Phys. Lett.* **31**, 91–92 (1977).
76. K. Dolgaleva and R. W. Boyd, "Laser gain media based on nanocomposite materials," *J. Opt. Soc. Am. B* **24**, A19–A25 (2007).
77. F. A. Hopf, C. M. Bowden, and W. H. Louisell, "Mirrorless optical bistability with the use of the local-field correction," *Phys. Rev. A* **29**, 2591–2596 (1984).

78. J. J. Maki, M. S. Malcuit, J. E. Sipe, and R. W. Boyd, "Linear and nonlinear optical measurements of the Lorentz local field," *Phys. Rev. Lett.* **67**, 972–975 (1991).
79. K. Dolgaleva, R. W. Boyd, and J. E. Sipe, "Cascaded nonlinearity caused by local-field effects in the two-level atom," *Phys. Rev. A* **76**, 063806 (2007).
80. M. E. Crenshaw and C. M. Bowden, "Local-field effects in a dense collection of two-level atoms embedded in a dielectric medium: intrinsic optical bistability enhancement and local cooperative effects," *Phys. Rev. A* **53**, 1139–1142 (1996).
81. R. W. Boyd, *Nonlinear Optics*, 2nd ed. (Academic, 2003).
82. N. Bloembergen, *Nonlinear Optics*, 4th ed. (World Scientific, 1996).
83. L. Gao, J. P. Huang, and K. W. Yu, "Effective nonlinear optical properties of composite media of graded spherical particles," *Phys. Rev. B* **69**, 075105 (2004).
84. P. M. Hui, C. Xu, and D. Stroud, "Second-harmonic generation for a dilute suspension of coated particles," *Phys. Rev. B* **69**, 014203 (2004).
85. M. I. Stockman, K. B. Kurlayev, and T. F. George, "Linear and nonlinear optical susceptibilities of Maxwell Garnett composites: dipolar spectral theory," *Phys. Rev. B* **60**, 17071–17083 (1999).
86. R. Driben, A. Husakou, and J. Herrmann, "Low-threshold supercontinuum generation in glasses doped with silver nanoparticles," *Opt. Express* **17**, 17989–17995 (2009).
87. R. Driben, A. Husakou, and J. Herrmann, "Supercontinuum generation in aqueous colloids containing silver nanoparticles," *Opt. Lett.* **34**, 2132–2134 (2009).
88. R. Driben and J. Herrmann, "Solitary pulse propagation and soliton-induced supercontinuum generation in silica glasses containing silver nanoparticles," *Opt. Lett.* **35**, 2529–2531 (2010).
89. K.-H. Kim, A. Husakou, and J. Herrmann, "Linear and nonlinear optical characteristics of composites containing metal nanoparticles with different sizes and shapes," *Opt. Express* **18**, 7488–7496 (2010).
90. D. C. Kohlgraf-Owens and P. G. Kik, "Structural control of nonlinear optical absorption and refraction in dense metal nanoparticle arrays," *Opt. Express* **17**, 15032–15042 (2009).
91. J. P. Huang and K. W. Yu, "Optical nonlinearity enhancement of graded metallic films," *Appl. Phys. Lett.* **85**, 94–96 (2004).
92. J. P. Huang, L. Dong, and K. W. Yu, "Giant enhancement of optical nonlinearity in multilayer metallic films," *J. Appl. Phys.* **99**, 053503 (2006).
93. A. M. Zheltikov, "Mixing rules for group velocities in nanocomposite materials and photonic crystals," *JETP Lett.* **79**, 57–61 (2004).
94. A. M. Zheltikov, "Interference of scattered waves and mixing rules for group velocities in nanocomposite materials," *JETP Lett.* **99**, 37–42 (2004).
95. P. M. Hui, P. Cheung, and D. Stroud, "Theory of third-harmonic generation in random composites of nonlinear dielectrics," *J. Appl. Phys.* **84**, 3451–3457 (1998).
96. J. J. Saarinen, E. M. Vartiainen, and K.-E. Peiponen, "On tailoring of nonlinear spectral properties of nanocomposites having Maxwell Garnett or Bruggeman structure," *Opt. Rev.* **10**, 111–115 (2003).

97. G. Piredda, D. D. Smith, B. Wendling, and R. W. Boyd, "Nonlinear optical properties of a gold–silica composite with high gold fill fraction and the sign change of its nonlinear absorption coefficient," *J. Opt. Soc. Am. B* **25**, 945–950 (2008).
98. E. L. Falcão-Filho, C. B. de Araújo, A. Galembeck, M. M. Oliveira, and A. J. G. Zarbin, "Nonlinear susceptibility of colloids consisting of silver nanoparticles in carbon disulfide," *J. Opt. Soc. Am. B* **22**, 2444–2449 (2005).
99. X. Hu, P. Jiang, C. Xin, H. Yang, and Q. Gong, "Nano-Ag:polymeric composite material for ultrafast photonic crystal all-optical switching," *Appl. Phys. Lett.* **94**, 031103 (2009).
100. H. W. Lee, J. K. Anthony, H.-D. Nguyen, S. Mho, K. Kim, H. Lim, J. Lee, and F. Rotermund, "Enhanced ultrafast optical nonlinearity of porous anodized aluminum oxide nanostructures," *Opt. Express* **17**, 19093–19101 (2009).
101. T. Ning, Y. Zhou, H. Shen, H. Lu, Z. Sun, L. Cao, D. Guan, D. Zhang, and G. Yang, "Large third-order optical nonlinearity of periodic gold nanoparticle arrays coated with ZnO," *J. Phys. D Appl. Phys.* **40**, 6705–6708 (2007).
102. L. A. Gómez, C. B. de Araújo, A. M. Brito-Silva, and A. Galembeck, "Solvent effects on the linear and nonlinear optical response of silver nanoparticles," *Appl. Phys. B* **92**, 61–66 (2008).
103. R. F. Souza, M. A. R. C. Alencar, E. C. da Silva, M. R. Meneghetti, and J. M. Hickmann, "Nonlinear optical properties of Au nanoparticles colloidal system: local and nonlocal responses," *Appl. Phys. Lett.* **92**, 201902 (2008).
104. T. Ning, C. Chen, Y. Zhou, H. Lu, H. Shen, D. Zhang, P. Wang, H. Ming, and G. Yang, "Third-order optical nonlinearity of gold nanoparticle arrays embedded in a BaTiO₃ matrix," *Appl. Opt.* **48**, 375–379 (2009).
105. X. Liu, K. Matsumura, Y. Tomita, K. Yasui, K. Kojima, and K. Chikama, "Nonlinear optical responses of nanoparticle-polymer composites incorporating organic (hyperbranched polymer)-metallic nanoparticle complex," *J. Appl. Phys.* **108**, 073102 (2010).
106. W. Wang, G. Yang, W. Wu, and Z. Chen, "Effects of the morphology and nanostructure on the optical nonlinearities of Au:BaTiO₃ nanocomposite films," *J. Appl. Phys.* **94**, 6837–6840 (2003).
107. M. Sheik-Bahae, A. A. Said, T. Wei, D. J. Hagan, and E. W. Van Stryland, "Sensitive measurements of optical nonlinearities using a single beam," *IEEE J. Quantum Electron.* **26**, 760–769 (1990).
108. R. del Coso, J. Requejo-Isidro, J. Solis, J. Gonzalo, and C. N. Afonso, "Third order nonlinear optical susceptibility of Cu:Al₂O₃ nanocomposites: from spherical nanoparticles to the percolation threshold," *J. Appl. Phys.* **95**, 2755–2762 (2004).
109. I. Abram and A. Maruani, "Calculation of the nonlinear dielectric function in semiconductors," *Phys. Rev. B* **26**, 4759–4761 (1982).
110. F. A. Hopf and C. M. Bowden, "Heuristic stochastic model of mirrorless optical bistability," *Phys. Rev. A* **32**, 268–275 (1985).
111. Y. Ben-Aryeh, C. M. Bowden, and J. C. Englund, "Intrinsic optical bistability in collections of spatially distributed two-level atoms," *Phys. Rev. A* **34**, 3917–3926 (1986).

112. H. van Kampen, V. A. Sautenkov, C. J. C. Smeets, E. R. Eliel, and J. P. Woerdman, "Measurement of the excitation dependence of the Lorentz local-field shift," *Phys. Rev. A* **59**, 271–274 (1999).
113. C. R. Stroud Jr., C. M. Bowden, and L. Allen, "Self-induced transparency in self-chirped media," *Opt. Commun.* **67**, 387–390 (1988).
114. N. Wang and H. Rabitz, "Near dipole–dipole effects in electromagnetically induced transparency," *Phys. Rev. A* **51**, 5029–5031 (1995).
115. J. P. Dowling and C. M. Bowden, "Near dipole–dipole effects in lasing without inversion: an enhancement of gain and absorptionless index of refraction," *Phys. Rev. Lett.* **70**, 1421–1424 (1993).
116. A. S. Manka, J. P. Dowling, C. M. Bowden, and M. Fleischhauer, "Piezophotonic switching due to local field effects in a coherently prepared medium of three-level atoms," *Phys. Rev. Lett.* **73**, 1789–1792 (1994).
117. A. S. Manka, J. P. Dowling, C. M. Bowden, and M. Fleischhauer, "A review of local field effects in lasing without inversion," *Quantum Opt. J. Eur. Opt. Soc. Part B* **6**, 371–380 (1994).
118. S. Singh, C. M. Bowden, and J. Rai, "Gain enhancement in lasing without inversion in an optically dense medium," *Opt. Commun.* **135**, 93–97 (1997).
119. A. S. Zibrov, M. D. Lukin, L. Hollberg, D. E. Nikonov, M. O. Scully, H. G. Robinson, and V. L. Velichansky, "Experimental demonstration of enhanced index of refraction via quantum coherence in Rb," *Phys. Rev. Lett.* **76**, 3935–3938 (1996).
120. A. S. Zibrov, A. B. Matsko, L. Hollberg, and V. L. Velichansky, "Resonant enhancement of refractive index in a cascade scheme," *J. Mod. Optics* **49**, 359–365 (2002).
121. Y. R. Shen, *The Principles of Nonlinear Optics*, 2nd ed. (Wiley, 1984).
122. E. Yablonovitch, C. Flytzanis, and N. Bloembergen, "Anisotropic interference of three-wave and double two-wave frequency mixing in GaAs," *Phys. Rev. Lett.* **29**, 865–868 (1972).
123. S. D. Kramer, F. G. Parsons, and N. Bloembergen, "Interference of third-order light mixing and second-harmonic exciton generation in CuCl," *Phys. Rev. B* **9**, 1853–1856 (1974).
124. G. R. Meredith, "Cascading in optical third-harmonic generation by crystalline quartz," *Phys. Rev. B* **24**, 5522–5532 (1981).
125. R. DeSalvo, D. J. Hagan, M. Sheik-Bahae, G. Stegeman, E. W. Van Stryland, and H. Vanherzeele, "Self-focusing and self-defocusing by cascaded second-order effects in KTP," *Opt. Lett.* **17**, 28–30 (1992).
126. G. I. Stegeman, M. Sheik-Bahae, E. Van Stryland, and G. Assanto, "Large nonlinear phase shifts in second-order nonlinear-optical processes," *Opt. Lett.* **18**, 13–15 (1993).
127. Y. Baek, R. Schiek, and G. I. Stegeman, "All-optical switching in a hybrid Mach-Zehnder interferometer as a result of cascaded second-order nonlinearity," *Opt. Lett.* **20**, 2168–2170 (1995).
128. R. Schiek, Y. Baek, and G. I. Stegeman, "One-dimensional spatial solitary waves due to cascaded second-order nonlinearities in planar waveguides," *Phys. Rev. E* **53**, 1138–1141 (1996).
129. J. B. Khurgin, A. Obeidat, S. J. Lee, and Y. J. Ding, "Cascaded optical nonlinearities: microscopic understanding as a collective effect," *J. Opt. Soc. Am. B* **14**, 1977–1983 (1997).

130. G. I. Stegeman, D. J. Hagan, and L. Torner, " $\chi^{(2)}$ cascading phenomena and their applications to all-optical signal processing, mode-locking, pulse compression and solitons," *Opt. Quantum Electron.* **28**, 1691–1740 (1996).
131. G. I. Stegeman, " $\chi^{(2)}$ cascading: nonlinear phase shifts," *Quantum Semiclassic. Opt. J. Eur. Opt. Soc. Part B* **69**, 139–153 (1997).
132. D. Bedeaux and N. Bloembergen, "On the relation between macroscopic and microscopic nonlinearities," *Quantum Semiclassic. Opt. J. Eur. Opt. Soc. Part B* **69**, 57–66 (1973).
133. J. Ducuing, "Microscopic and macroscopic nonlinear optics," in *Nonlinear Optics*, P. G. Harper and B. S. Wewrrett, ed. (Academic, 1975).
134. C. Flytzanis, "Theory of nonlinear optical susceptibilities," in *Quantum Electronics*, H. Rabin and C. L. Tang, ed. (Academic, 1975).
135. G. R. Meredith, "Prospects of new nonlinear organic materials," in *Nonlinear Optics: Materials and Devices*, C. Flytzanis and J. L. Oudar, ed. (Springer-Verlag, 1986).
136. J. H. Andrews, K. L. Kowalski, and K. D. Singer, "Pair correlations, cascading, and local-field effects in nonlinear optical susceptibilities," *Phys. Rev. A* **46**, 4172–4184 (1992).
137. C. Kollck, "Cascaded second-order contribution to the third-order nonlinear susceptibility," *Phys. Rev. A* **69**, 053812 (2004).
138. K. Dolgaleva, H. Shin, and R. W. Boyd, "Observation of a microscopic cascaded contribution to the fifth-order nonlinear susceptibility," *Phys. Rev. Lett.* **103**, 113902 (2009).
139. E. Koudoumas, F. Dong, M. D. Tzatzadaki, S. Couris, and S. Leach, "High-order nonlinear optical response of C₆₀-toluene solutions in the sub-picosecond regime," *J. Phys. B* **29**, L773–L778 (1996).
140. M. Sheik-Bahae, A. A. Said, and E. W. Van Stryland, "High-sensitivity, single-beam n_2 measurements," *Opt. Lett.* **14**, 955–957 (1989).
141. S. Couris, E. Koudoumas, F. Dong, and S. Leach, "Sub-picosecond studies of the third-order optical nonlinearities of C₆₀-toluene solutions," *J. Phys. B* **29**, 5033–5041 (1996).
142. A. N. Boto, P. Kok, D. S. Abrams, S. L. Braunstein, C. P. Williams, and J. P. Dowling, "Quantum interferometric optical lithography: exploiting entanglement to beat the diffraction limit," *Phys. Rev. Lett.* **85**, 2733–2736 (2000).
143. A. Baev, J. Autschbach, R. W. Boyd, and P. N. Prasad, "Microscopic cascading of second-order molecular nonlinearity: new design principles for enhancing third-order nonlinearity," *Opt. Express* **18**, 8713–8721 (2010).
144. A. E. Kaplan and S. N. Volkov, "Nanoscale stratification of local optical fields in low-dimensional atomic lattices," *Phys. Rev. Lett.* **101**, 133902 (2008).
145. A. E. Kaplan and S. N. Volkov, "Nanoscale stratification of optical excitation in self-interacting one-dimensional arrays," *Phys. Rev. A* **79**, 053834 (2009).
146. S. N. Volkov and A. E. Kaplan, "Local-field excitations in two-dimensional lattices of resonant atoms," *Phys. Rev. A* **81**, 043801 (2010).



Ksenia Dolgaleva earned her undergraduate degree in Physics from Moscow State University, Russia. She was awarded a prize for an outstanding undergraduate thesis from Russian Physical Society. Ksenia has recently completed her Ph.D. program at the Institute of Optics, University of Rochester, USA. There she worked under the supervision of Prof. Robert Boyd on various projects, including composite laser materials and local-field-induced microscopic cascading in nonlinear optics. She is currently a Mitacs Elevate postdoctoral fellow at the Department of Electrical and Computer Engineering, University of Toronto, working with Prof. Stewart Aitchison. Her current research is focused on integrated optics in AlGaAs. Her two primary projects concern nonlinear optical interactions in AlGaAs waveguides and integrated pulse shaping devices. She was awarded a prize for an outstanding student presentation at the Frontiers in Optics OSA Annual Meeting in Rochester in October 2008.



Robert W. Boyd was born in Buffalo, New York. He received the B.S. degree in physics from MIT and the Ph.D. degree in physics from the University of California at Berkeley. His Ph.D. thesis was supervised by Charles Townes and involves the use of nonlinear optical techniques in infrared astronomy. Professor Boyd joined the faculty of the University of Rochester in 1977, and in 2001 became the M. Parker Givens Professor of Optics and Professor of Physics. In 2010 he became in addition Professor of Physics and Canada Excellence Research Chair in Quantum Nonlinear Optics at the University of Ottawa. His research interests include studies of “slow” and “fast” light propagation, quantum imaging techniques, nonlinear optical interactions, studies of the nonlinear optical properties of materials, and the development of photonic devices including photonic biosensors. Professor Boyd is the 2009 recipient of the Willis E. Lamb Award for Laser Science and Quantum Optics and in 2010 received a Humboldt research award. He is a past chair of the Division of Laser Science of APS and has been a member of the Board of Directors of OSA. Prof. Boyd has served as a member of the editorial boards of *Physical Review Letters* and of *Science* magazine.